NASA MEMO 1-22-59A

NASA MEMO 1-22-59A

A 37
3/4 624

NASA

MEMORANDUM

PRESSURE DISTRIBUTIONS AT TRANSONIC SPEEDS FOR BUMPY AND INDENTED MIDSECTIONS OF A BASIC PARABOLIC-ARC BODY

By Robert A. Taylor

Ames Research Center
Moffett Field, Calif.

NATIONAL AERONAUTICS AND
SPACE ADMINISTRATION
WASHINGTON
February 1959

NATIONAL AERONAUTICS AND SPACE ADMINISTRATION

MEMORANDUM 1-22-59A

PRESSURE DISTRIBUTIONS AT TRANSONIC SPEEDS FOR BUMPY AND INDENTED MIDSECTIONS OF A BASIC PARABOLIC-ARC BODY

By Robert A. Taylor

SUMMARY

The measured static-pressure distributions at the model surface and in the surrounding flow field are presented for a basic parabolic-arc body having a fineness ratio of 14 and for three additional bodies obtained by modifying the basic parabolic-arc body along the middle portion of the body length by adding a bump, by indenting, or by quadripole shaping. The data were obtained with the various bodies at zero angle of attack. The Mach number varied from 0.80 to 1.20 with a corresponding Reynolds number (based on body length) variation of 27×10^6 to 38×10^6. The data are subject to tunnel-wall interference and do not represent free-air conditions.

INTRODUCTION

In order to provide experimental data concerning the pressure distributions on and near bodies at transonic speeds, several experimental investigations have been conducted in the Ames 14-foot transonic wind tunnel. The experimental investigation of the transonic flows about three parabolic-arc bodies of revolution having fineness ratios of 10, 12, and 14 is described in reference 1. The present report presents the results of an experimental investigation of the transonic flows about two basic parabolic-arc bodies of fineness ratio 14 and three bodies obtained by modification of the basic body shape along the middle portion of the body length. The modifications were chosen so that the cross-sectional areas of the bodies and the first axial derivative of the cross-sectional areas were continuous. The models were found to be subject to tunnel-wall interference because of their large size.

NOTATION

C_D	drag coefficient, $\frac{D}{q_\infty l^2}$
$C_{D_{bp}}$	base-pressure drag coefficient (see eq. (6))
C_{D_f}	friction-drag coefficient
C_{D_p}	pressure-drag coefficient, $C_{D_{sp}} + C_{D_{bp}}$
$C_{D_{sp}}$	surface-pressure drag coefficient (see eq. (5))
C_p	pressure coefficient, $\frac{p-p_\infty}{q_\infty}$
D	drag
D_f	friction drag (see eq. (7))
d	body diameter
l	body length, measured from nose to point of closure
M_∞	free-stream Mach number
p	local static pressure
q_∞	free-stream dynamic pressure
R	Reynolds number, based on body length l
S	body cross-sectional area, normalized by dividing by body length squared, πH^2
ξ,η,θ	cylindrical coordinate system, see sketch (a), where ξ and η are streamwise and radial distances normalized by dividing by the body length l
H	body radius, normalized by dividing by the body length l
$(\ )',(\ )''$	first and second derivatives with respect to the normalized streamwise coordinate ξ

Subscripts

b	body base
max	maximum
∞	free-stream conditions

APPARATUS AND MODELS

Apparatus

This investigation was conducted in the Ames 14-foot transonic wind tunnel which is a closed-return tunnel equipped with a perforated test section permitting continuous operation from subsonic to low supersonic speeds (fig. 1).

The models were truncated and sting mounted as indicated in figures 2 and 3. Figure 4 indicates model geometry. The axial force was measured by a strain-gage balance enclosed within the model. Multiple-tube manometers using tetrabromoethane (specific gravity = 2.96) were photographed to record the pressure data. The force and pressure data were recorded simultaneously.

Local static-pressure data were obtained in the flow field under the model by the use of a survey tube (see figs. 5(a) and 5(b)). The survey tube was 1 inch in diameter and contained static-pressure orifices located 90° with respect to a vertical plane passing through the longitudinal axes of the model and survey tube. Both ends of the survey tube could be moved in a vertical plane so that the survey tube would always remain horizontal.

Data were recorded with the models at the tunnel center line. The locations of the survey tube with respect to the model center line (based on the large basic body) are tabulated in the following table.

Survey-tube position	Vertical distance between center lines
1	8 inches, $\eta = 0.071$
2	16 inches, $\eta = 0.142$
3	24 inches, $\eta = 0.213$
4	32 inches, $\eta = 0.284$

Models

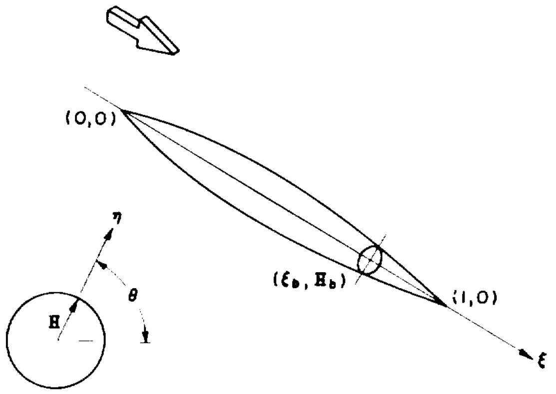

Sketch (a)

The five models tested in this investigation are shown in figure 2. The coordinate system used in the following description of the models is illustrated by sketch (a). (All distances are normalized by division by the theoretical body length l.)

Basic bodies.- The two basic bodies were parabolic-arc bodies of revolution. Both bodies had fineness ratios of 14, their lengths however were 84 and 112 inches. They will be referred to as basic body (small) and basic body (large). Their radii are defined by the equation

$$H = 4H_{max}(\xi - \xi^2) \tag{1}$$

where H is the normalized body radius. In order to permit mounting on the sting the models were truncated at $\xi = 0.854$. (The base area equals one-fourth the maximum basic body cross-sectional area.)

The streamwise variations of normalized body radius H and body slope H' are presented in figures 4(a), 4(b), 4(c), and 4(d). The variations of normalized cross-sectional area S and the first derivative S' are shown in figures 4(e) and 4(f).

Bumpy, indented, and quadripole bodies.- The bumpy, indented, and quadripole bodies were obtained by modifying the large basic parabolic-arc body of theoretical length equal to 112 inches. The modifications were confined to the middle portion from station $\xi_1 = 0.393$ to station $\xi_2 = 0.607$. The distance $\Delta\xi = \xi_2 - \xi_1$ was equal to three times the maximum body diameter before modification.

The normalized radii for the bumpy body are given by

$$H = \tilde{H} + \frac{\Delta R_{max}}{l} \sin^2\left(\frac{\xi - \xi_1}{\xi_2 - \xi_1}\right) \tag{2}$$

$$\xi_1 \leqq \xi \leqq \xi_2$$

and for the indented body

$$H = \tilde{H} - \frac{\Delta R_{max}}{l} \sin^2 \left(\frac{\xi - \xi_1}{\xi_2 - \xi_1} \right) \qquad (3)$$

$$\xi_1 \leqq \xi \leqq \xi_2$$

where $\tilde{H}$ is the normalized radius of the basic body

$$\tilde{H} = 4H_{max}(\xi - \xi^2)$$

l is the theoretical body length (112 in.), and ΔR_{max} is the incremental change in body radius as a result of the modification. A value of ΔR_{max} equal to 0.8 inch (one-tenth of the value of the maximum body diameter before modification) was used in equations (2) and (3).

The normalized body radii for the quadripole body are given by

$$H = \left(\tilde{H}^4 + 8 \cos 2\theta \int_{\xi_1}^{\xi} \frac{F^* \tilde{H}'}{\tilde{H}} d\xi + 4F^* \cos 2\theta + 8 \sin^2 2\theta \int_{\xi_1}^{\xi} \frac{f^* F^*}{\tilde{H}^4} d\xi \right)^{\frac{1}{4}}$$

where

$$F^* = \int_{\xi_1}^{\xi} f^*(\xi) d\xi$$

and

$$f^*(\xi) = H^{*3} \left(H^{*\prime} - \frac{\tilde{H}\tilde{H}'}{H^*} \right)$$

F^* and $f^*(\xi)$ were obtained graphically; $\tilde{H}$ and H^* define the body radii of the basic parabolic-arc body and a bumpy body. At $\theta = 0^\circ$, see sketch (a), the modified radii for the quadripole body are identical with the radii for a bumpy body with $\Delta R_{max} = 0.6$. The quadripole distortion of the basic body did not alter the axial distribution of cross-sectional area.

The axial variations of the normalized quantities H, H', S, and S' are presented in figures 4(a) to 4(f).

TESTS AND PROCEDURE

The models were investigated through a Mach number range from 0.80 to 1.20. The corresponding Reynolds number variations are presented in figure 6. The force and pressure data were obtained simultaneously.

It was found convenient to define the drag coefficient in the following manner

$$C_D = \frac{D}{q_\infty l^2} = C_{D_{sp}} + C_{D_{bp}} + C_{D_f} \tag{4}$$

where the component parts are defined as

$$C_{D_{sp}} = \int_0^{2\pi} \int_0^{\xi_b} C_p HH' d\theta d\xi \tag{5}$$

$$C_{D_{bp}} = -C_{p_b} S_b \tag{6}$$

$$C_{D_f} = \frac{D_f}{q_\infty l^2} \tag{7}$$

For bodies of revolution, equation (5) reduces to

$$C_{D_{sp}} = \int_0^{\xi_b} C_p S' d\xi \tag{8}$$

In the present investigation the drag coefficients calculated by the use of equations (4) to (8) were compared with the drag coefficients obtained from force balance readings. The integrated pressure drag, $C_{D_{sp}}$, was obtained by graphical integrations of the measured variations of C_pS' or C_pHH' with ξ. The base drag, $C_{D_{op}}$, was assumed to be equal to the product of the normalized base area and the negative of a measured pressure coefficient at the base (which assumes a constant pressure coefficient over the base area). The skin-friction coefficient, C_{D_f}, was estimated from the tables in reference 2. In general, it has been found that the drag coefficients calculated by the use of equations (4) to (8) agree reasonably well with the drag coefficients measured by the use of a strain-gage balance.

The experimental data were not corrected for the tunnel-wall interference that is known to affect models of the size used in this investigation. In the preparation of the data for this report it was found that the pressure data for the large basic body did not agree with theory. The model was inspected and found to be free of any measurable dimensional, surface, or orifice errors. A retest of the model failed to show any difference in the data points which led to the belief that these data were affected by tunnel-wall interference. A smaller body of the same geometry was then constructed and tested. The results of that test agreed better with theory (see ref. 1). Data from the small basic body are included on all pressure-coefficient curves to show the magnitude of possible corrections.

Consideration of the testing procedures and the data-reduction process indicate that the free-stream Mach numbers are repeatable within approximately ±0.002, the angle of attack is accurate within approximately $\pm 0.1^{\circ}$, and the pressure-coefficient data are repeatable within ±0.005. An additional error in pressure coefficient is due to transverse flow, induced by body curvature, at the survey tube. This error is negligible except for the survey-tube position closest to the body where the absolute value of the error exceeds 0.005 only for those values of ξ where S' exceeds about 0.022.

DATA PRESENTATION

The data presented in this report consist of axial forces, body surface pressures, and field pressures below the model.

Pressure Data

The pressure-distribution data are presented in figures 7 through 11. Measurements were made only on the upper surface except for the quadripole body for which some points (square symbols in fig. 10) were obtained on the lower surface. The data for the two basic bodies (from ref. 1) were faired and superimposed on the data plots for the bumpy, indented, and quadripole bodies. Although some scatter is evident in portions of the pressure-distribution data, it is felt that the great number of data points along each body surface enables one to fair the data so as to obtain reasonably accurate representations of the model surface pressures.

The pressure-distribution data for the quadripole body are presented in figures 9 through 11 for three meridian angles, $\theta = 0^{\circ}$, -45°, and -90° (see sketch (b)).

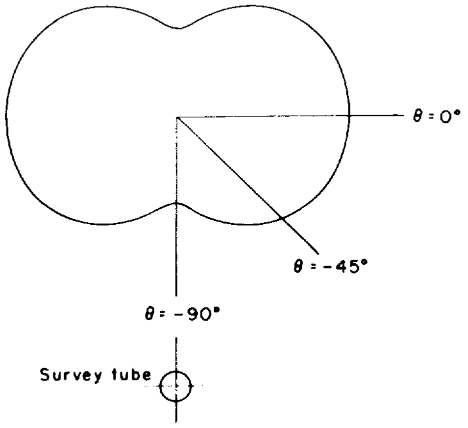

Sketch (b)

Drag Data

The drag coefficients obtained at the various Mach numbers for the four bodies are presented in figure 12. In figure 12 a comparison of the measured balance-drag coefficients[1] and the drag coefficients calculated from body pressures, base pressure, and skin friction according to equation (4) is made.

Ames Research Center
National Aeronautics and Space Administration
Moffett Field, Calif., Oct. 22, 1958

REFERENCES

1. Taylor, Robert A., and McDevitt, John B.: Pressure Distributions at Transonic Speeds for Parabolic-Arc Bodies of Revolution Having Fineness Ratios of 10, 12, and 14. NACA TN 4234, 1958.
2. Lee, Dorothy B., and Faget, Maxime A.: Charts Adapted from Van Driest's Turbulent Flat-Plate Theory for Determining Values of Turbulent Aerodynamic Friction and Heat-Transfer Coefficients. NACA TN 3811, 1956.
3. McDevitt, John B.: The Linearized Subsonic Flow About Symmetrical, Nonlifting Wing-Body Combinations. NACA TN 3964, 1957.

---

[1] The drag coefficients presented in this report have not been adjusted to represent free-stream static pressure at the model base as is often done in experimental work for bodies or wing-body combinations.

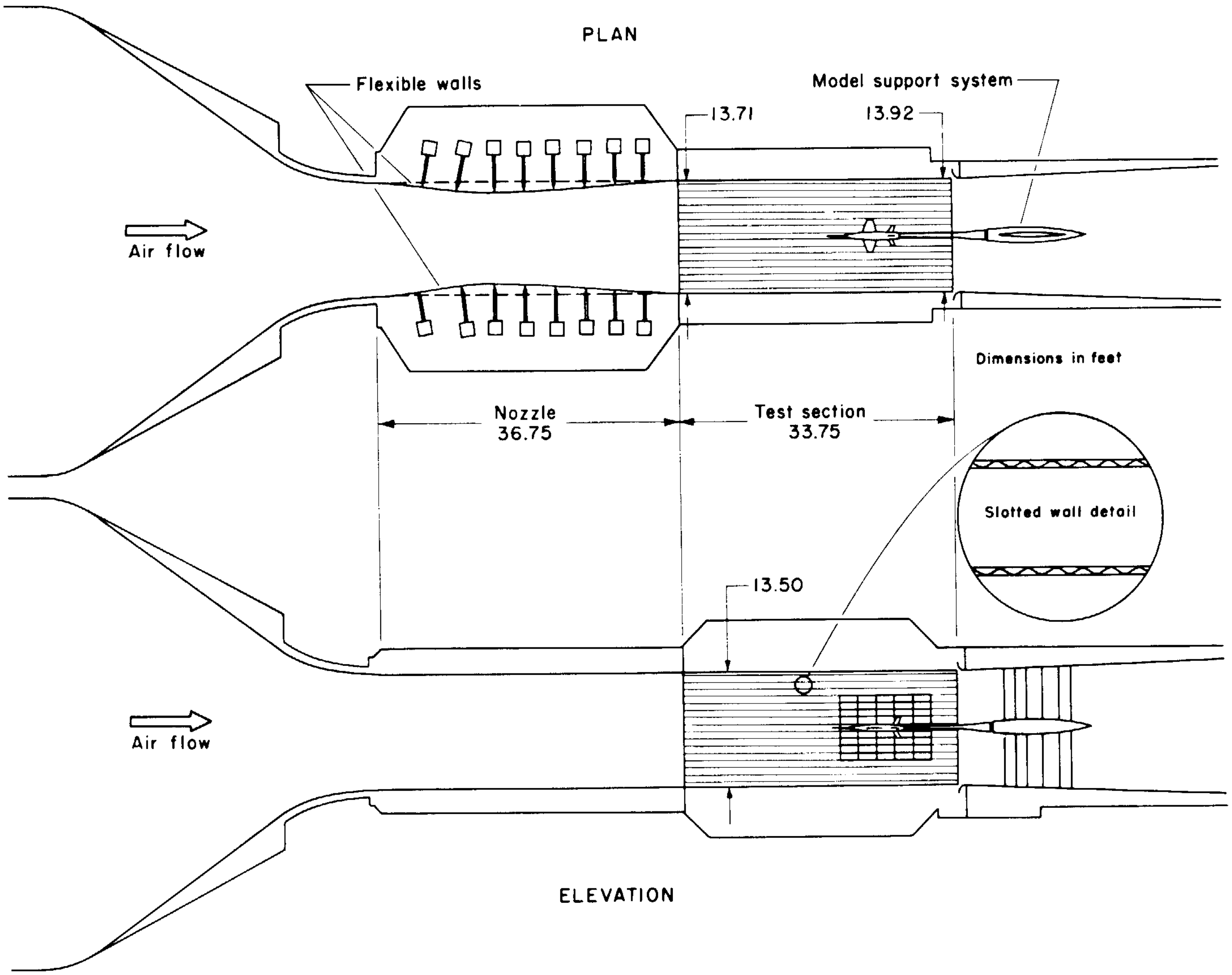

Figure 1.- General arrangement of the test section of the Ames 14-foot transonic wind tunnel.

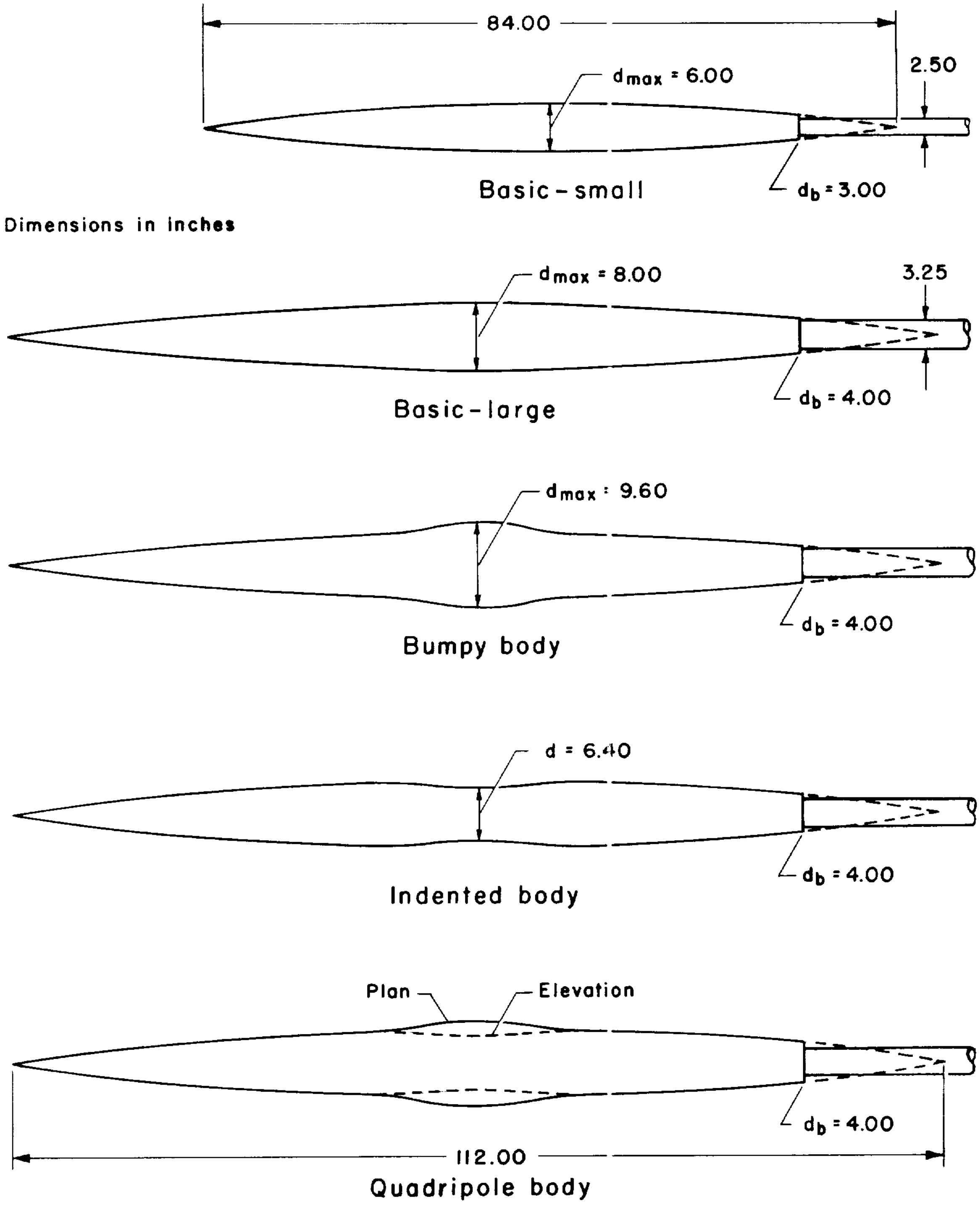

Figure 2.- Basic dimensions of the models.

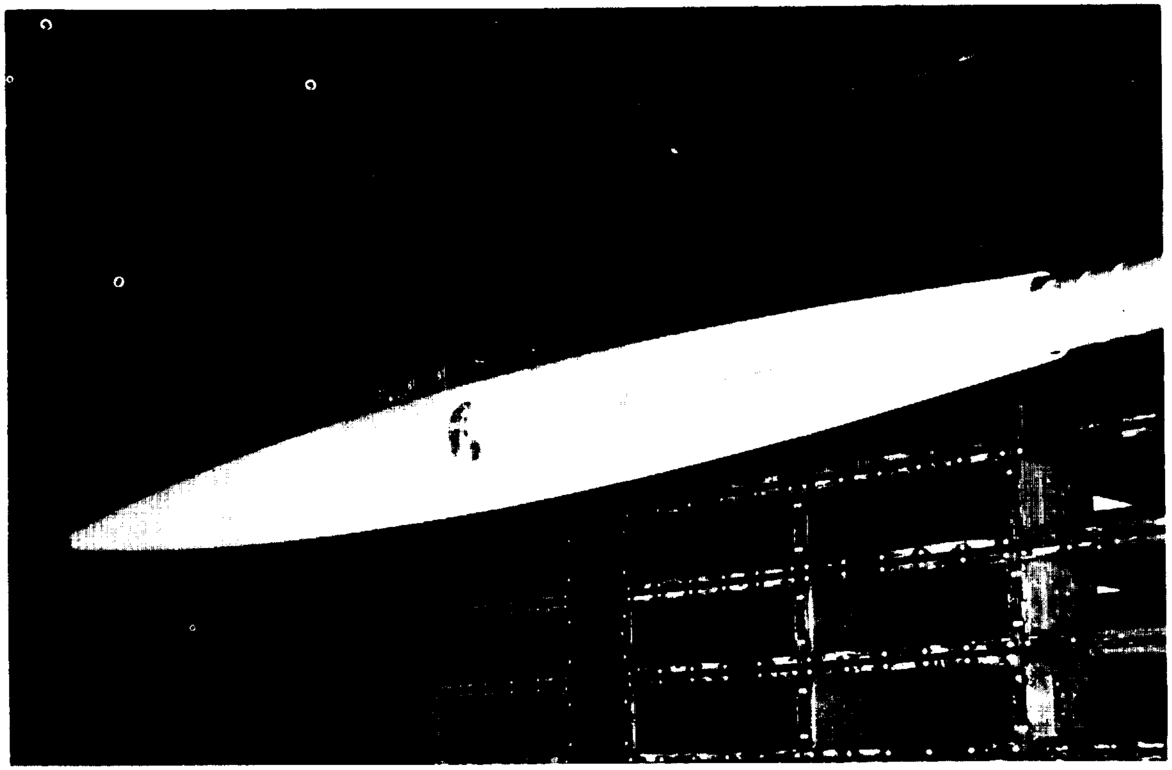

A-21873

Figure 3.- Photograph of the large basic body in the test section of the Ames 14-foot transonic wind tunnel.

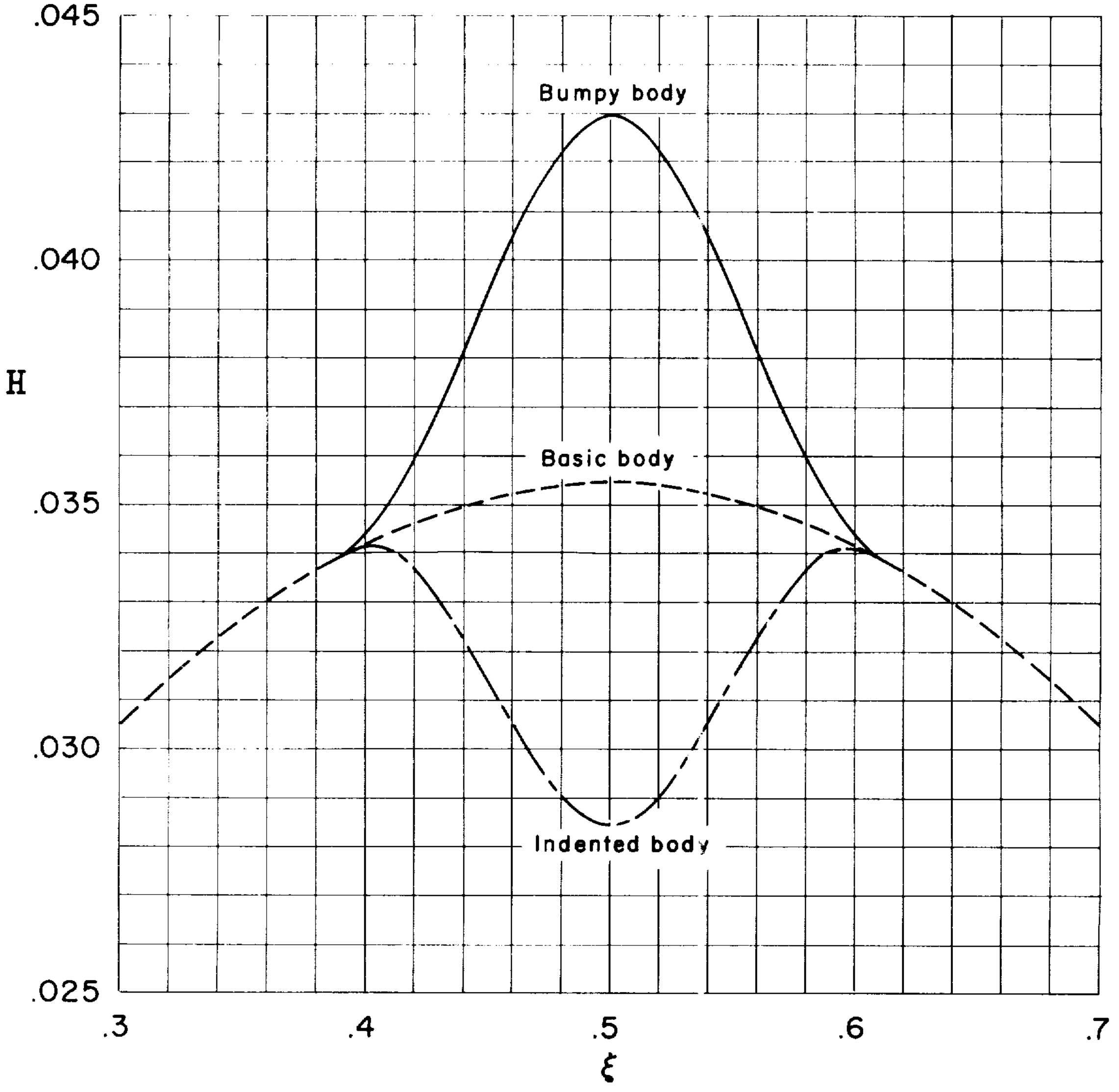

(a) Variation of H with ξ for the basic, indented, and bumpy bodies.

Figure 4.- Model geometry.

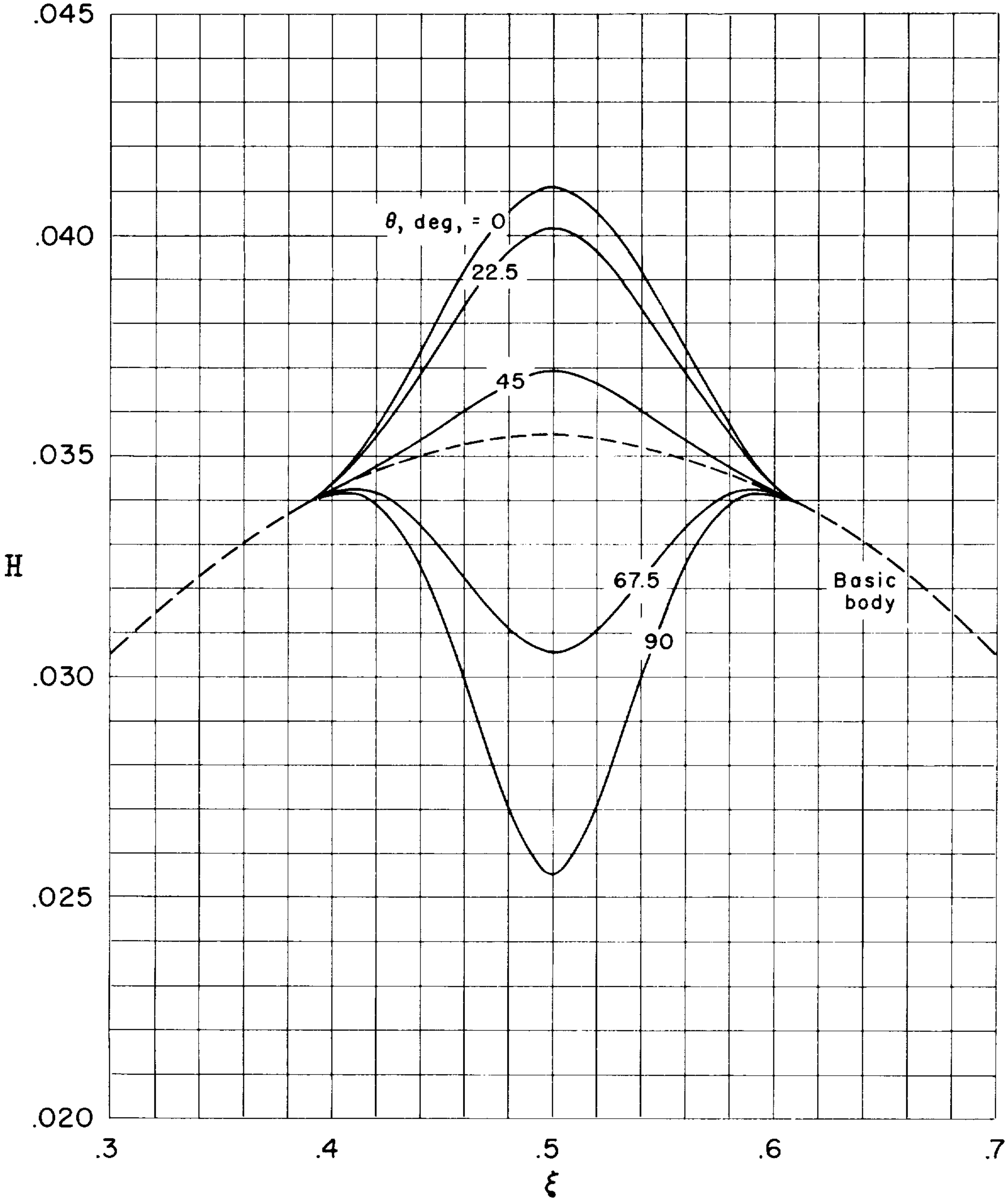

(b) Variation of H with ξ for the basic and quadripole bodies at $\theta = 0^{\circ}, 22.5^{\circ}, 45^{\circ}, 67.5^{\circ}$, and 90°.

Figure 4.- Continued.

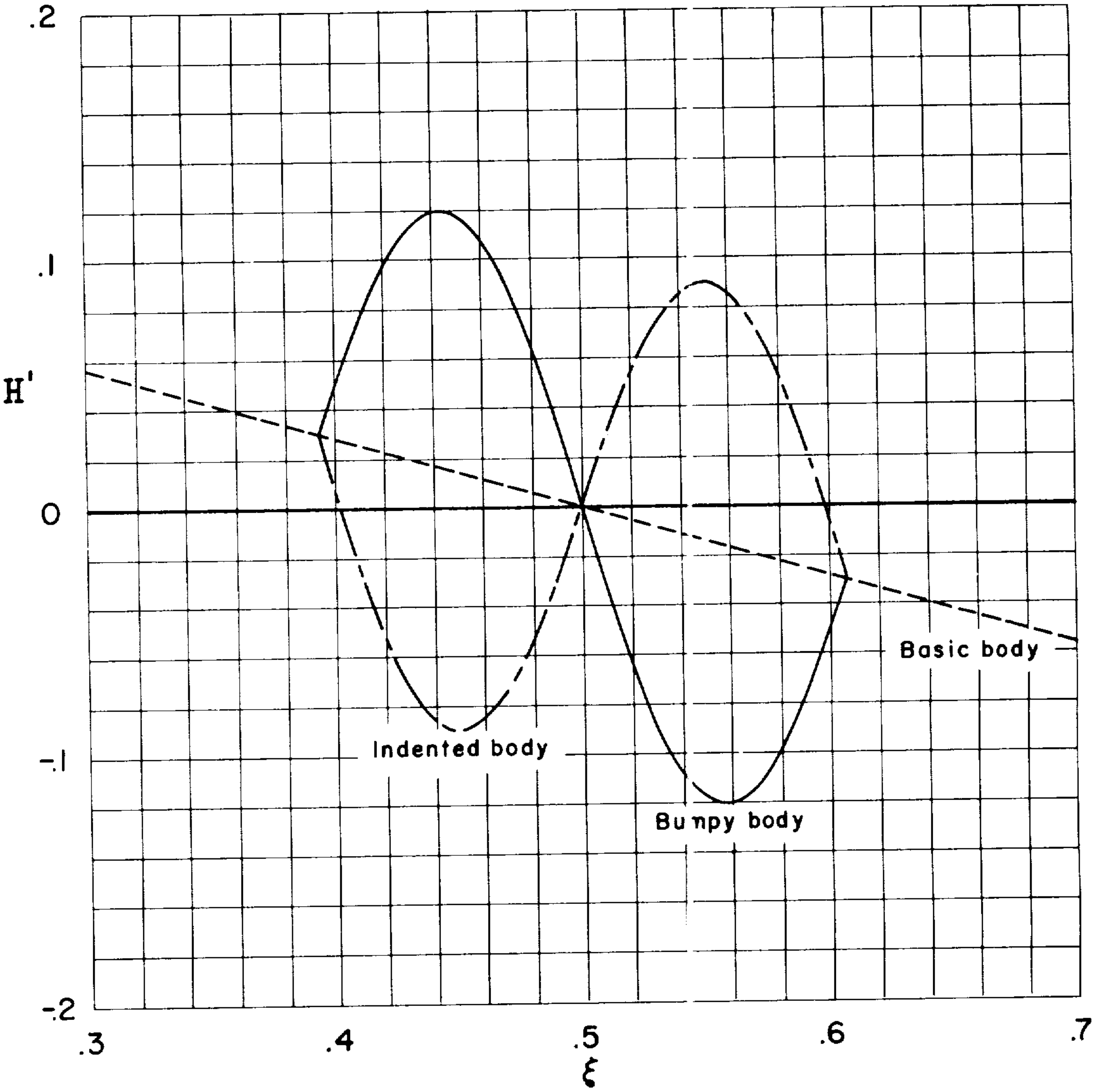

(c) Variation of H' with ξ for the basic, indented, and bumpy bodies.

Figure 4.- Continued.

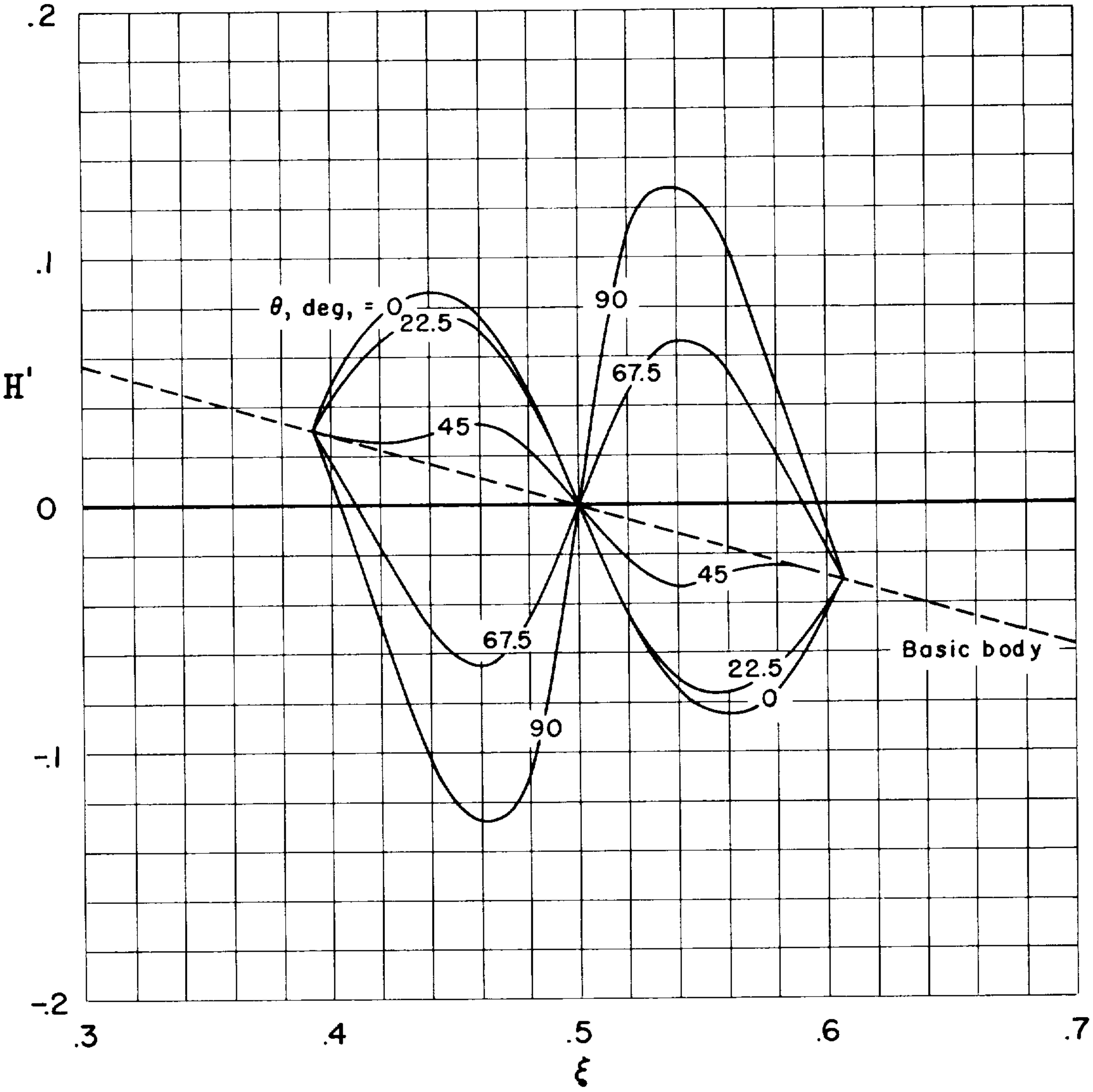

(d) Variation of H' with ξ for the basic and quadripole bodies at $\theta = 0^\circ, 22.5^\circ, 45^\circ, 67.5^\circ$, and 90°.

Figure 4.- Continued.

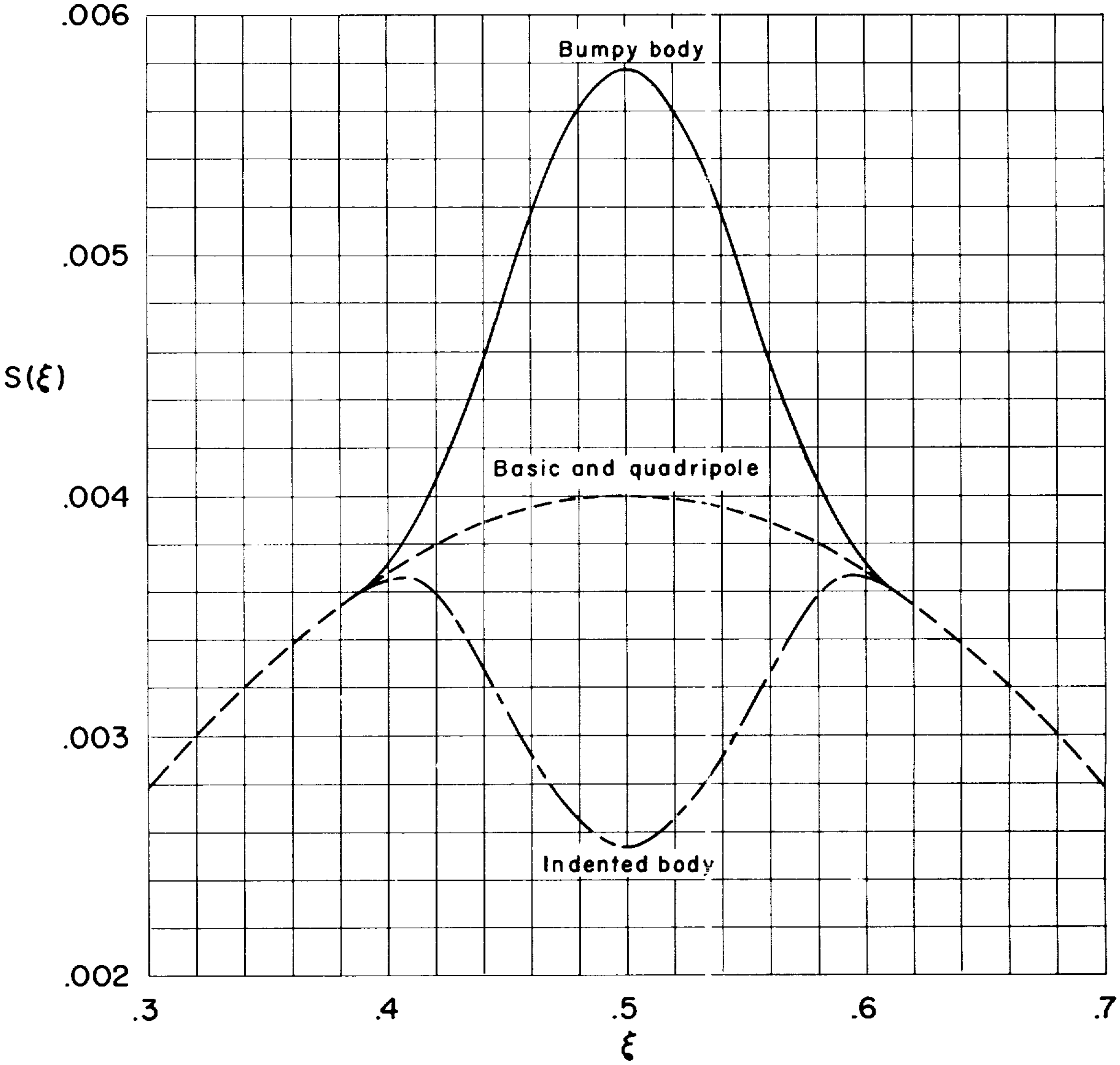

(e) Variation of S with ξ for the basic, indented, bumpy, and quadripole bodies.

Figure 4.- Continued.

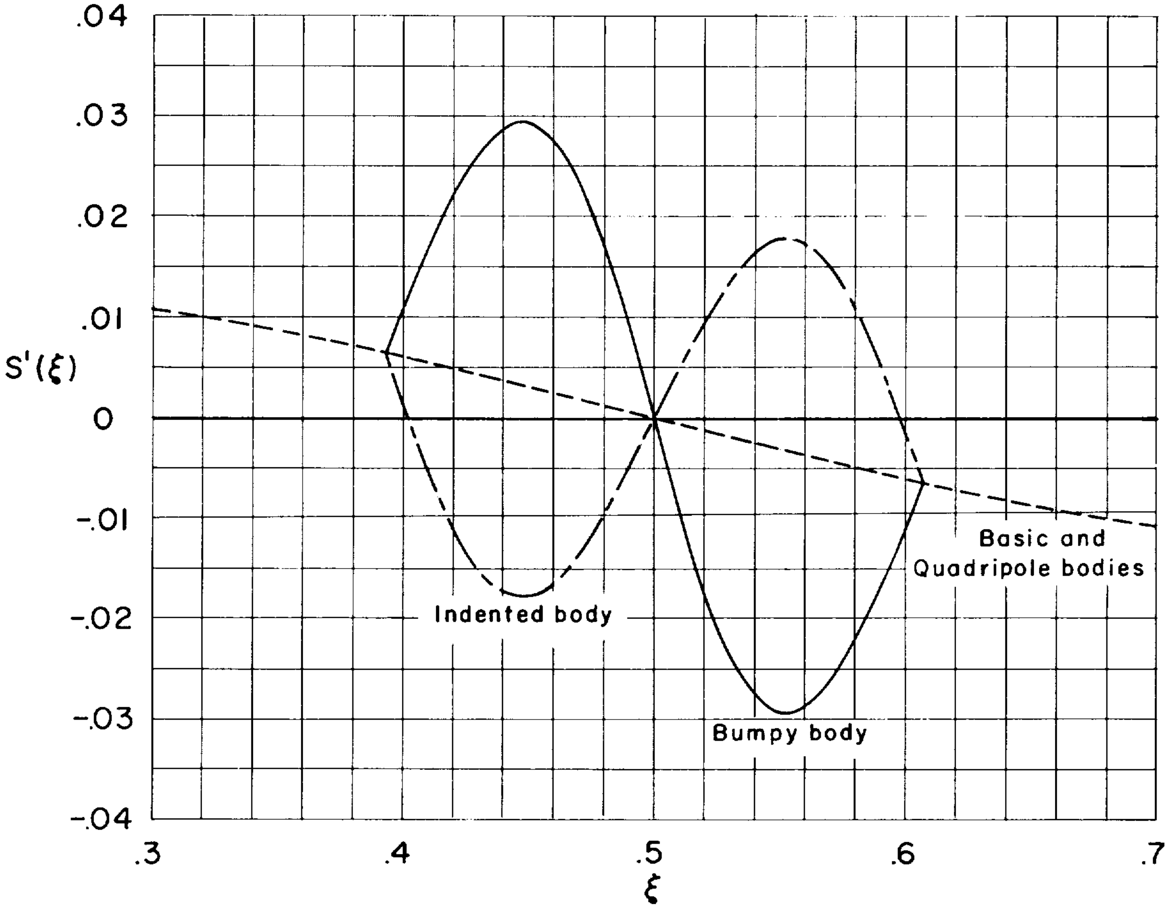

(f) Variation of S' with ξ for the basic, indented, bumpy, and quadripole bodies.

Figure 4.- Concluded.

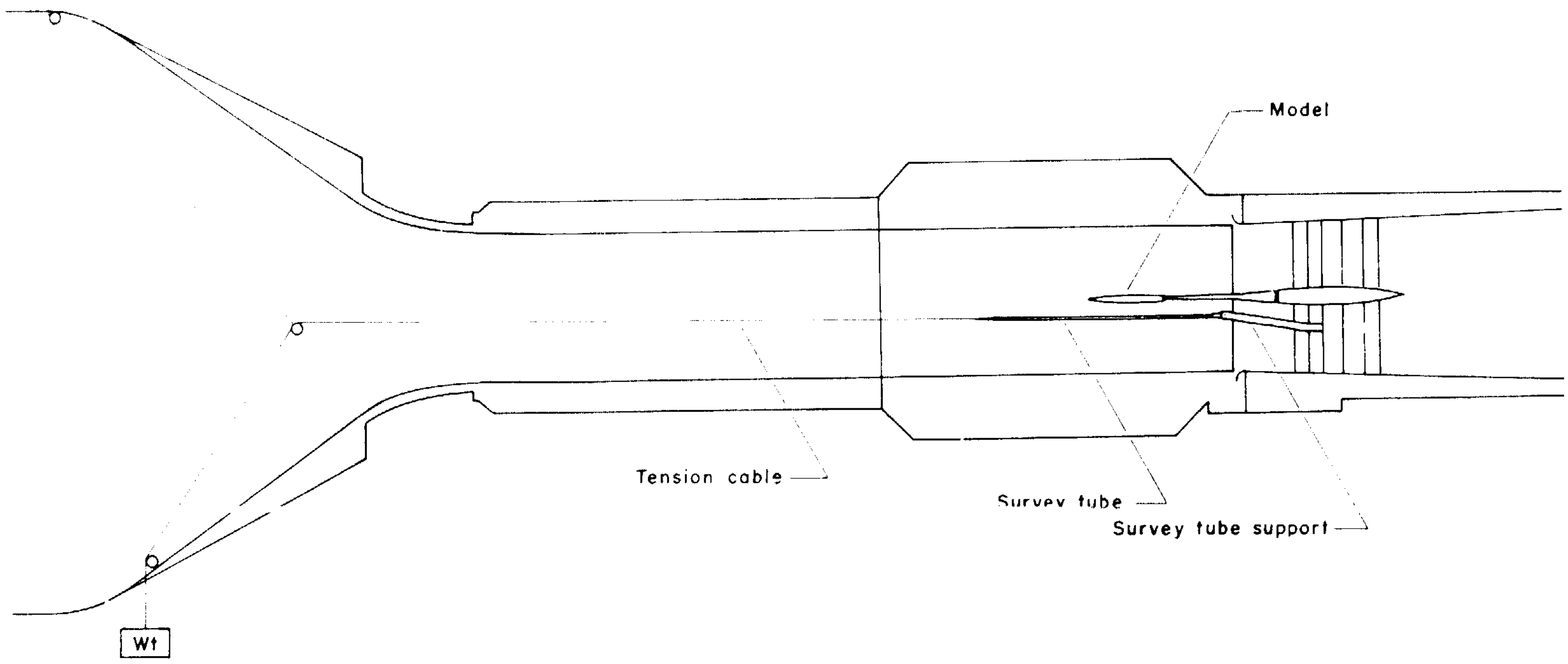

(a) Survey-tube support system.

Figure 5.- Schematic drawing of the model and survey tube.

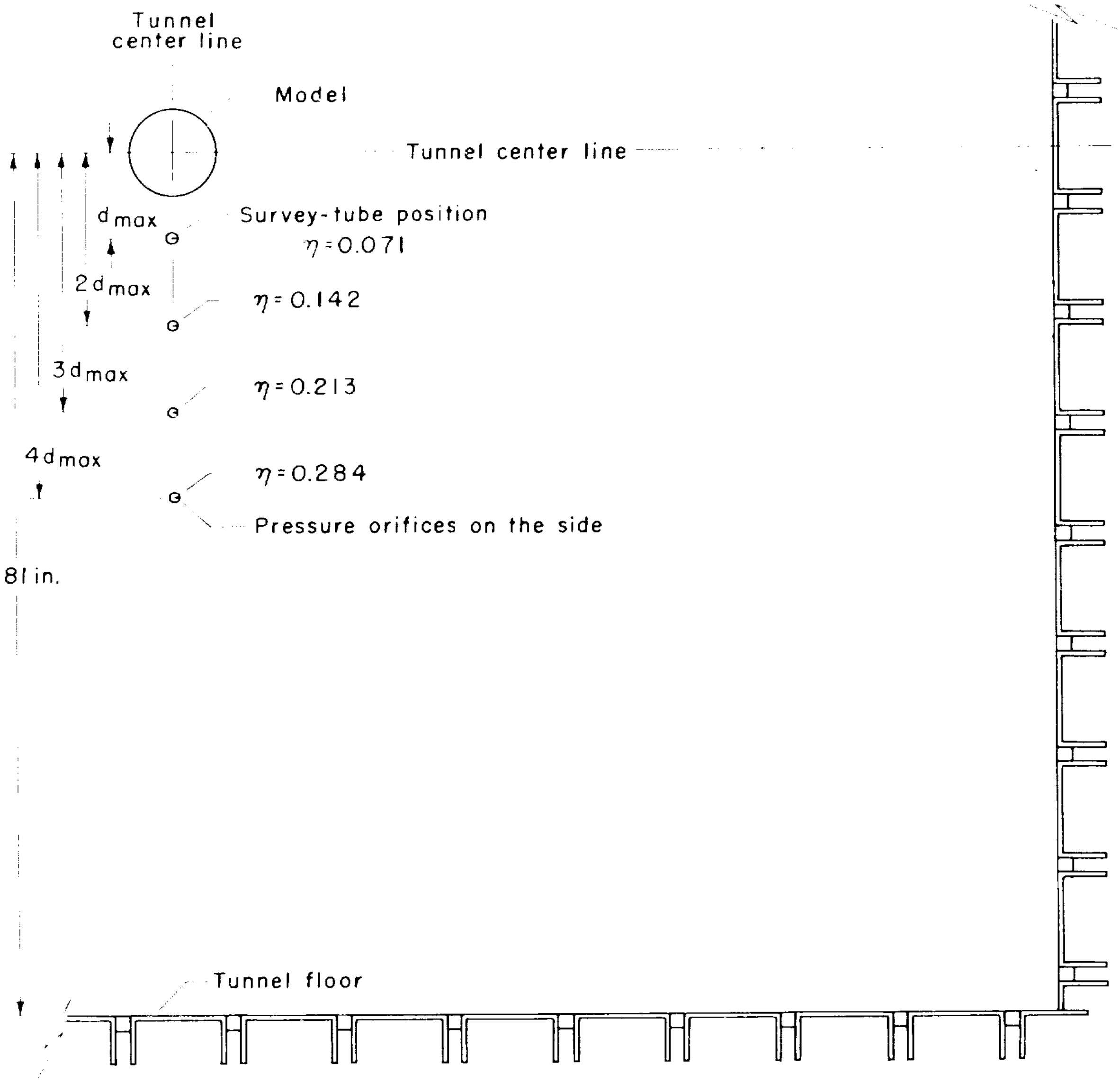

(b) Relative positions of the survey tube with respect to the model.

Figure 5.- Concluded.

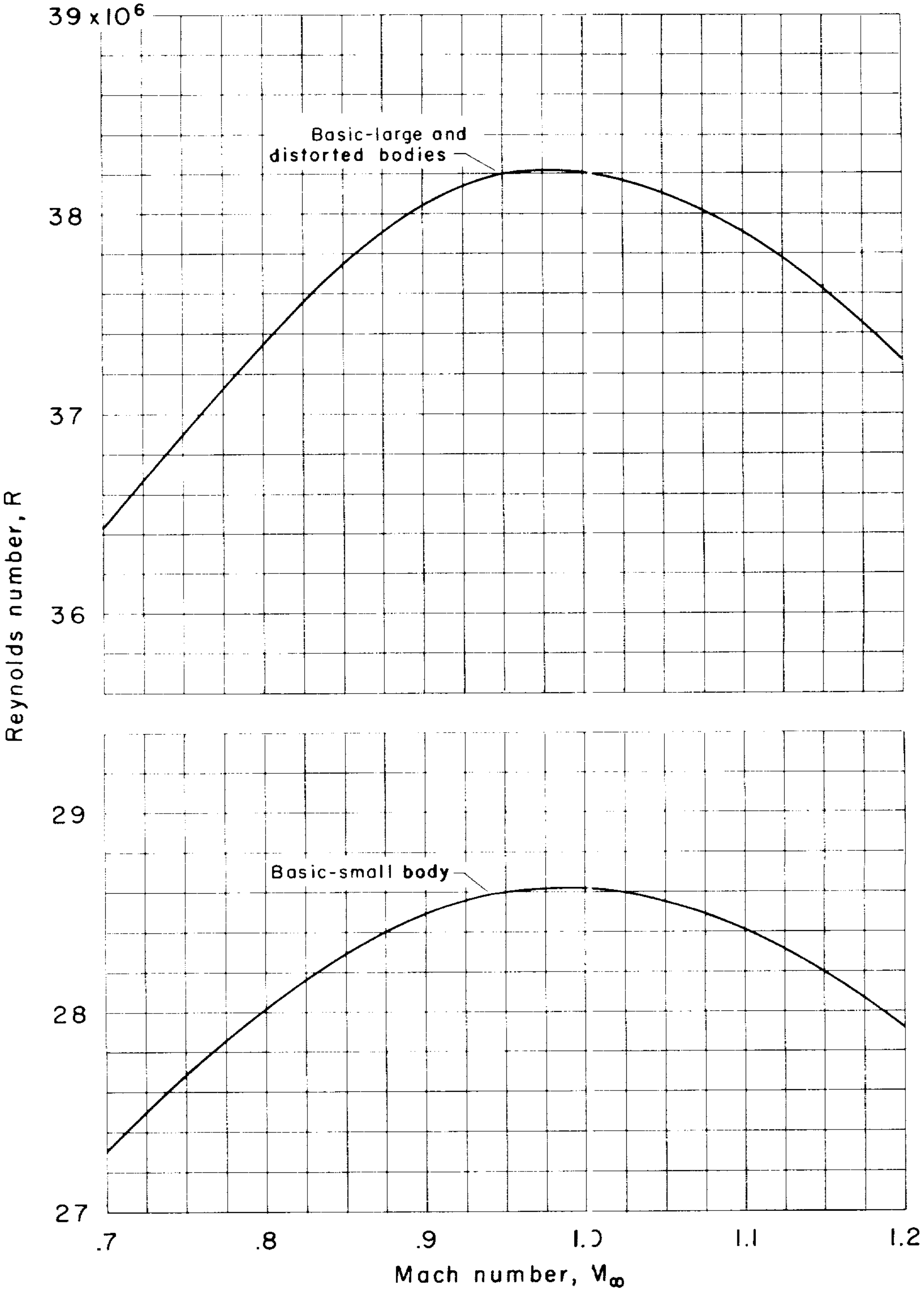

Figure 6.- Variation of Reynolds number with Mach number based on average temperatures.

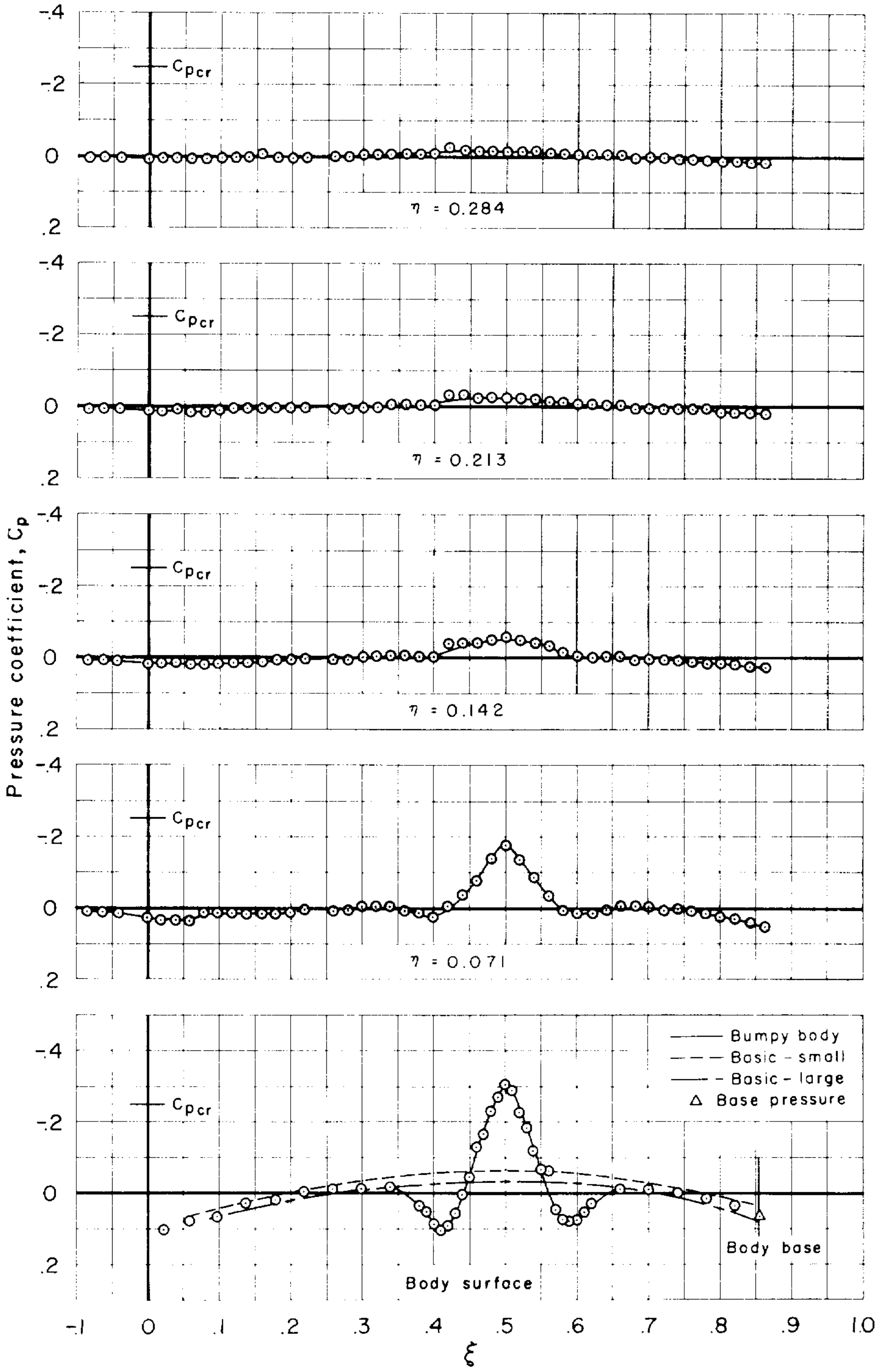

(a) M_{∞} = 80

Figure 7.- Pressure distributions for the basic and bumpy bodies.

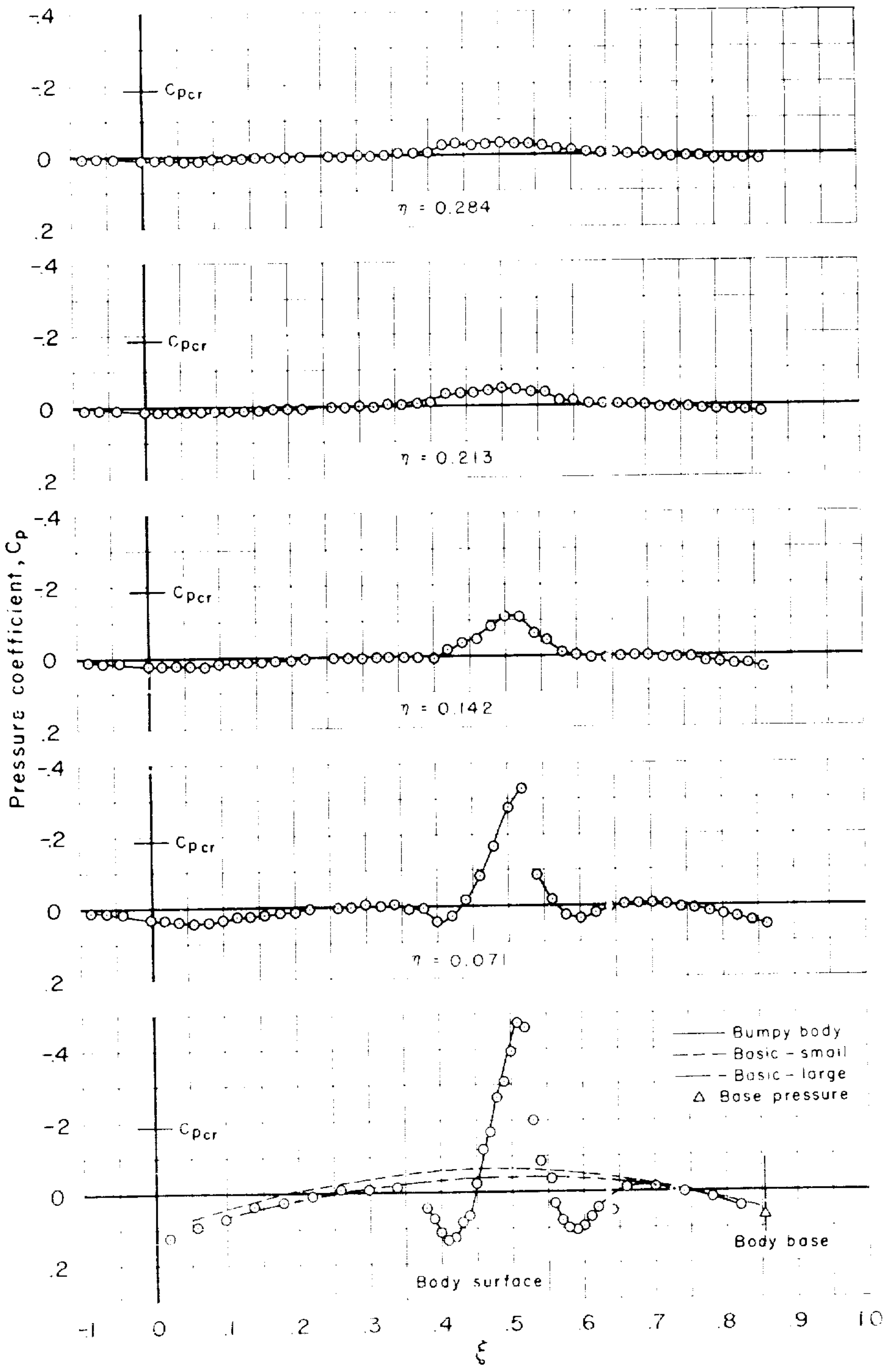

(b) M_∞ = 0.[illegible]

Figure 7.- Continued.

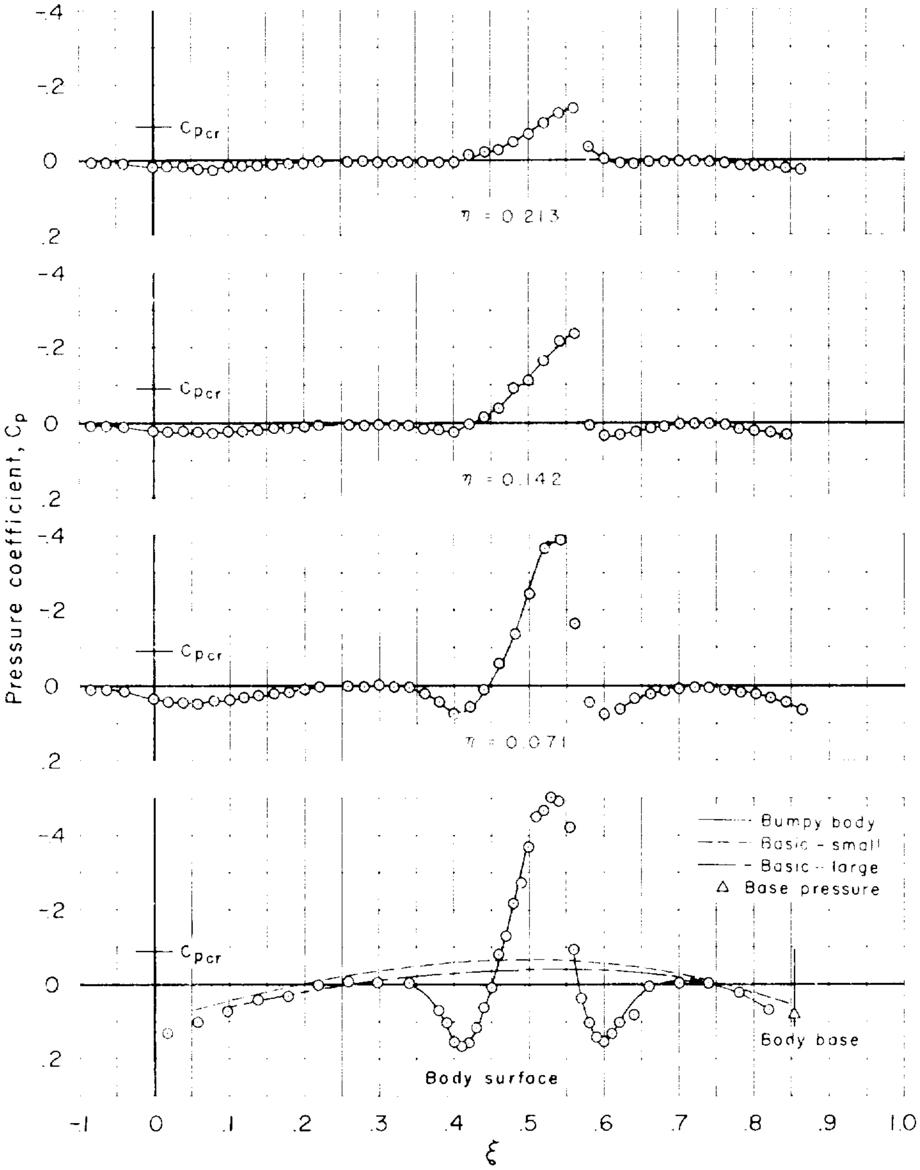

(c) M_∞ = 0.95

Figure 7.- Continued.

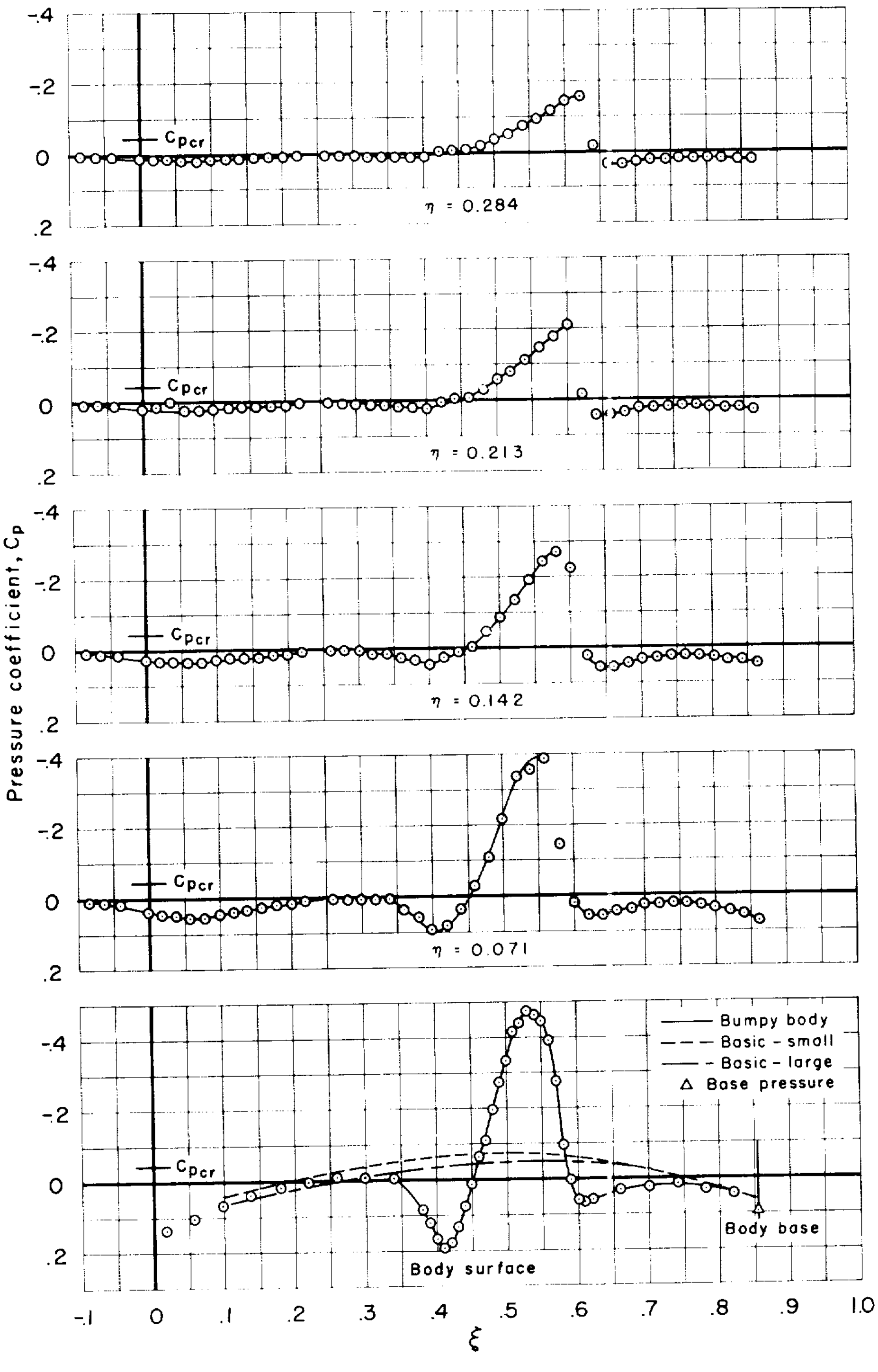

(d) $M_\infty = 0.975$

Figure 7.- Continued.

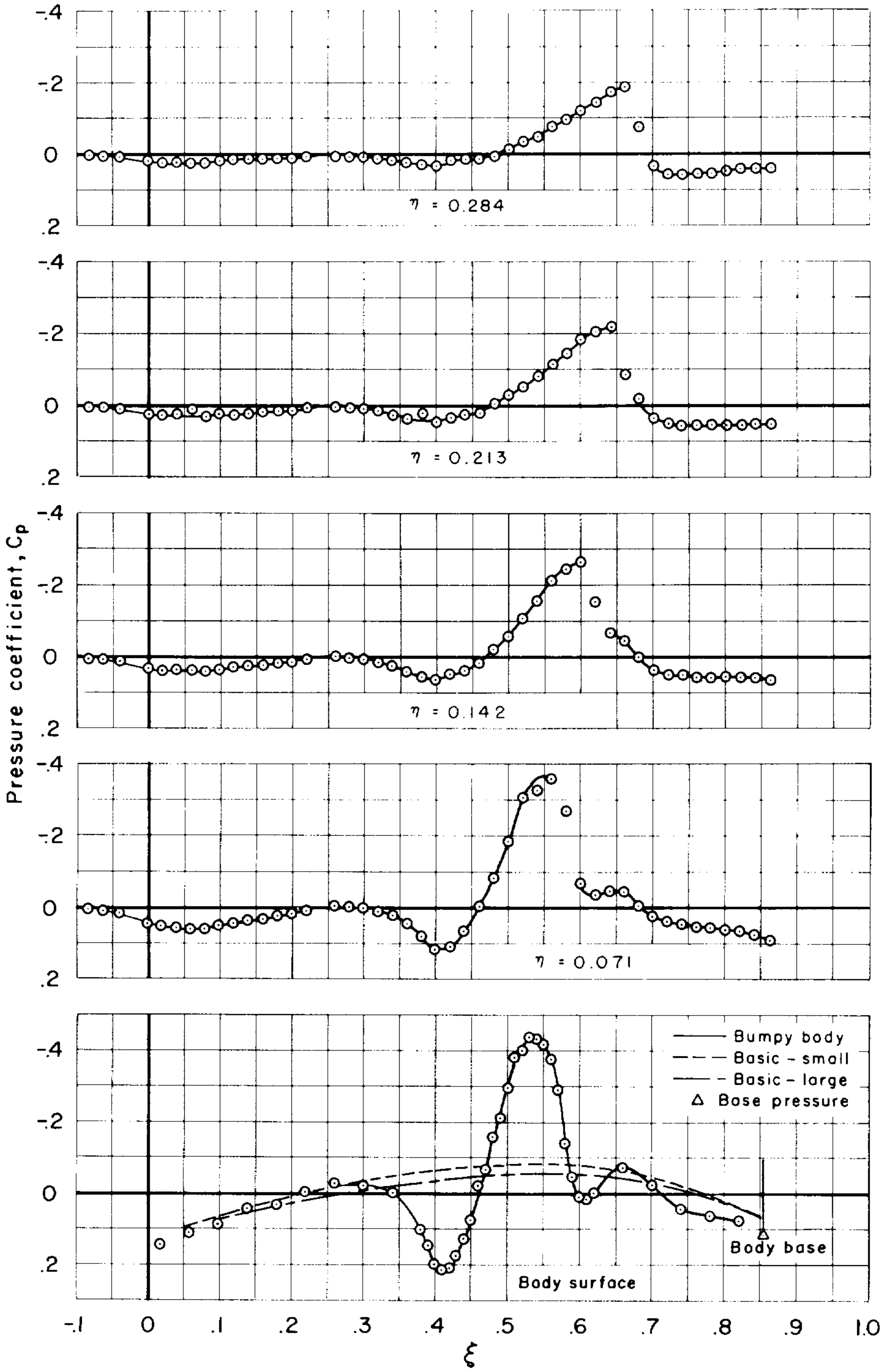

(e) $M_\infty = 1.0$

Figure 7.- Continued.

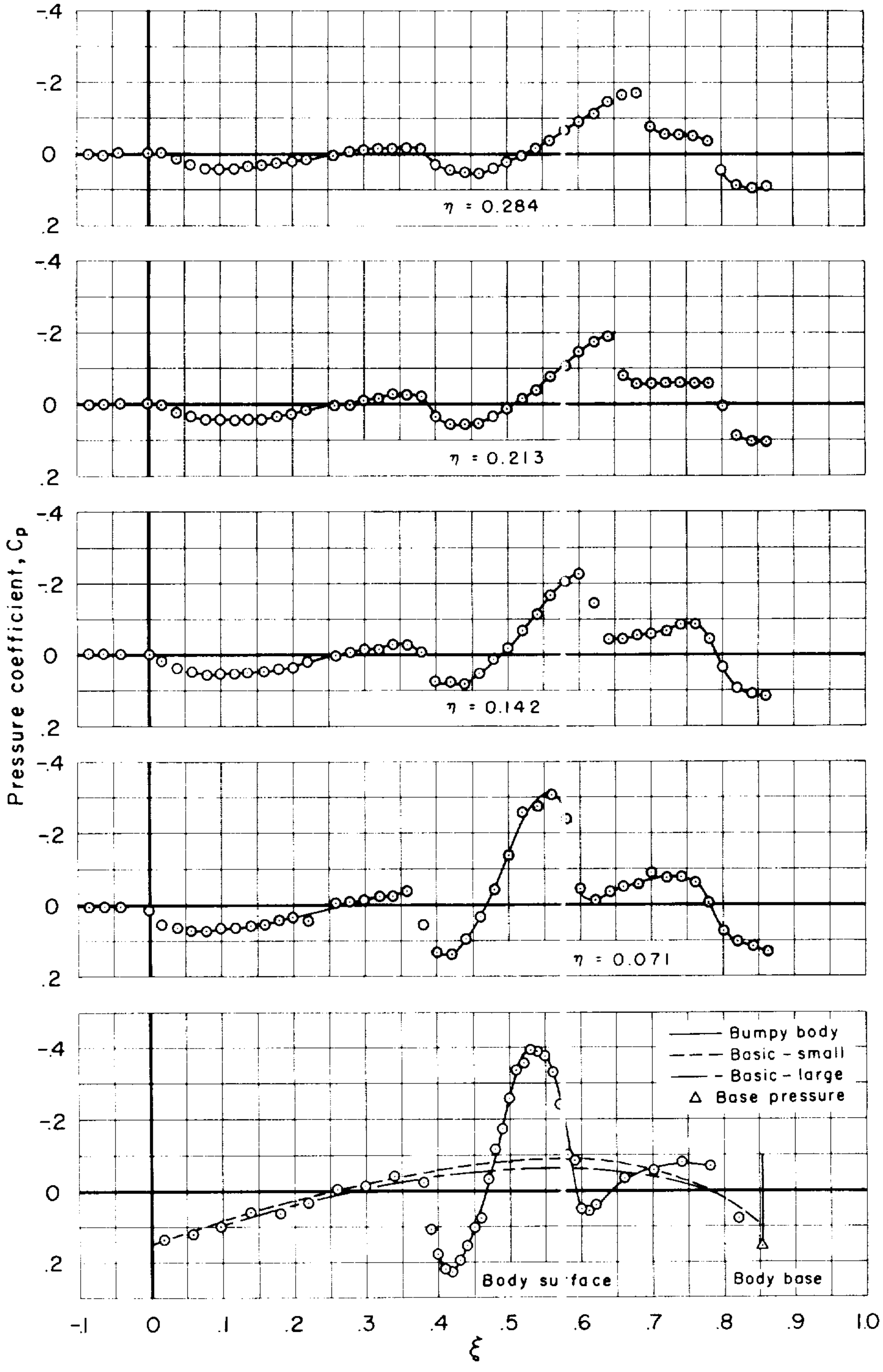

(f) $M_\infty = 1.025$

Figure 7.- Continued.

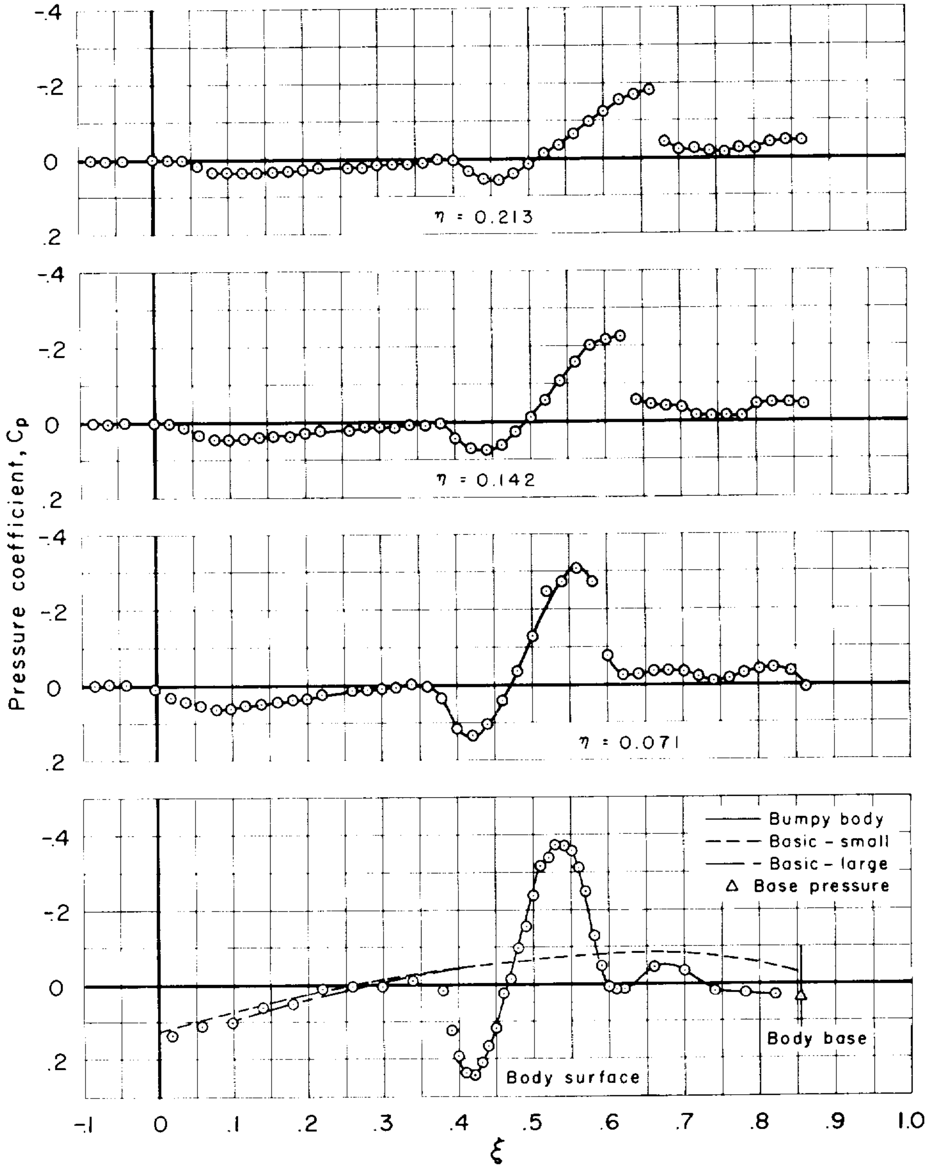

(g) $M_\infty = 1.05$

Figure 7.- Continued.

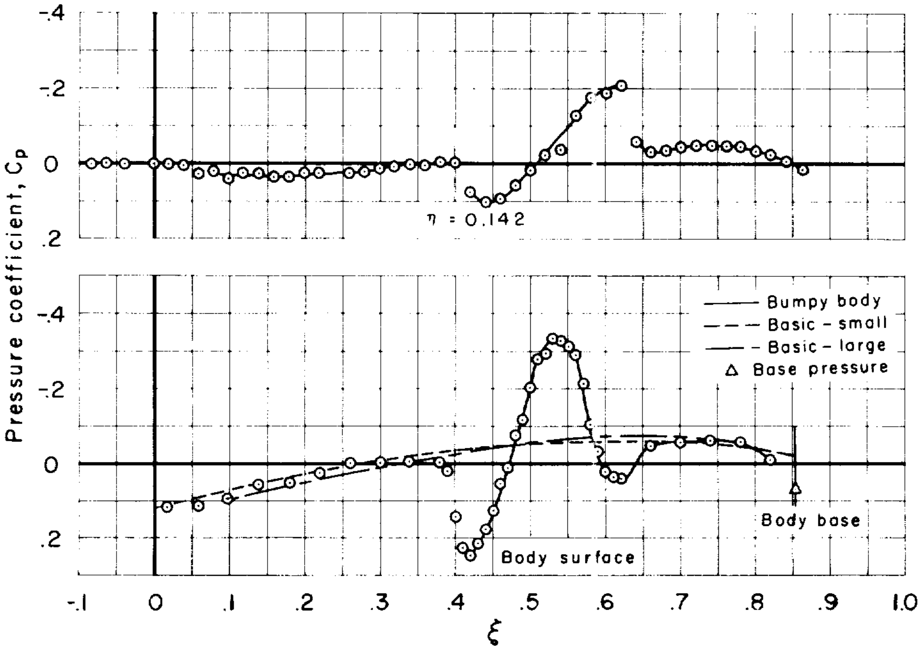

(h) M_∞ = 1.075

Figure 7.- Continued.

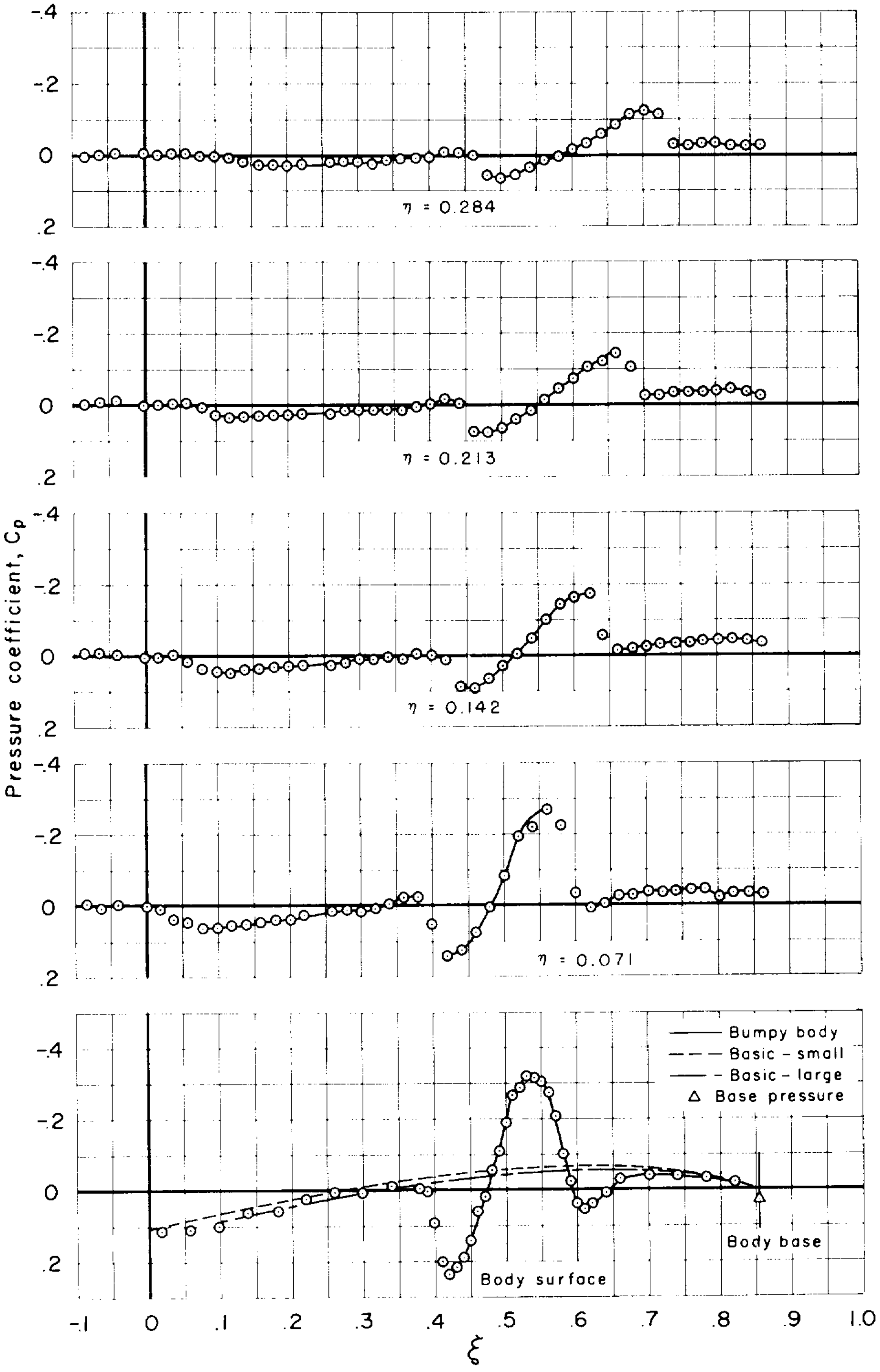

(i) $M_\infty = 1.10$

Figure 7.- Continued.

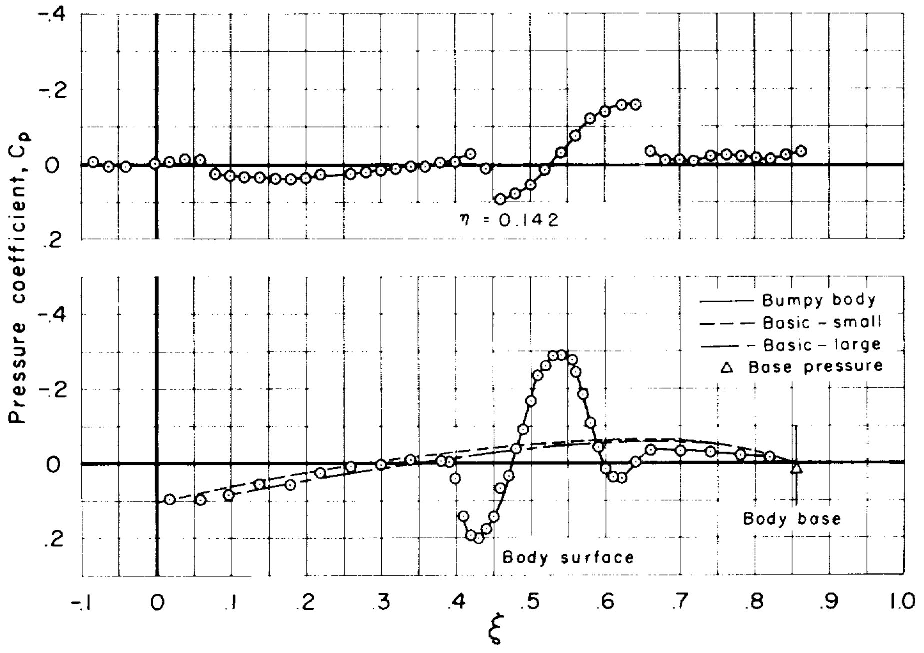

(j) $M_\infty = 1.15$

Figure 7.- Continued.

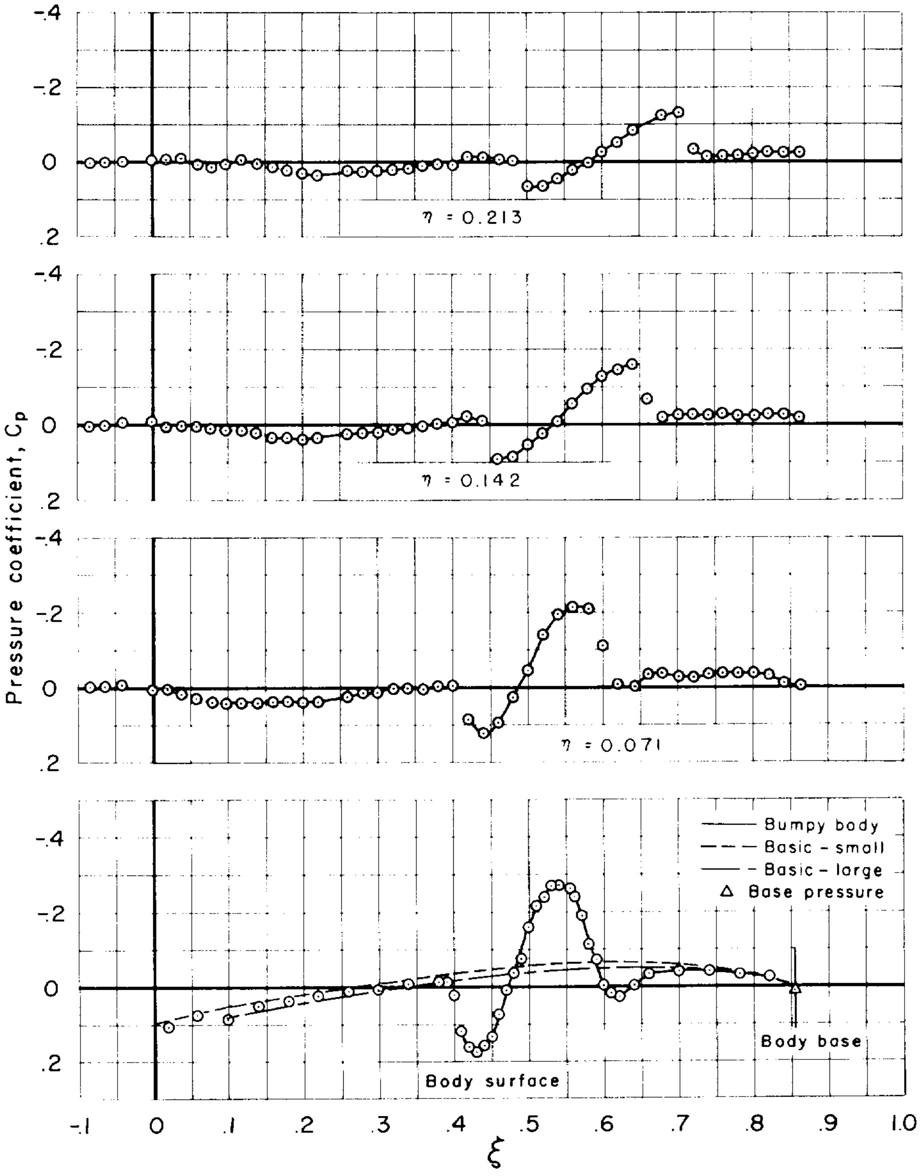

(k) $M_\infty = 1.20$

Figure 7.- Concluded.

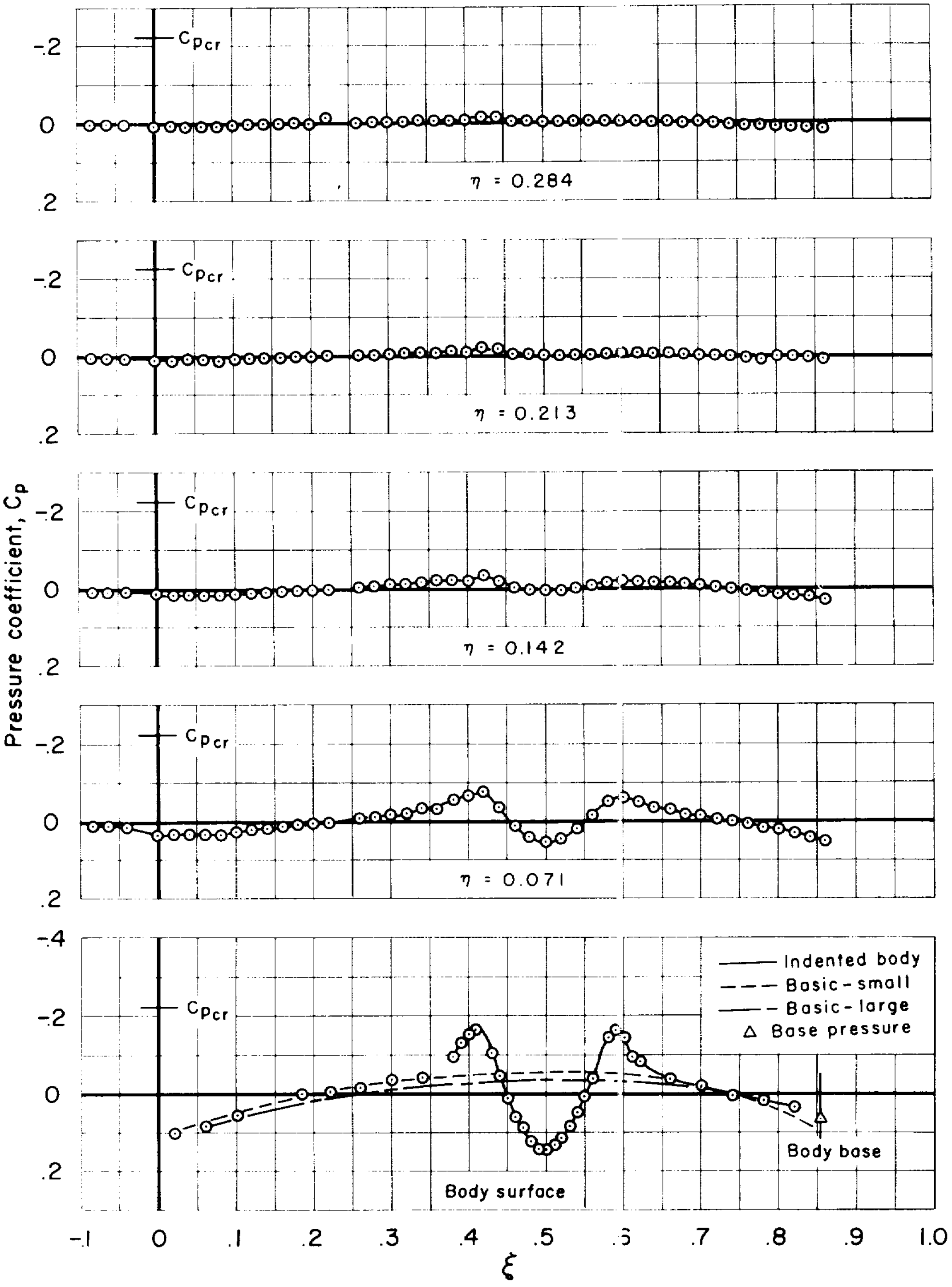

(a) $M_\infty = 0.80$

Figure 8.- Pressure distributions for the basic and indented bodies.

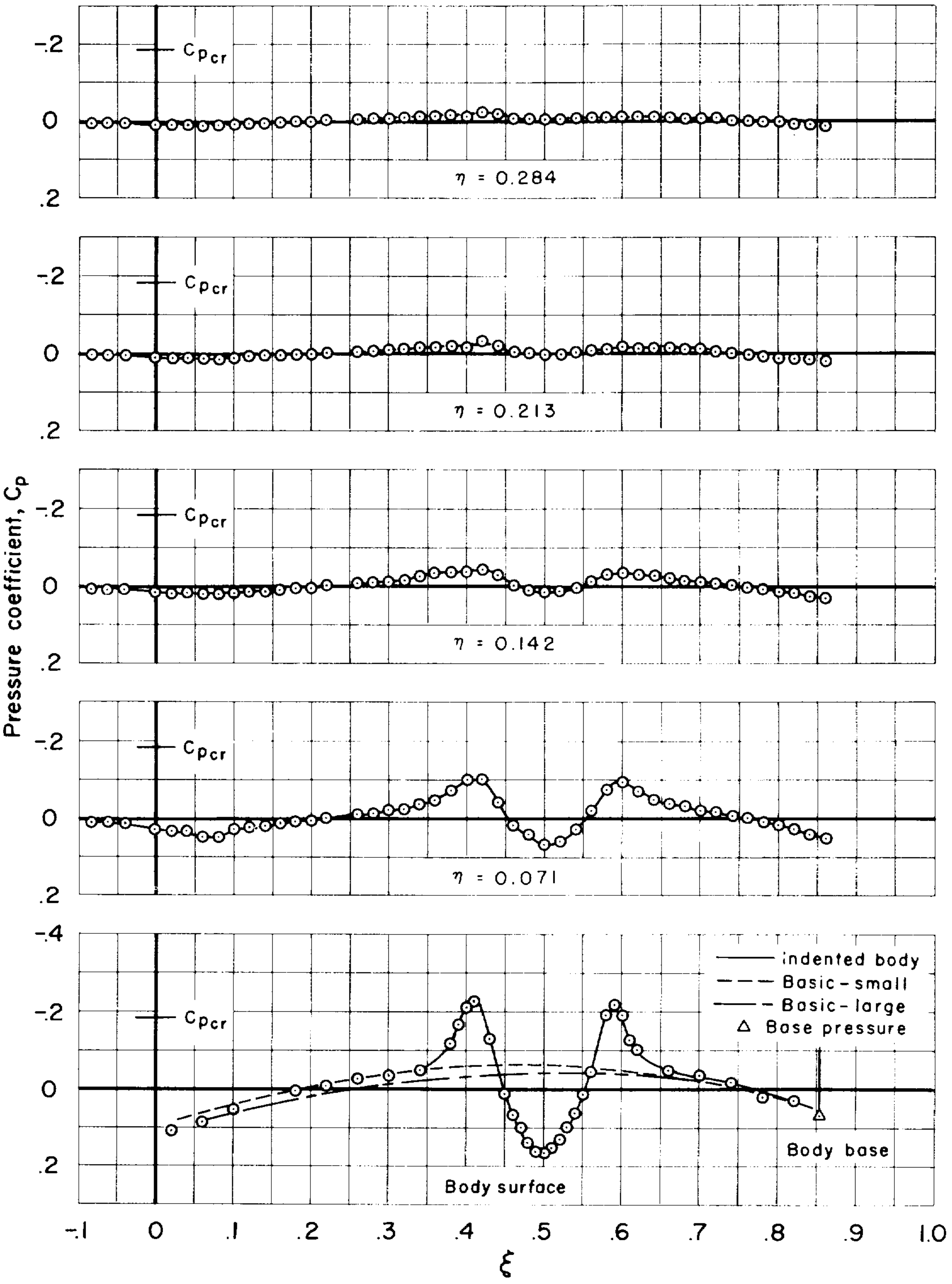

(b) M_∞ = 0.90

Figure 8.- Continued.

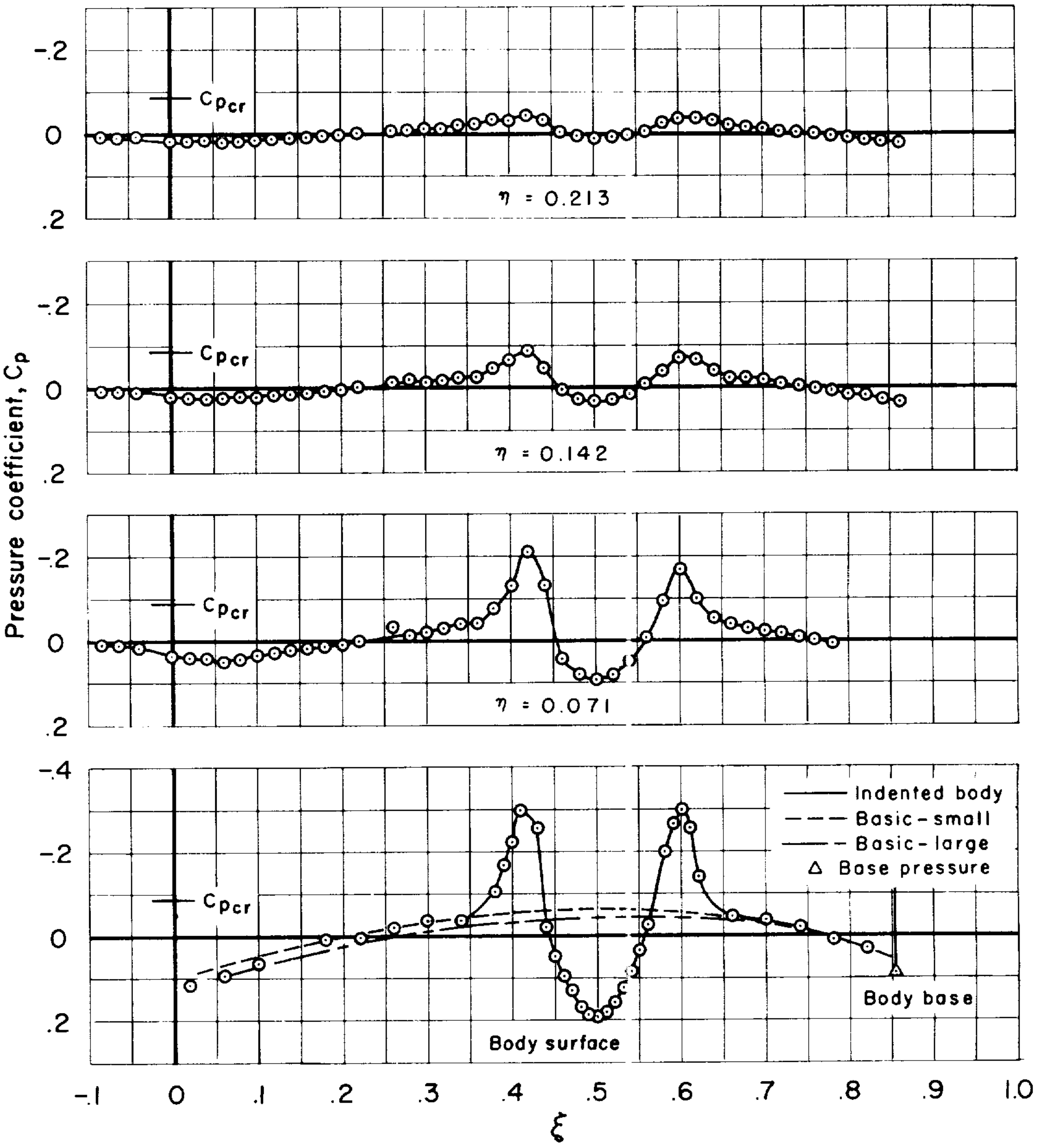

(c) $M_\infty = 0.95$

Figure 8.- Continued.

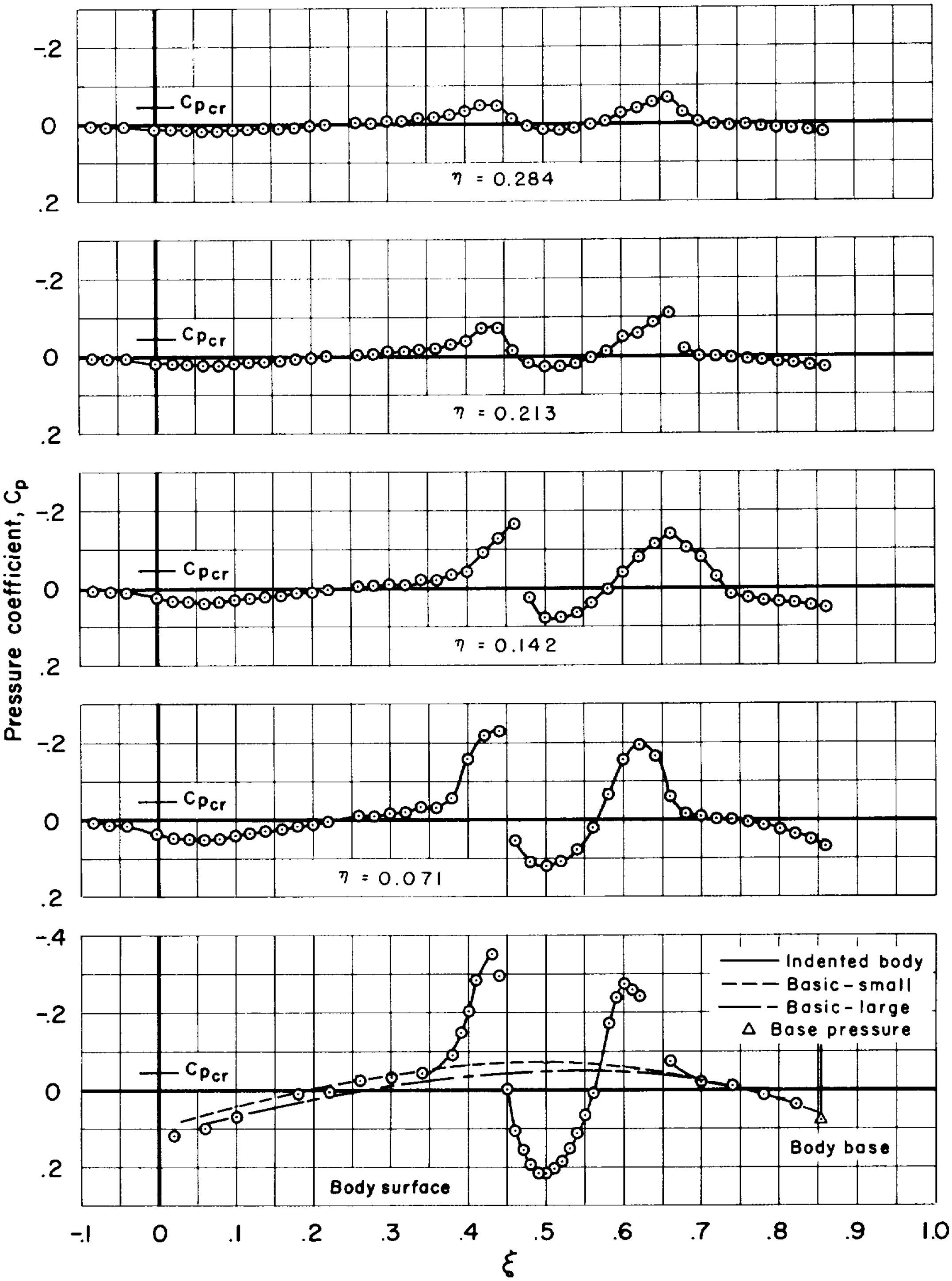

(d) $M_\infty = 0.975$

Figure 8.- Continued.

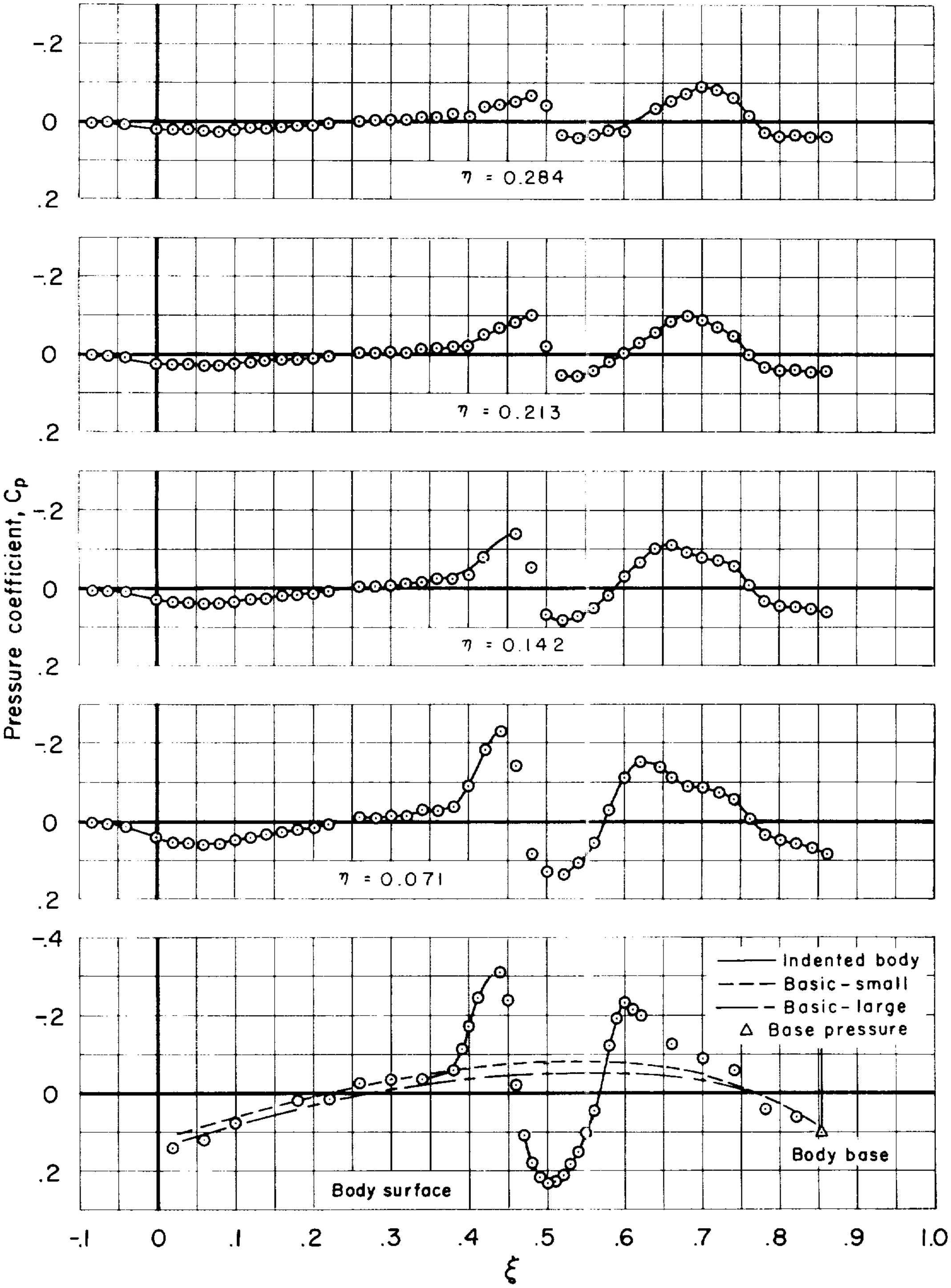

(e) $M_\infty = 1.0$

Figure 8.- Continued.

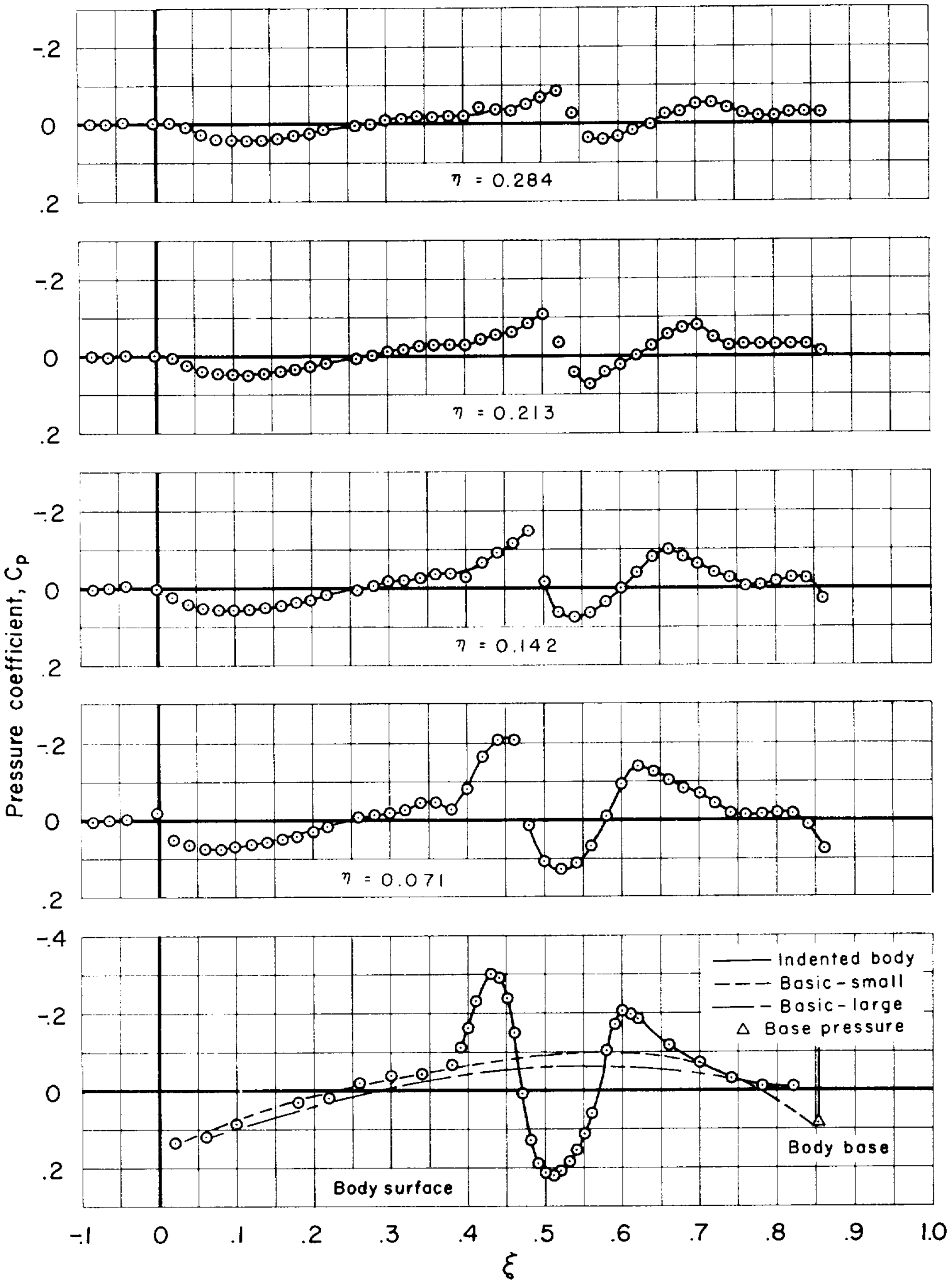

(f) $M_\infty = 1.025$

Figure 8.- Continued.

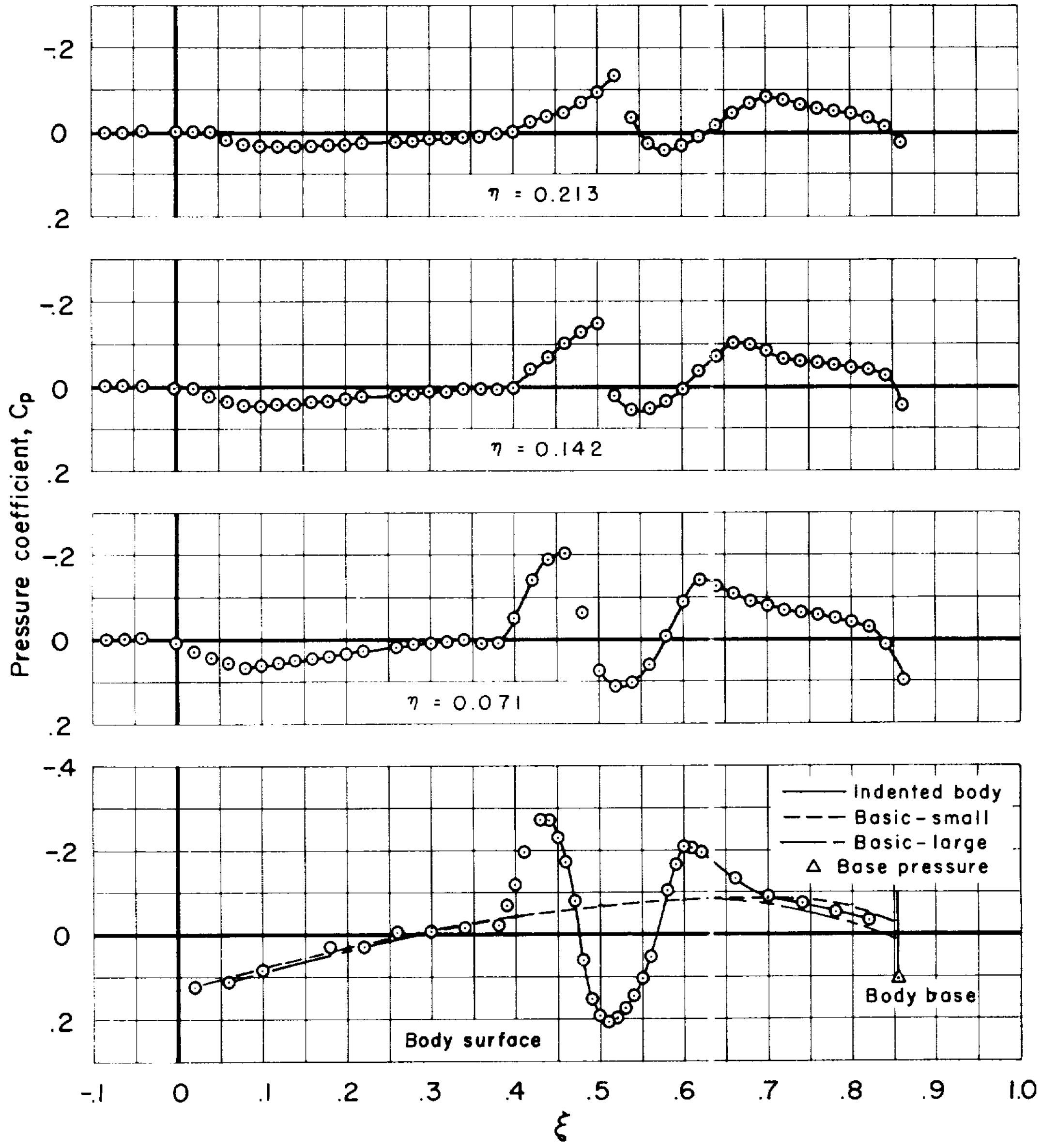

(g) $M_\infty = 1.05$

Figure 8.- Continued.

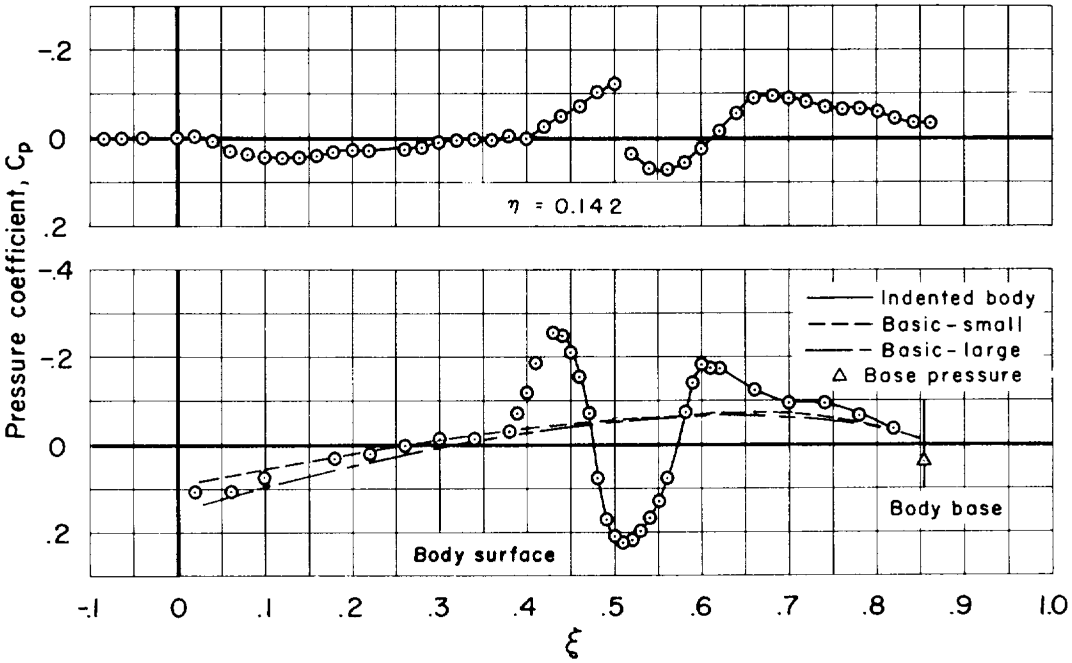

(h) $M_\infty = 1.075$

Figure 8.- Continued.

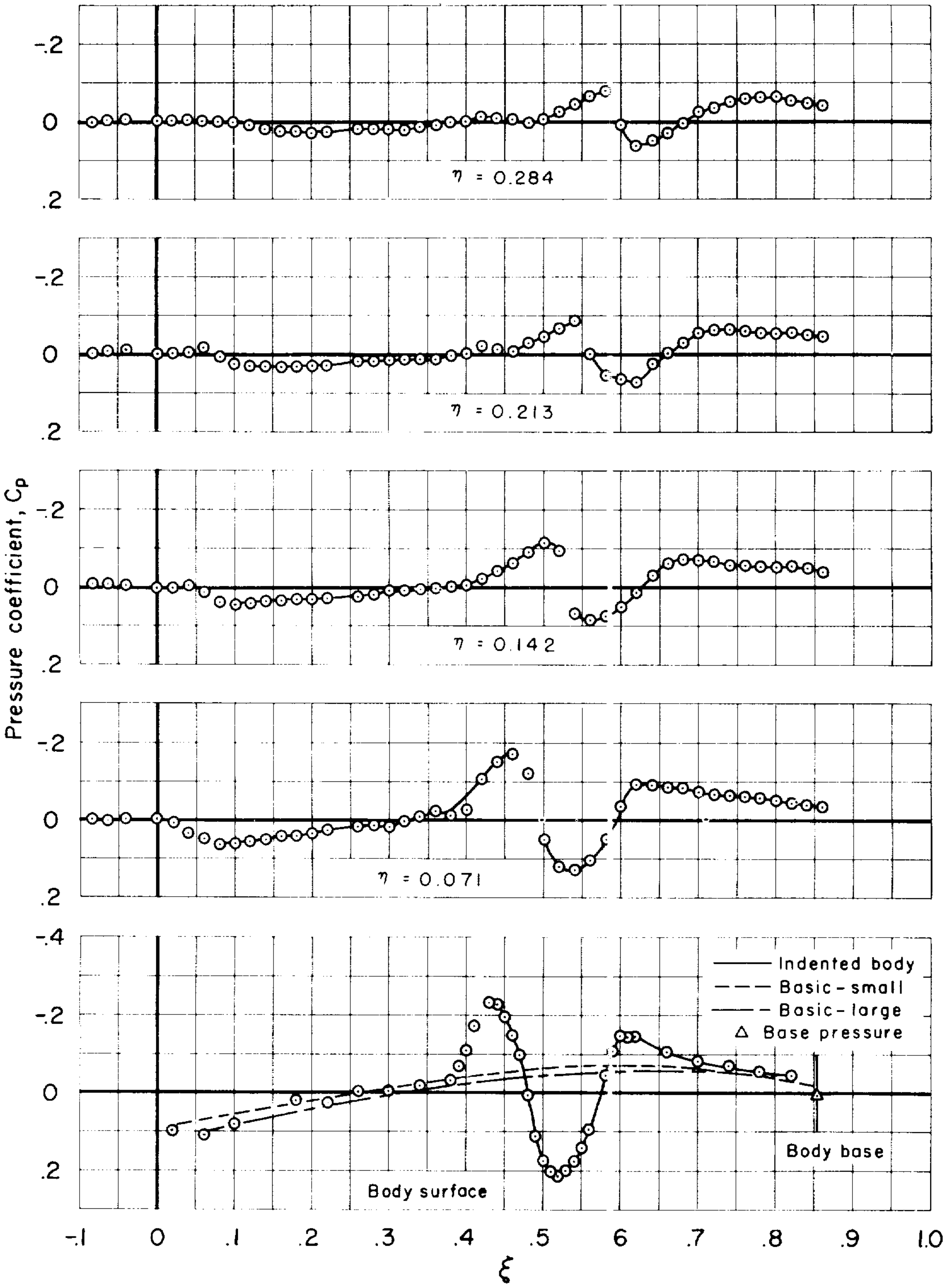

(i) $M_\infty = 1.10$

Figure 8.- Continued.

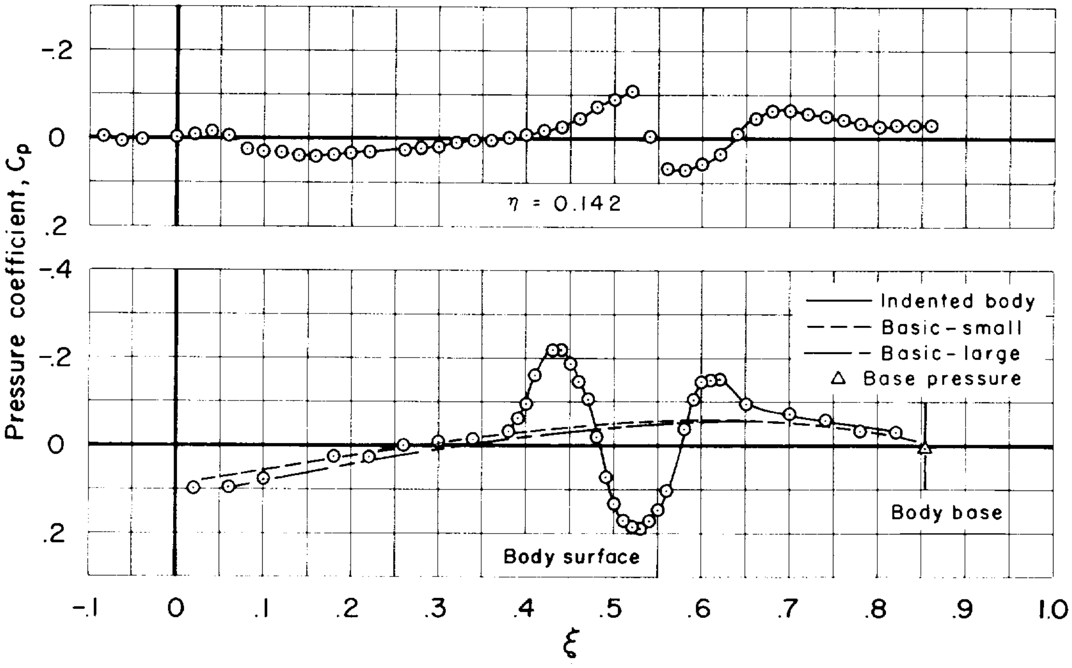

(j) $M_\infty = 1.15$

Figure 8.- Continued.

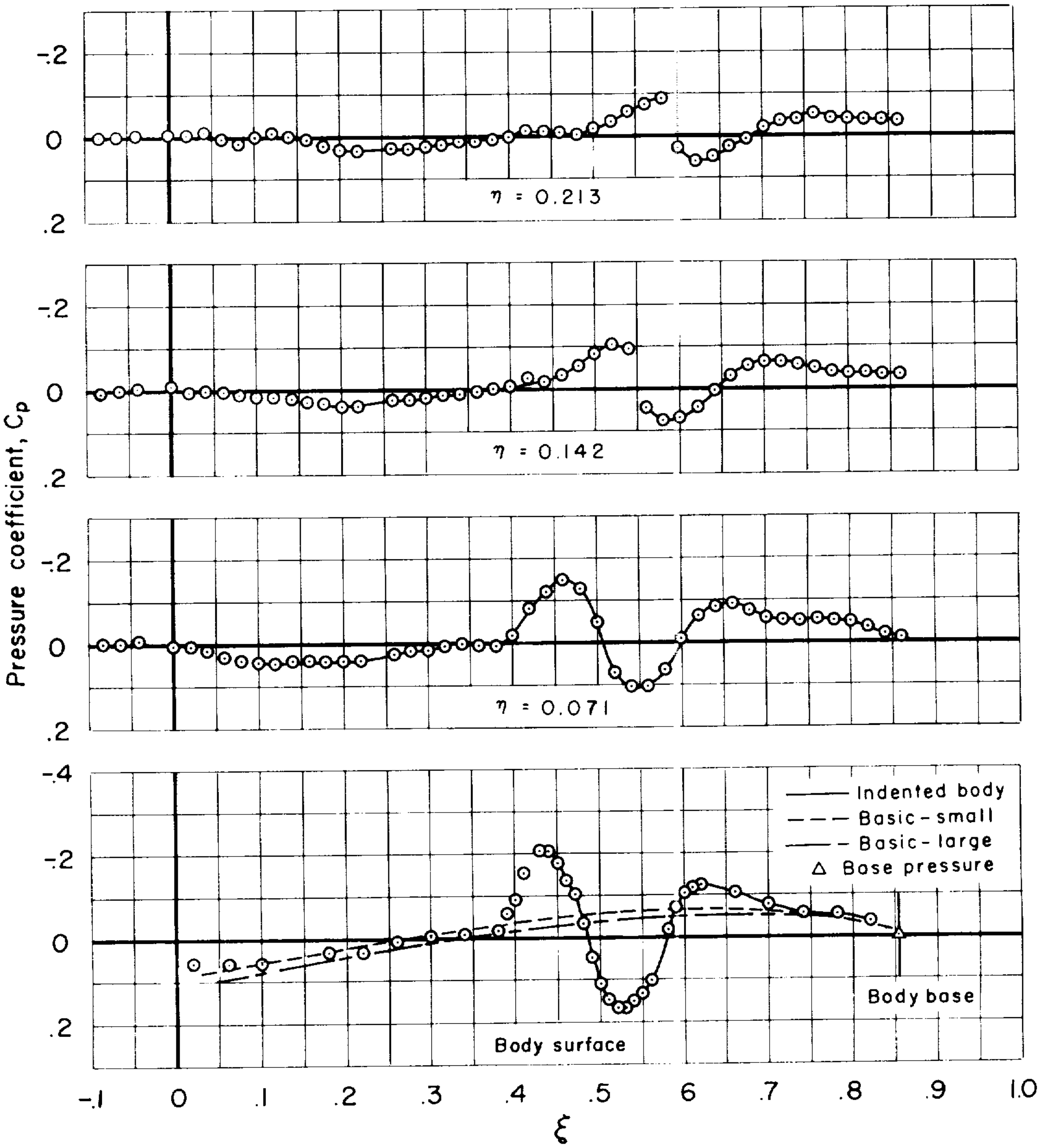

(k) $M_\infty = 1.20$

Figure 8.- Concluded.

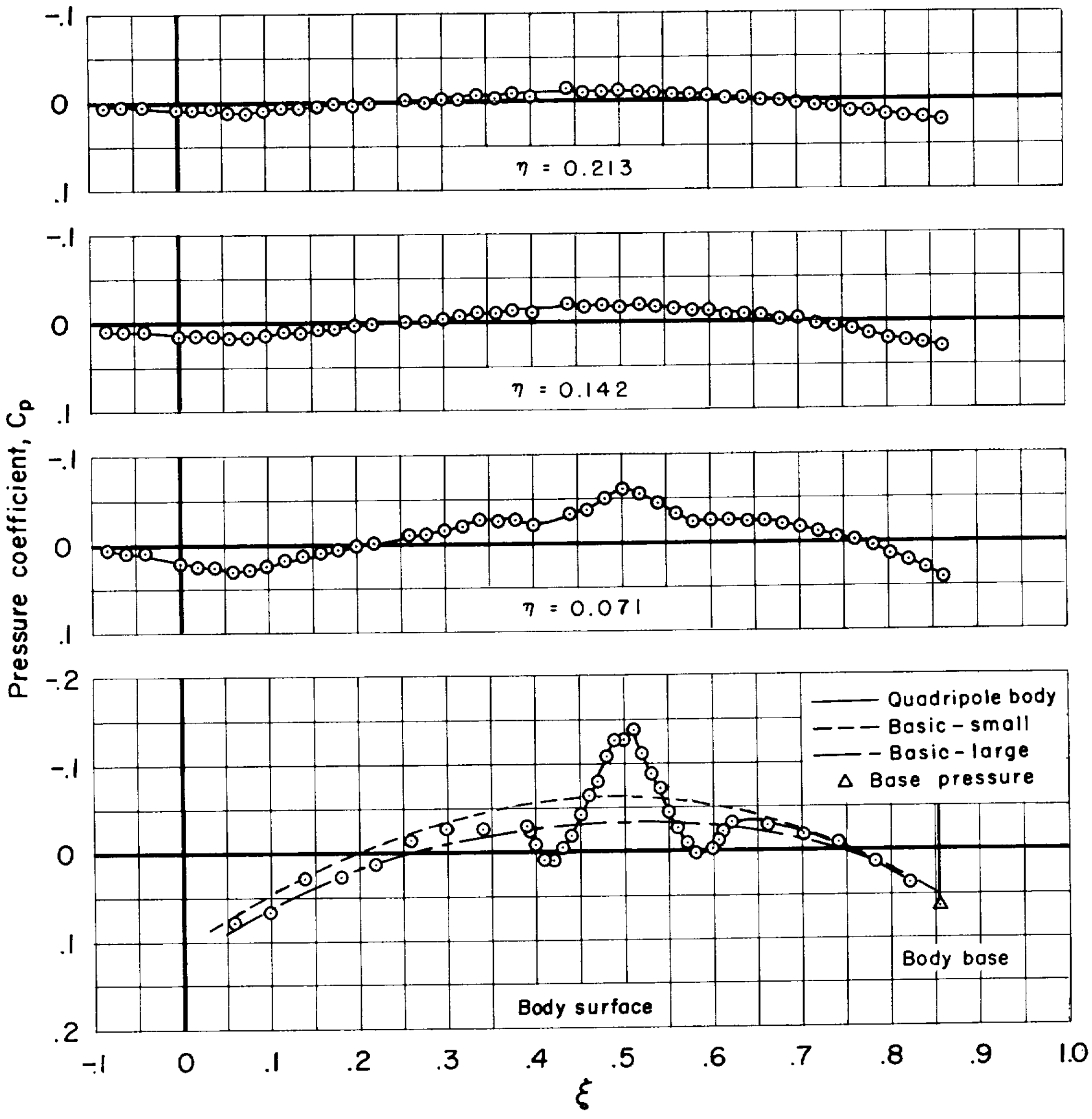

(a) $M_\infty = 0.80$, $\theta = 0^\circ$

Figure 9.- Pressure distributions for the basic and quadripole bodies.

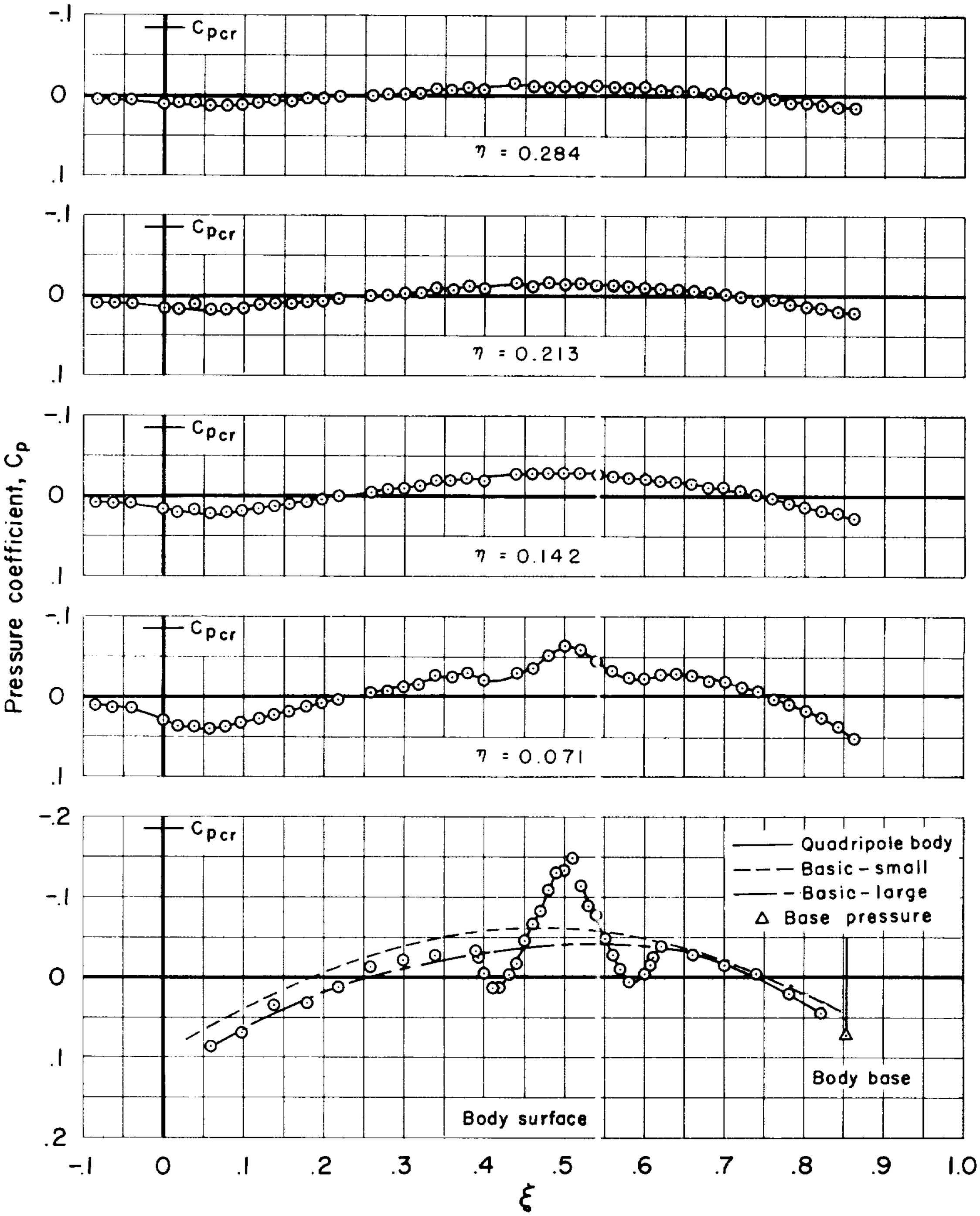

(b) $M_\infty = 0.90$, $\theta = 0^{\circ}$

Figure 9.- Continued.

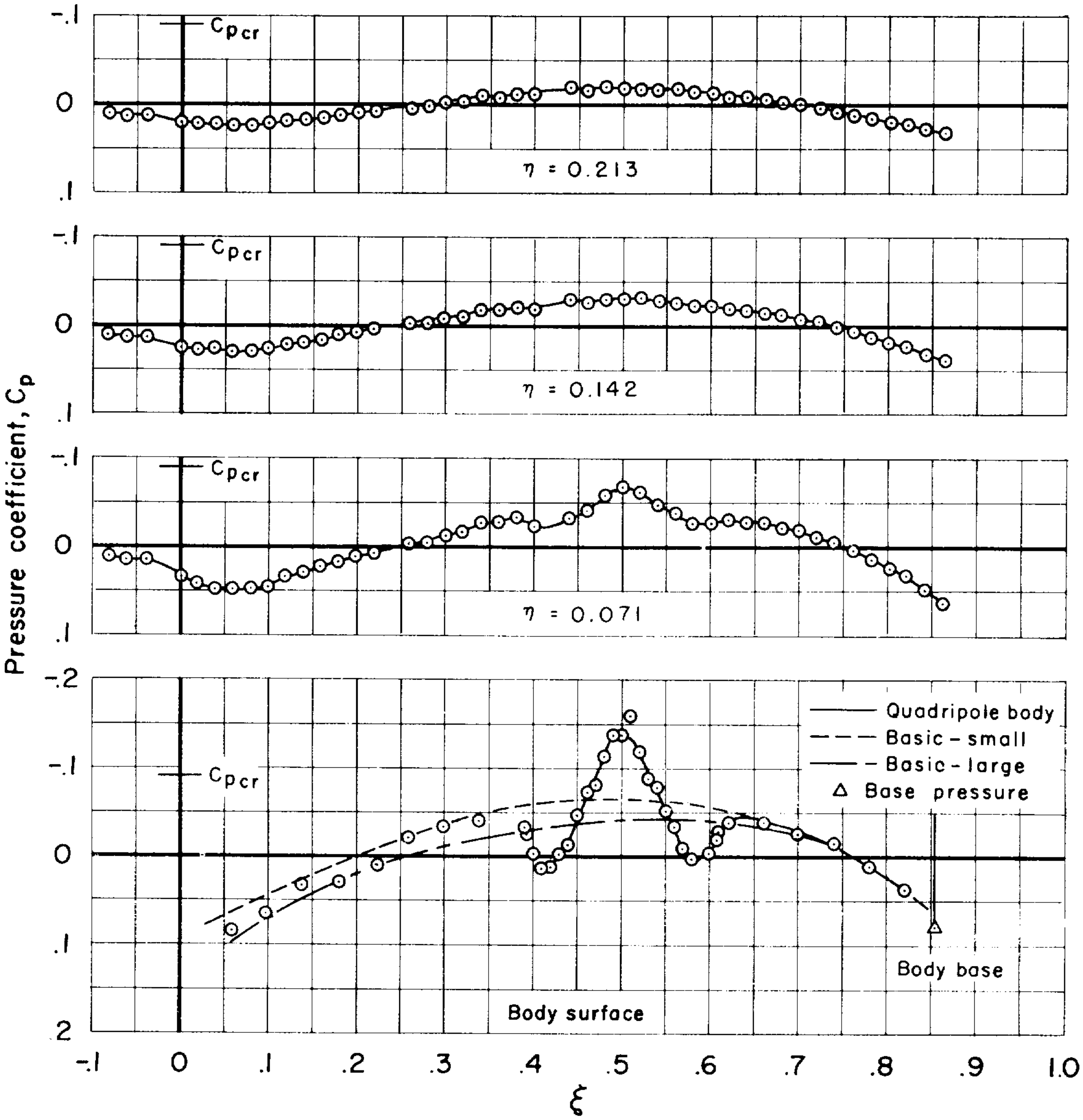

(c) $M_\infty = 0.95$, $\theta = 0^\circ$

Figure 9.- Continued.

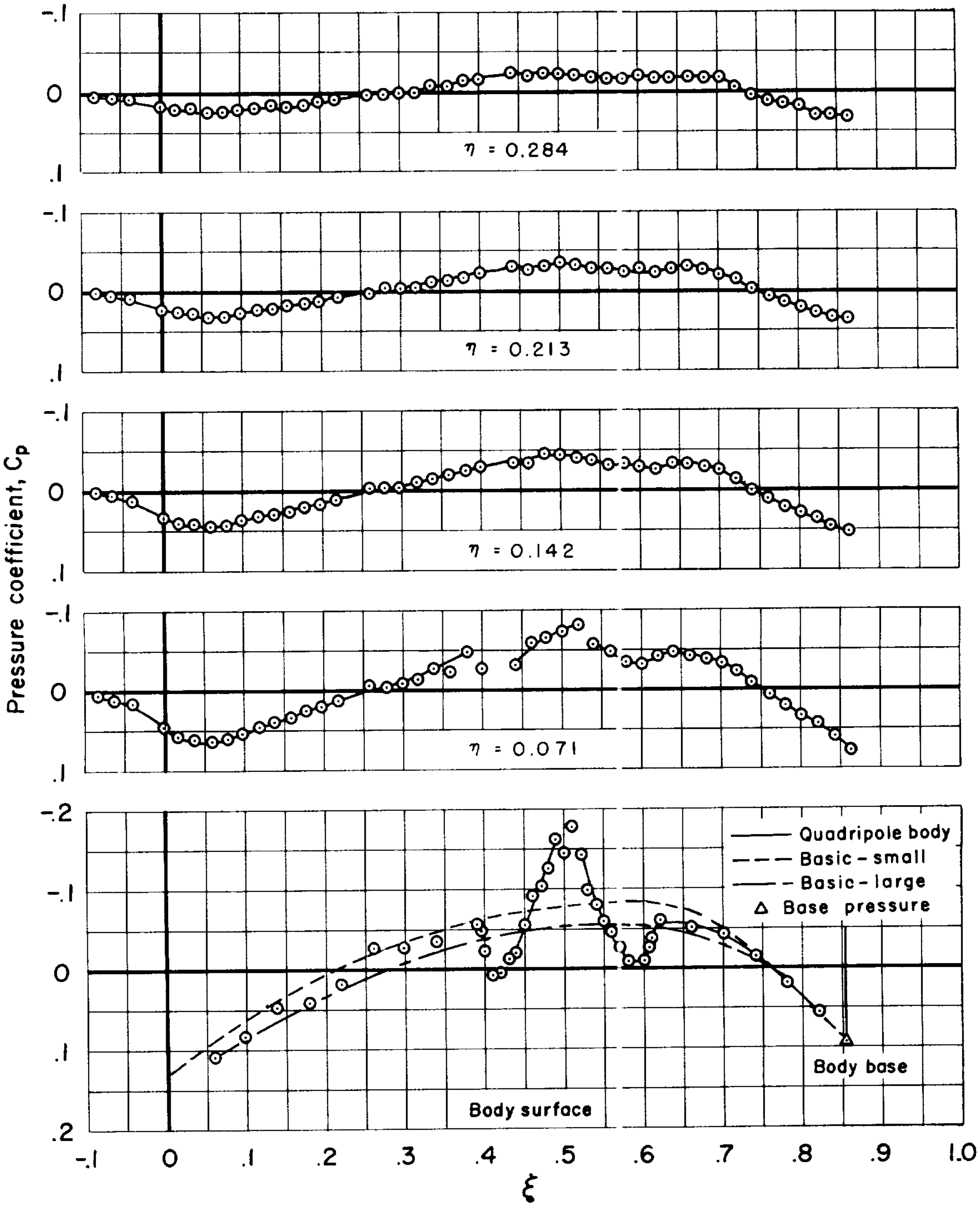

(d) $M_\infty = 1.0$, $\theta = 0^\circ$

Figure 9.- Continued.

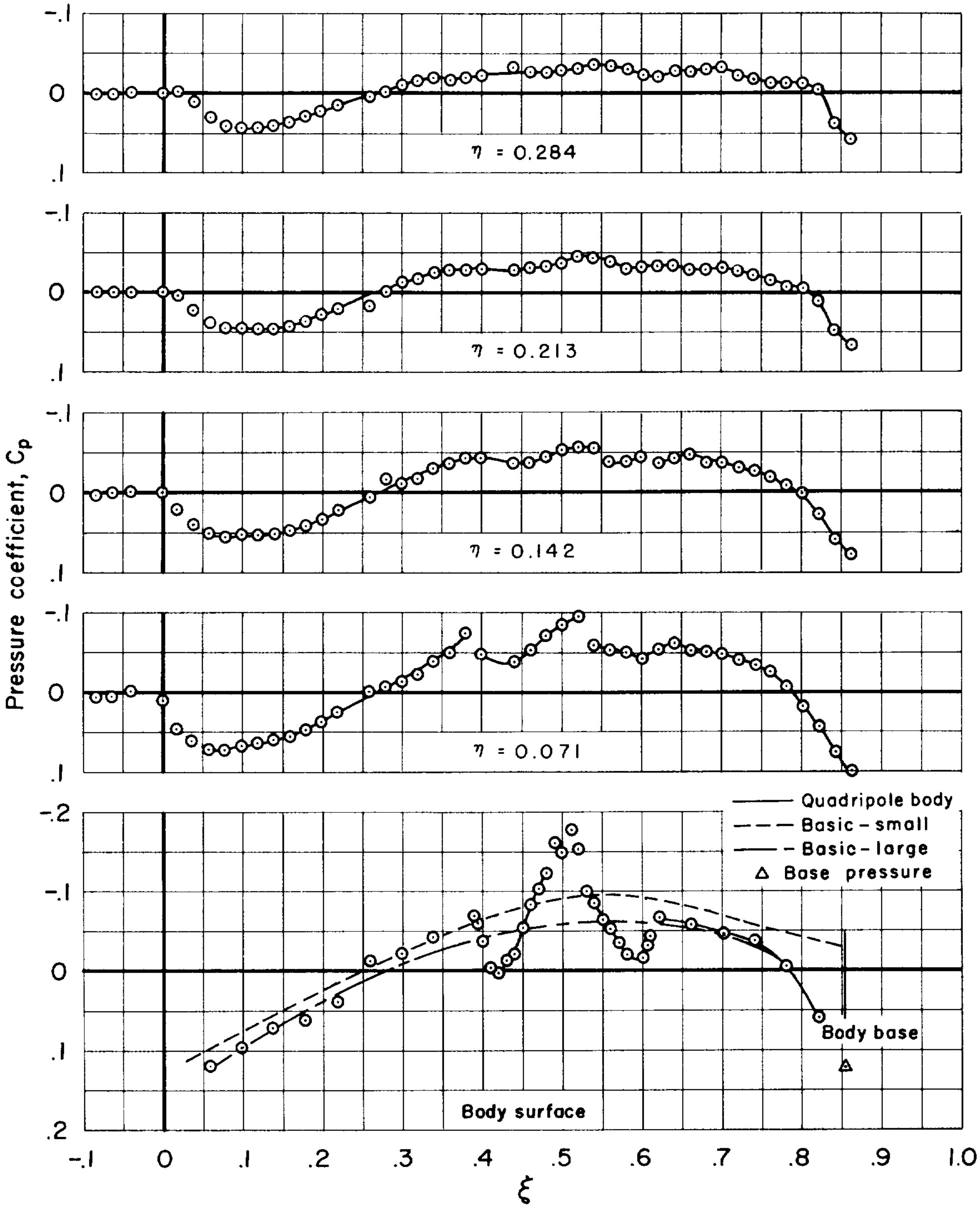

(e) $M_\infty = 1.025$, $\theta = 0^\circ$

Figure 9.- Continued.

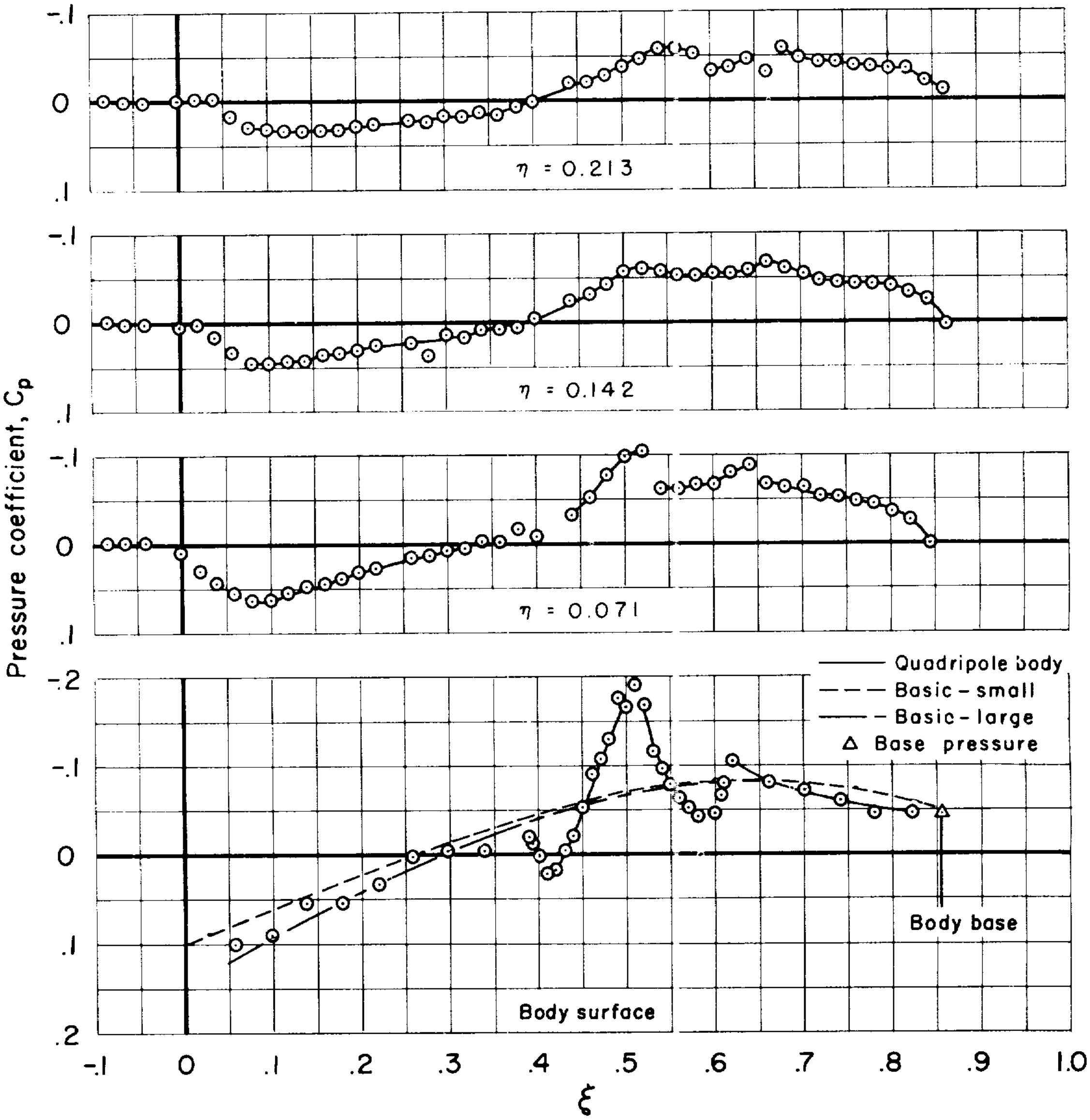

(f) $M_{\infty} = 1.05$, $\theta = 0^{\circ}$

Figure 9.- Continued.

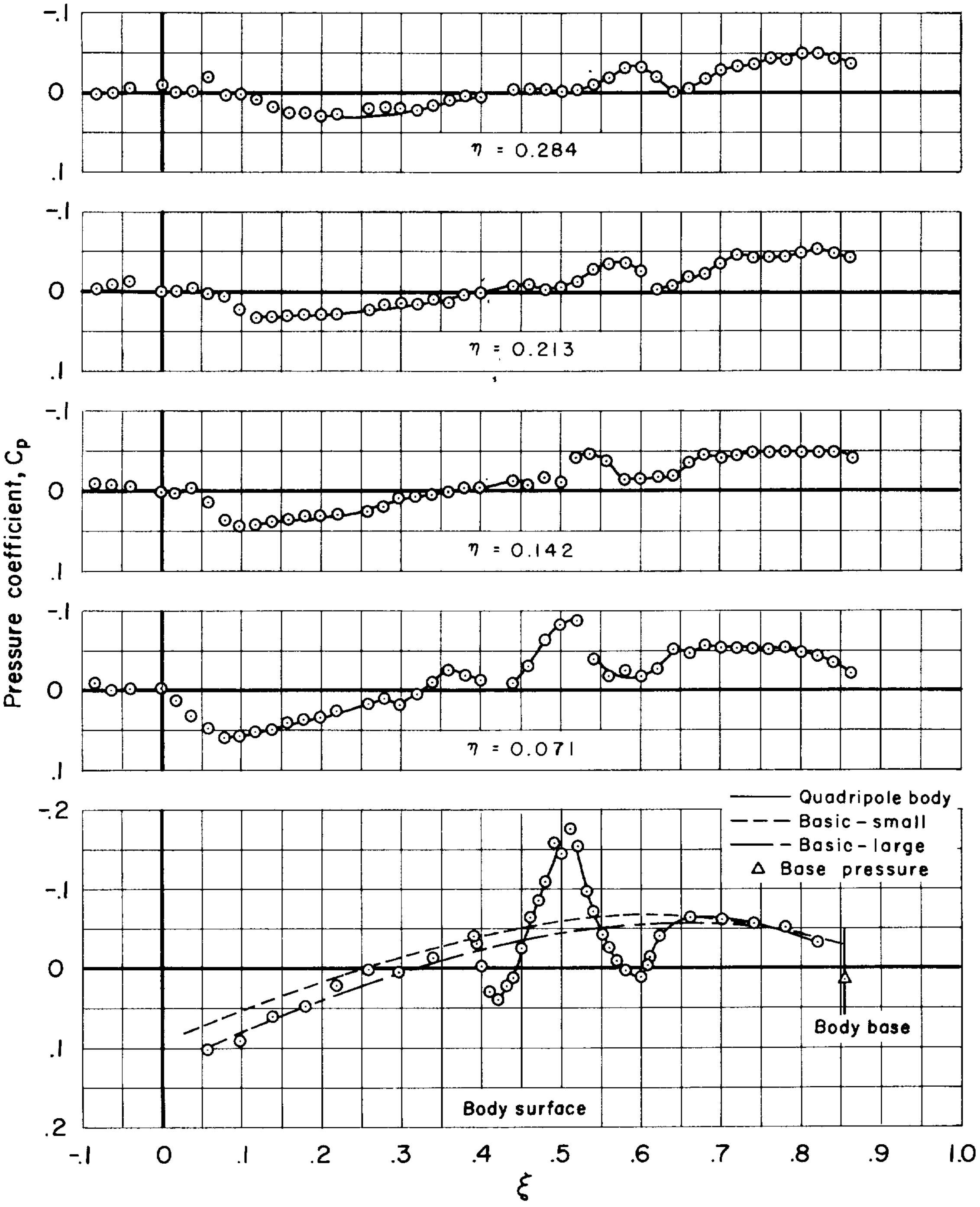

(g) $M_\infty = 1.10$, $\theta = 0^\circ$

Figure 9.- Continued.

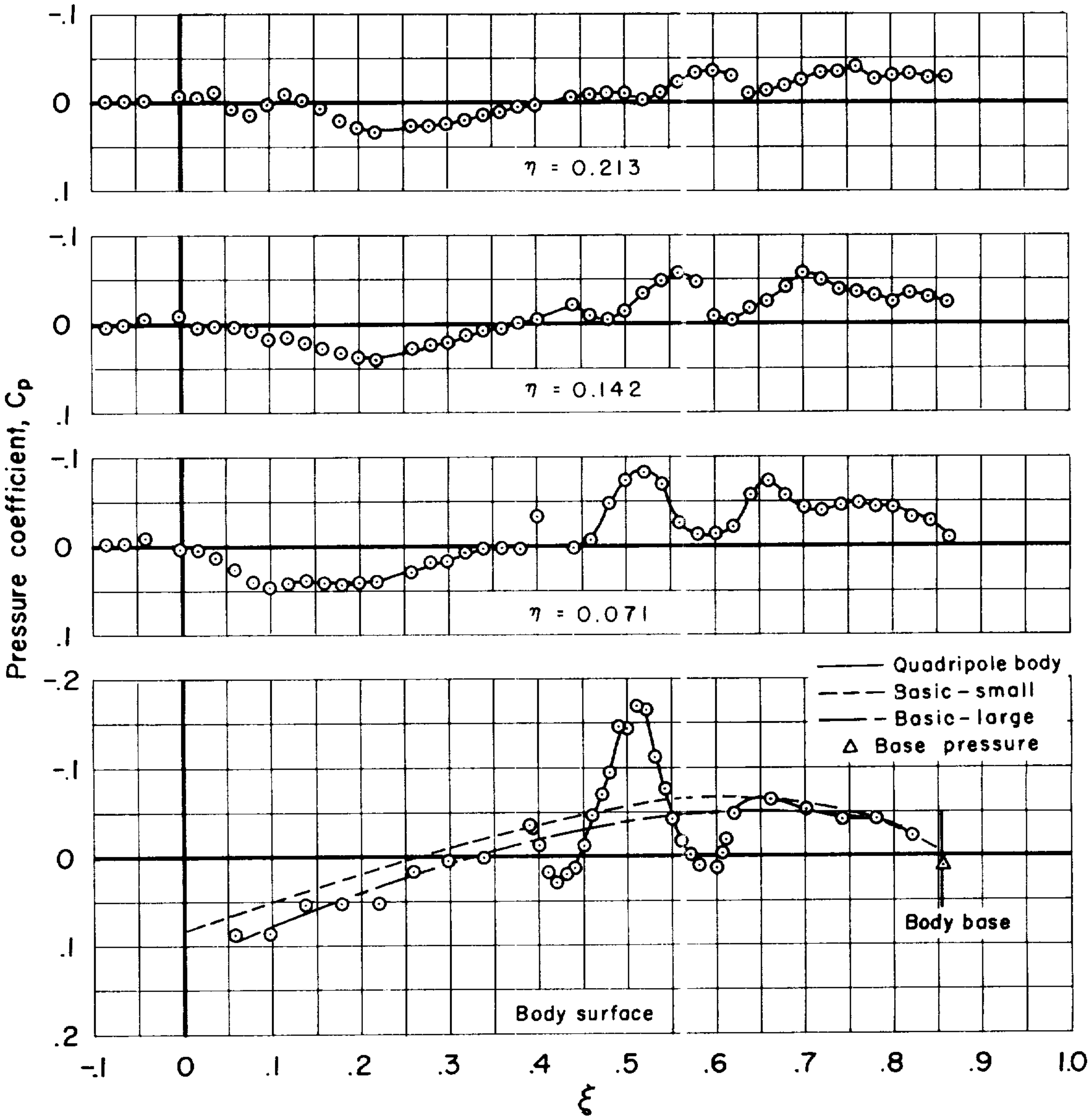

(h) $M_\infty = 1.20$, $\theta = 0^\circ$

Figure 9.- Concluded.

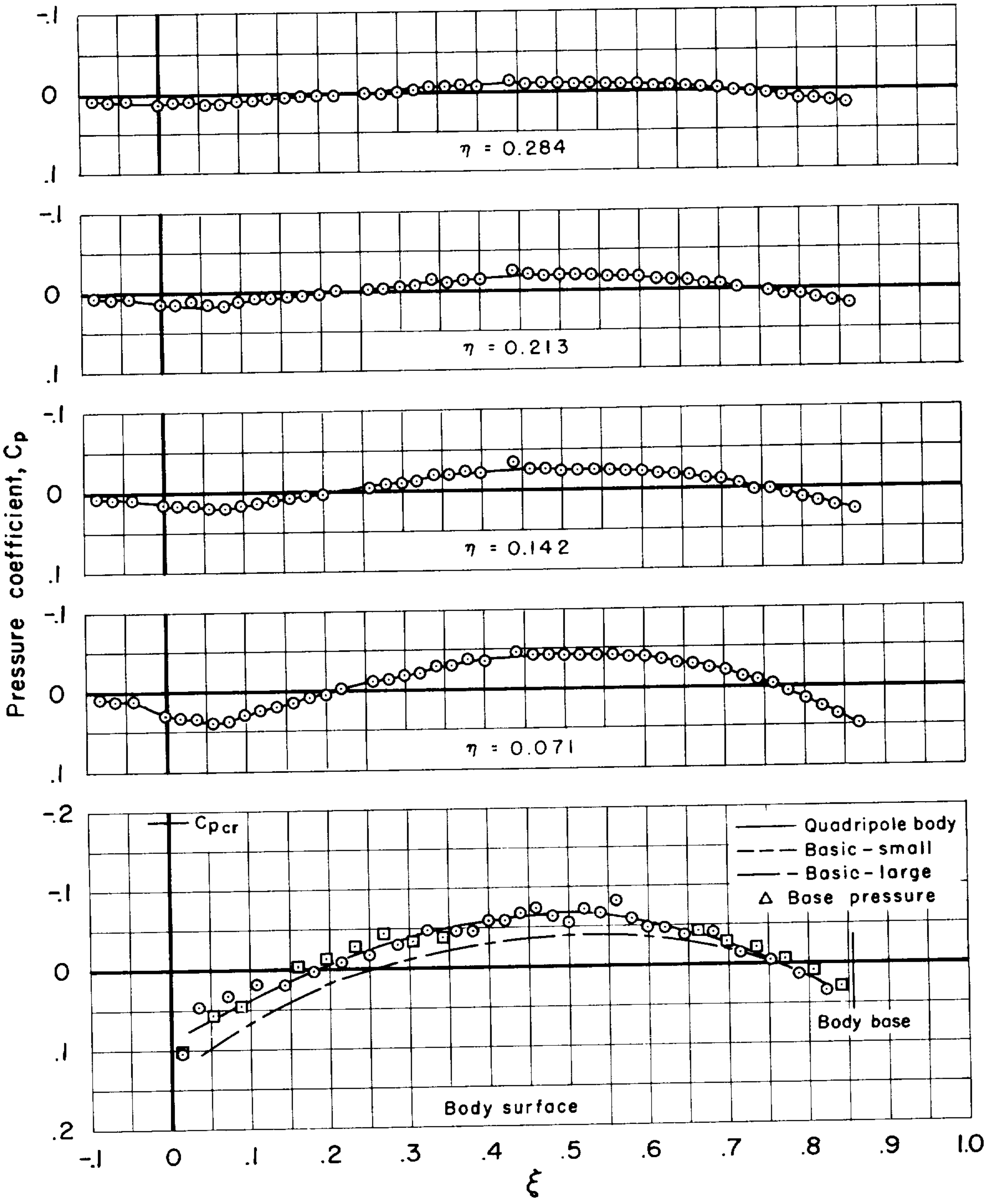

(a) $M_\infty = 0.90$, $\theta = 45^\circ$

Figure 10.- Pressure distributions for the basic and quadripole bodies.

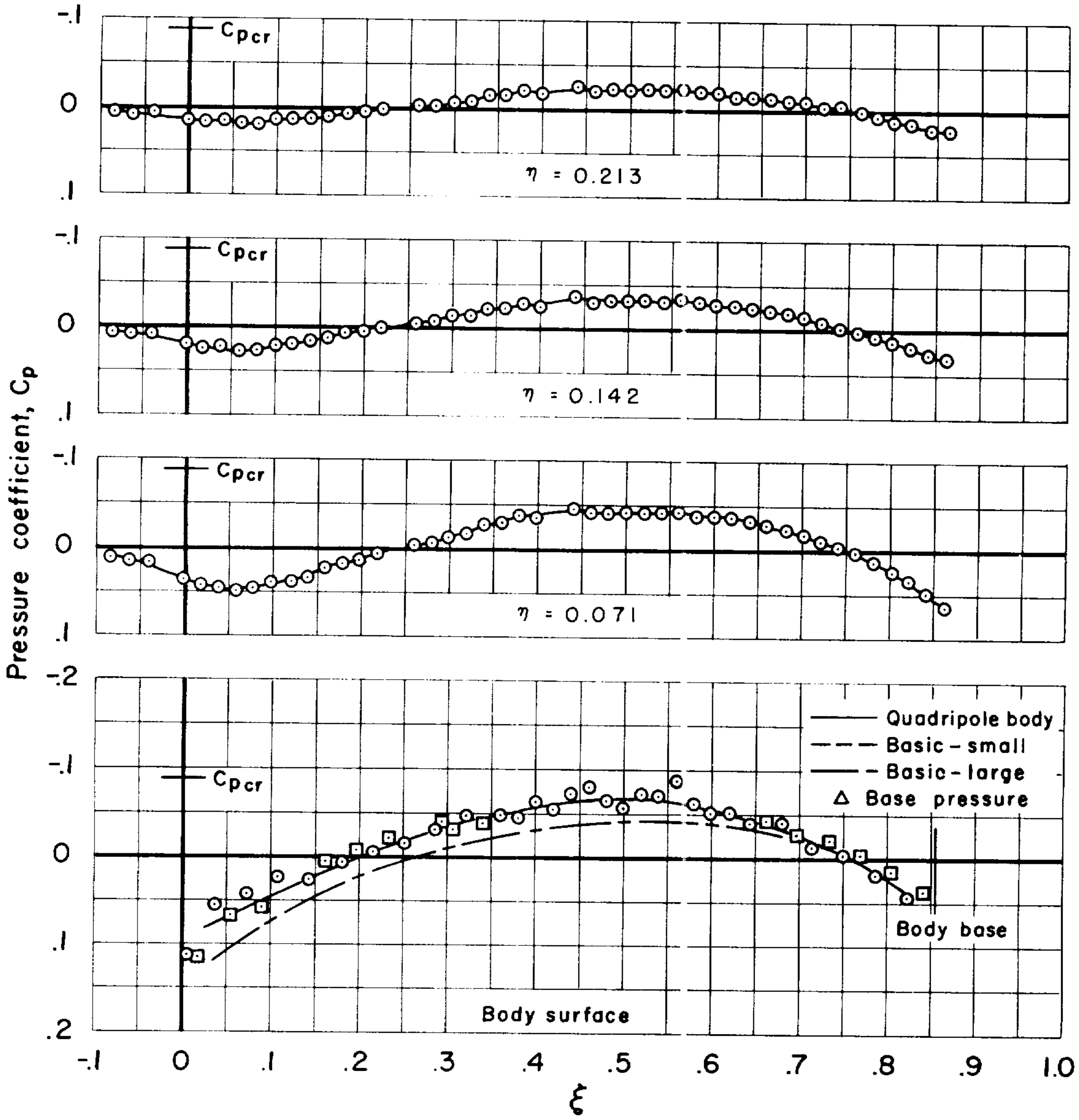

(b) $M_\infty = 0.95$, $\theta = 15^\circ$

Figure 10.- Continued.

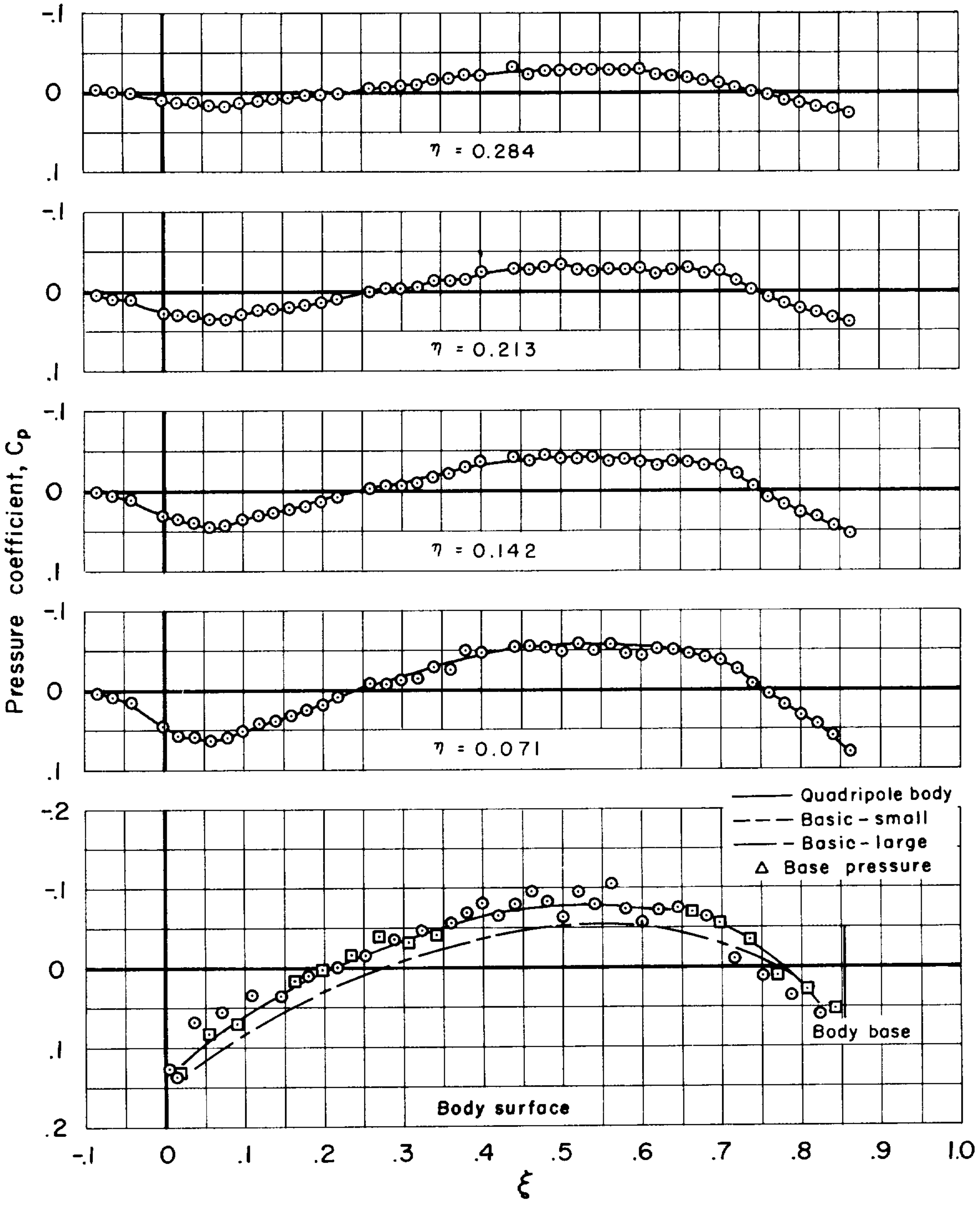

(c) $M_\infty = 1.0$, $\theta = 45^\circ$

Figure 10.- Continued.

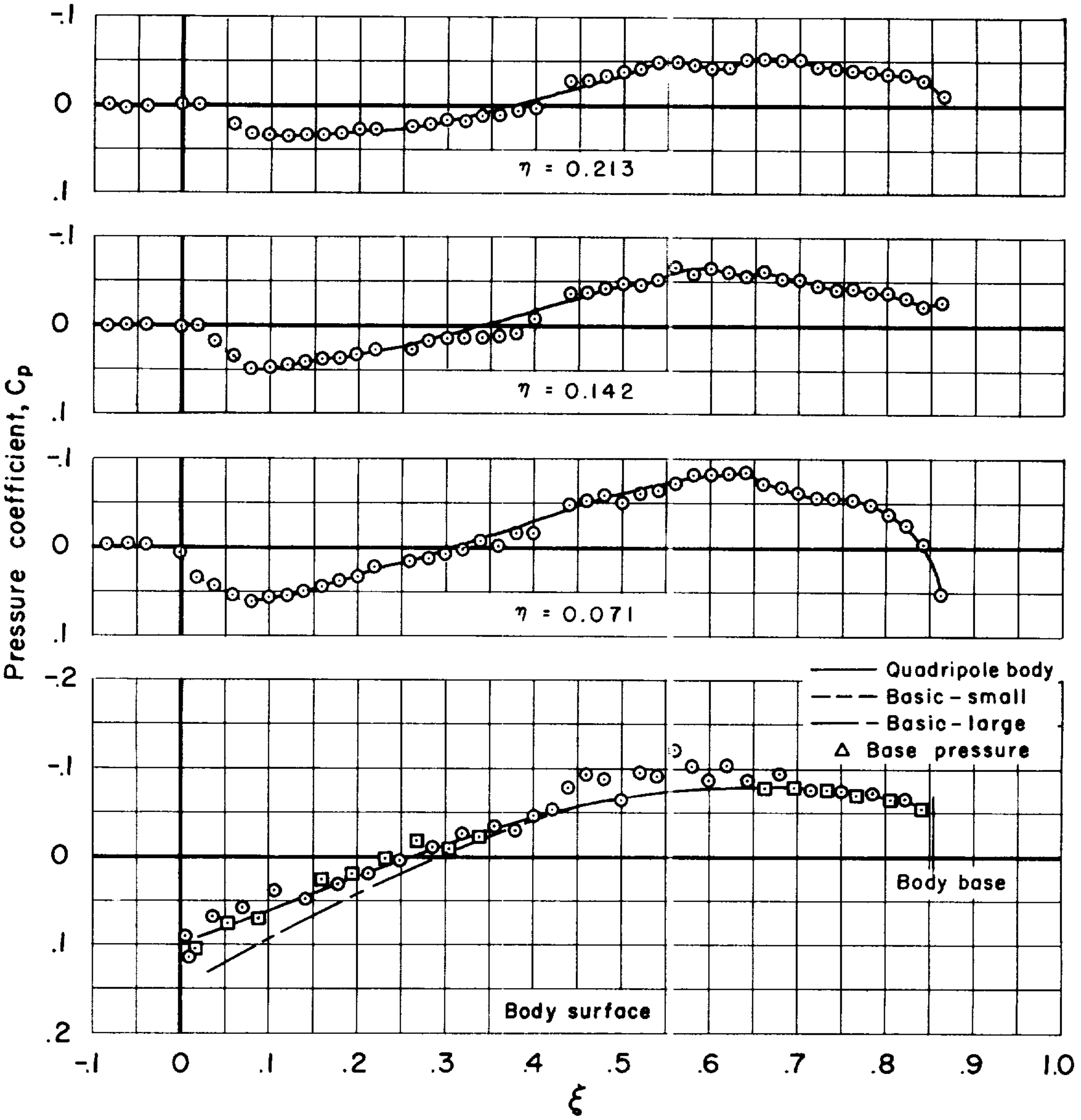

(d) $M_\infty = 1.05$, $\theta = 45^\circ$

Figure 10.- Continued.

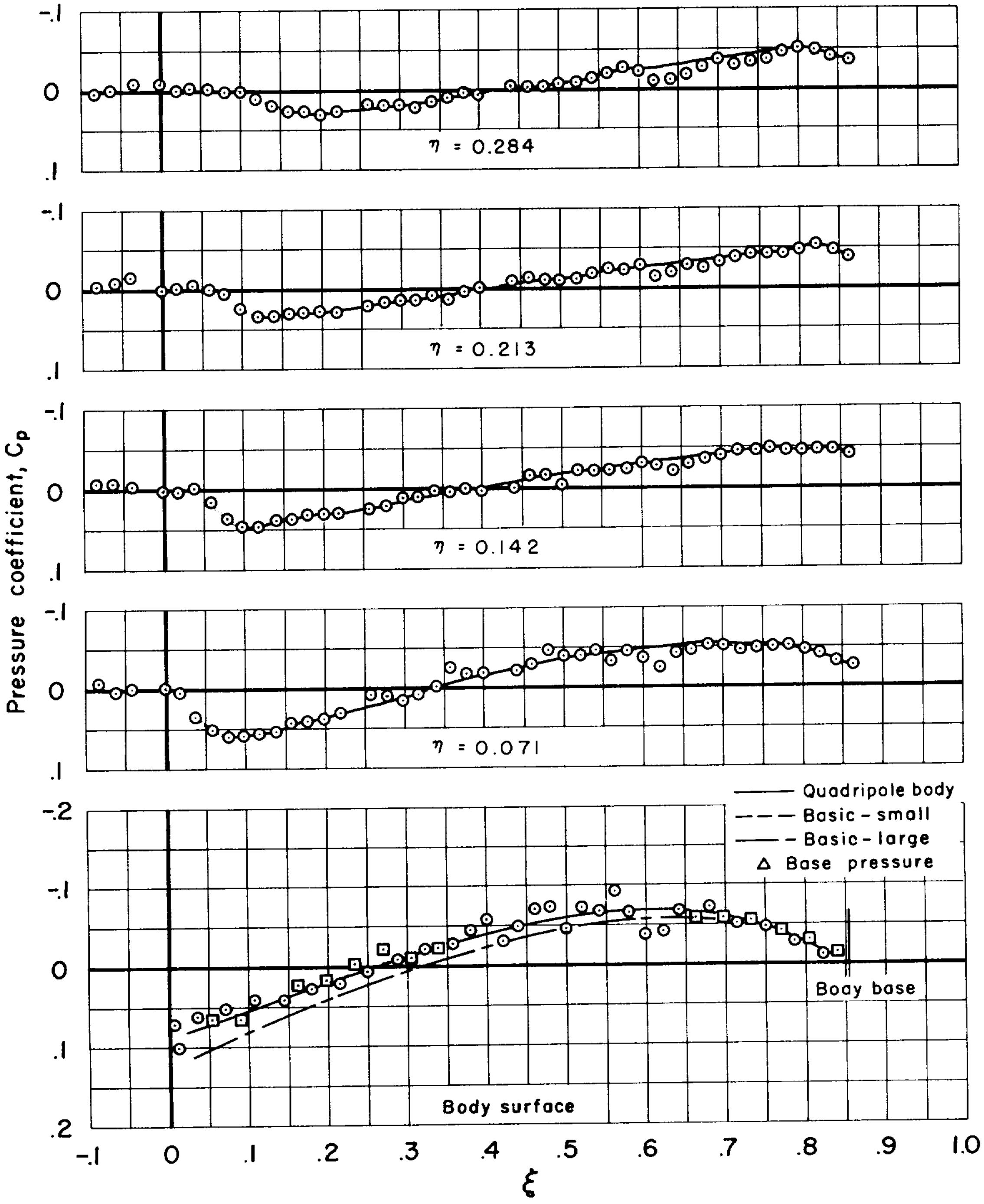

(e) $M_\infty = 1.10$, $\theta = 45^\circ$

Figure 10.- Continued.

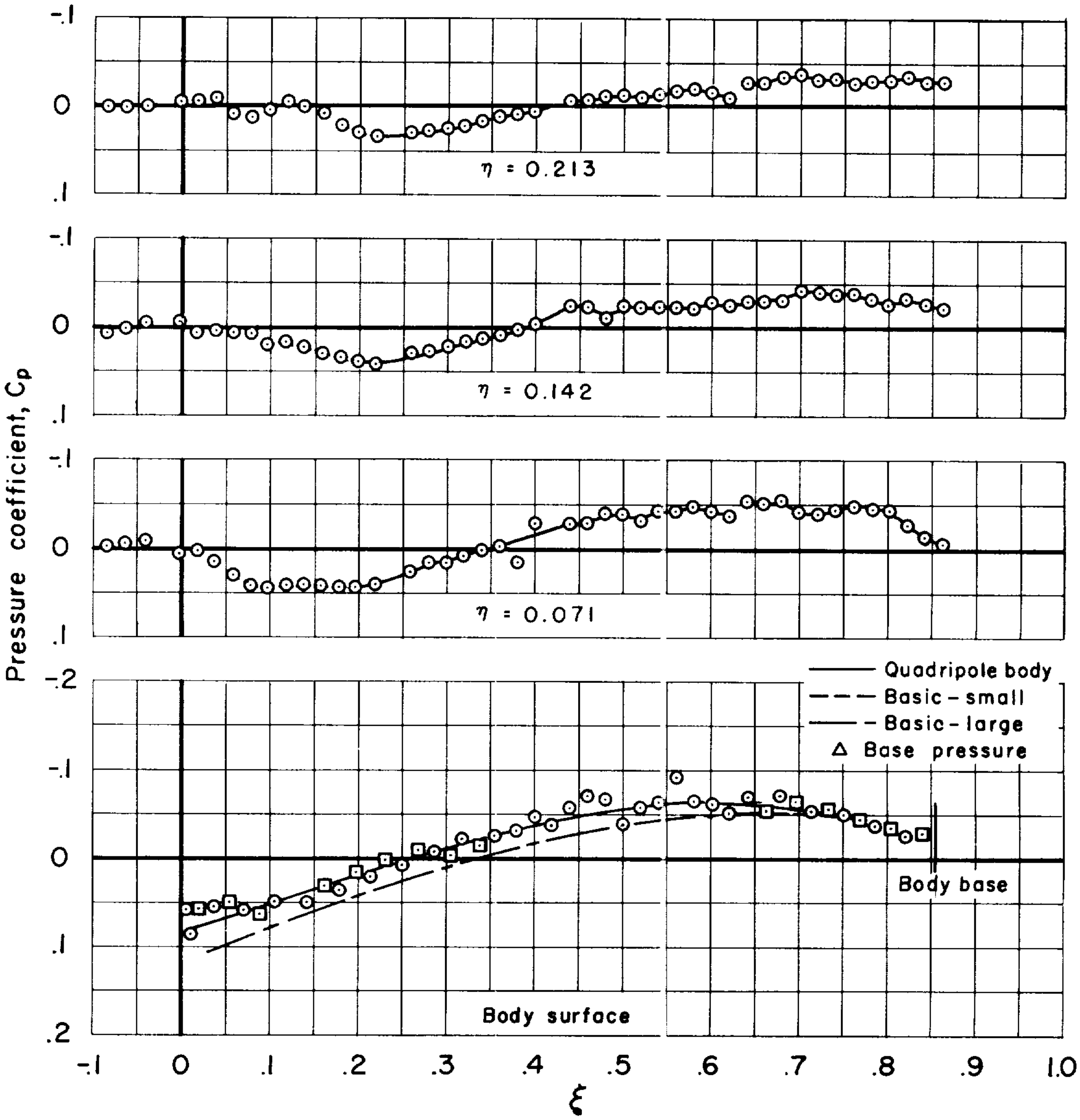

(f) $M_\infty = 1.20$, $\theta = 45^\circ$

Figure 10.- Concluded.

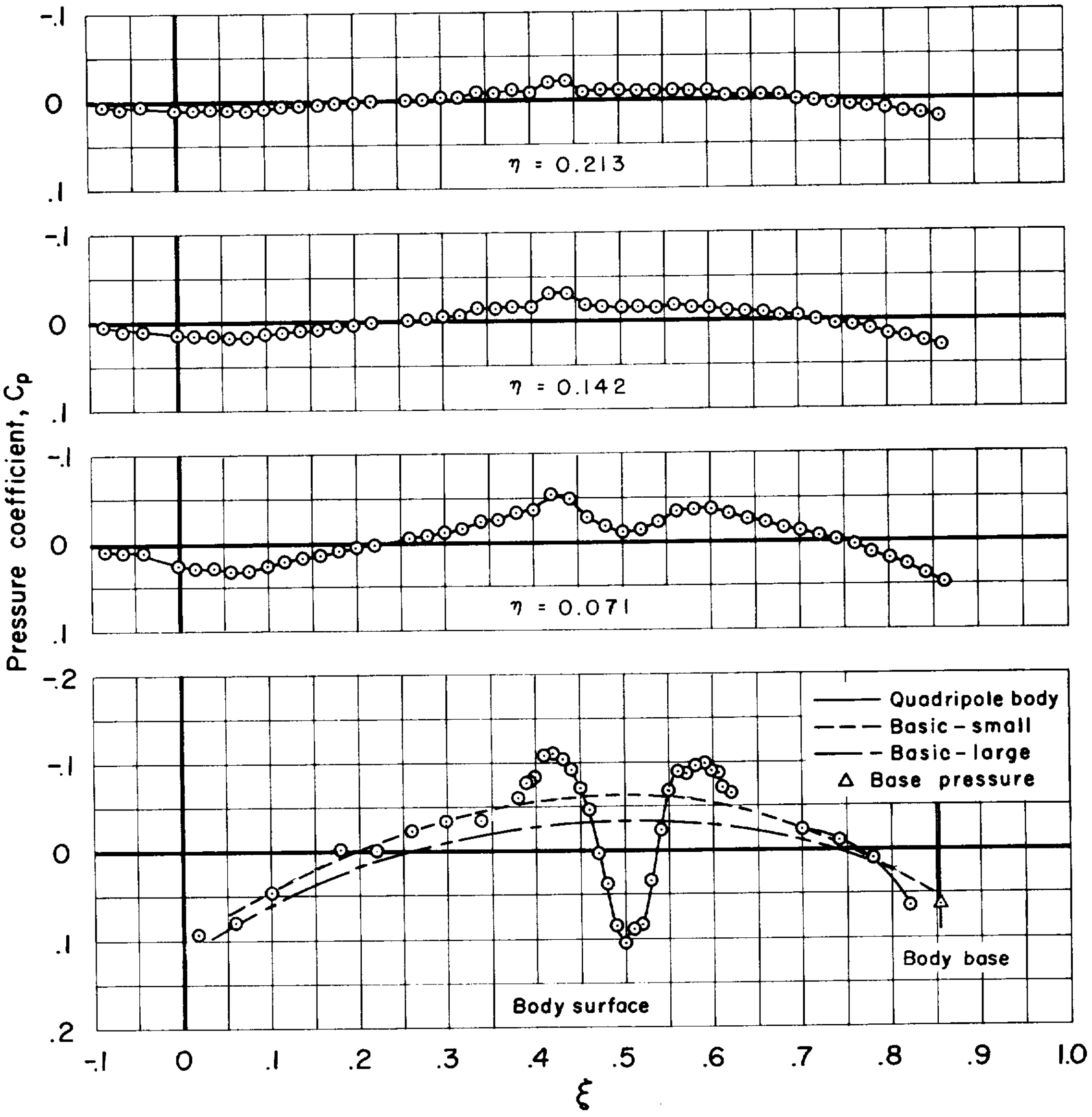

(a) $M_\infty = 0.80$, $\theta = 90^\circ$

Figure 11.- Pressure distributions for the basic and quadripole bodies.

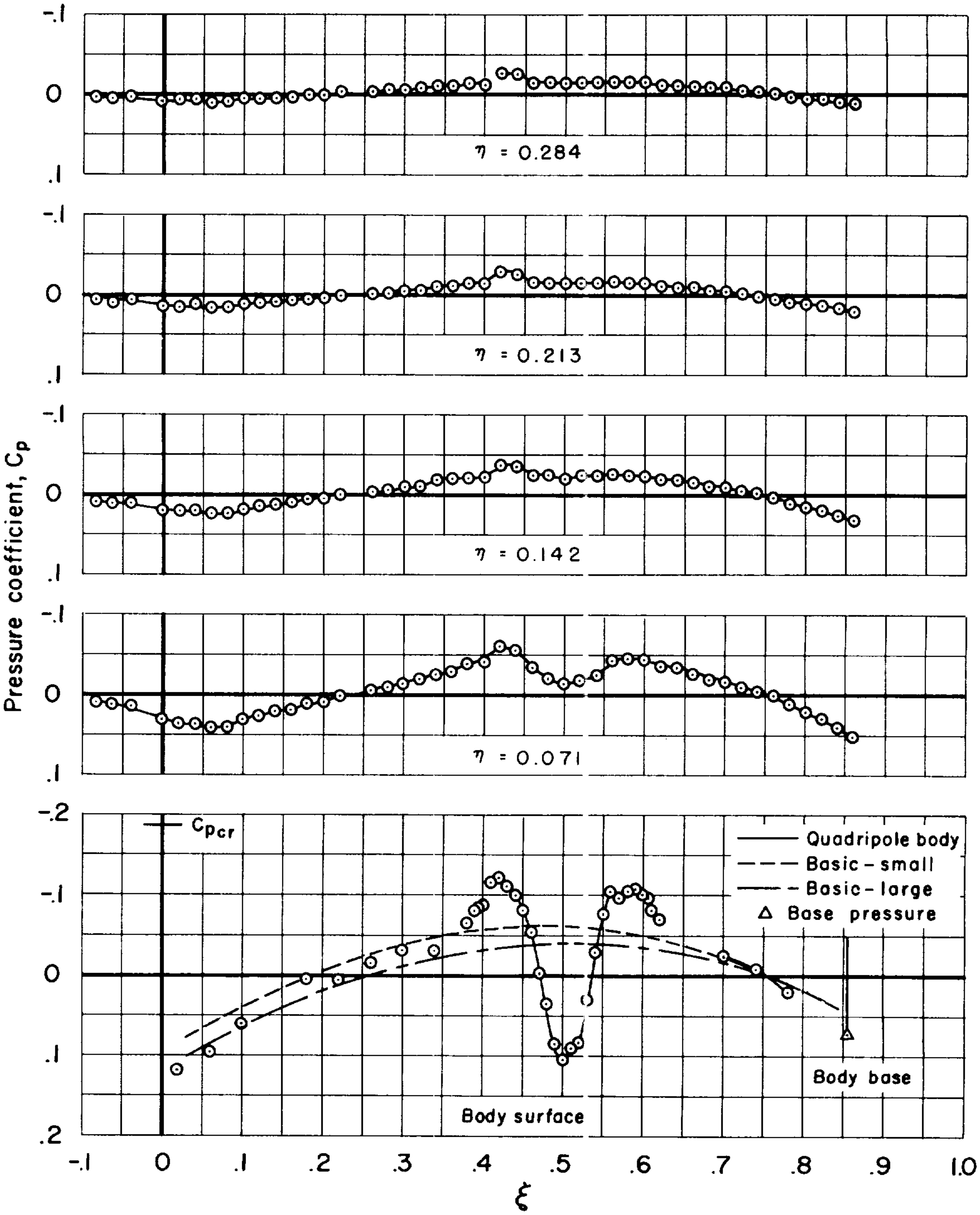

(b) $M_\infty = 0.90$, $\theta = 90^\circ$

Figure 11.- Continued.

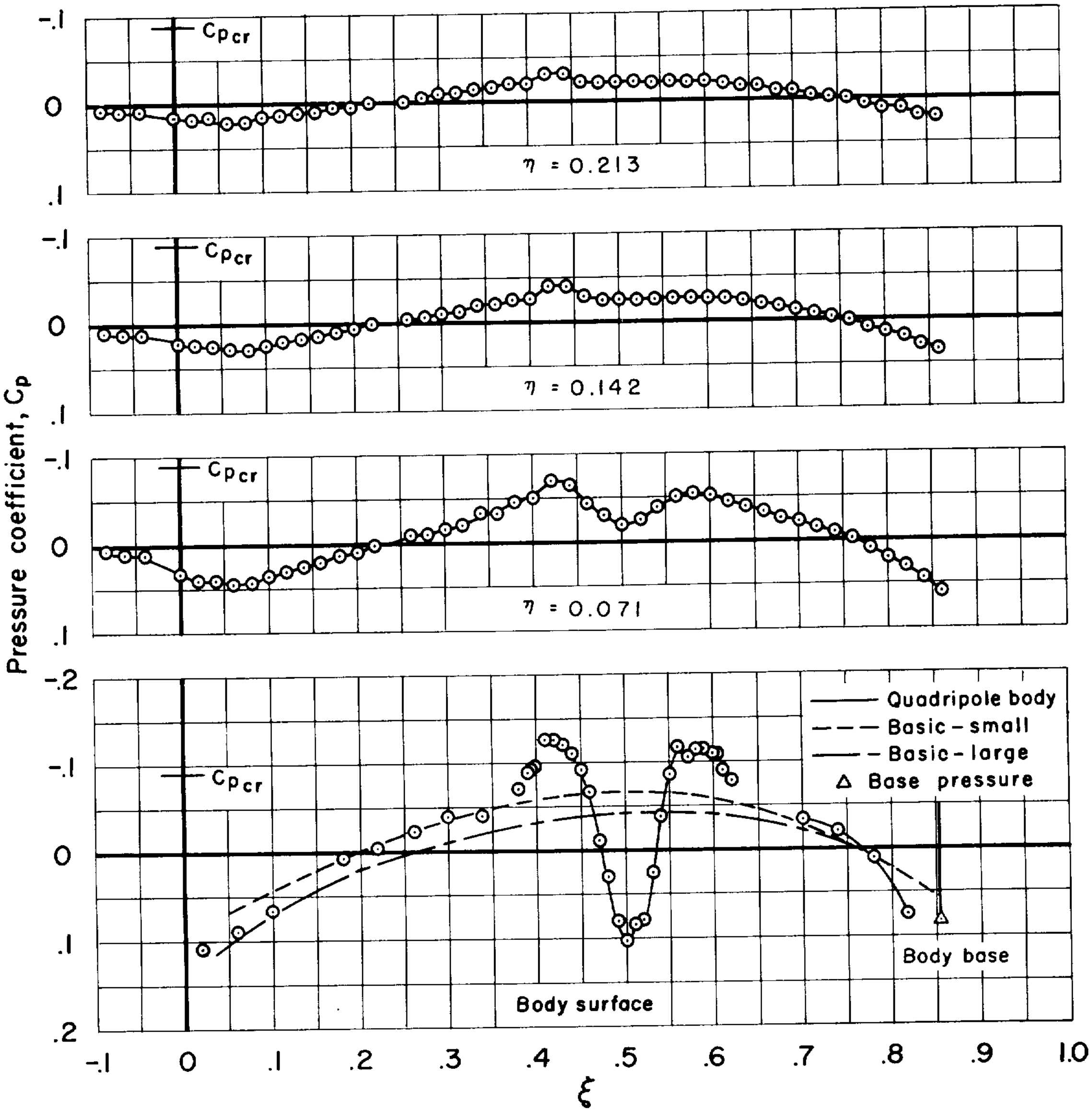

(c) $M_\infty = 0.95$, $\theta = 90^\circ$

Figure 11.- Continued.

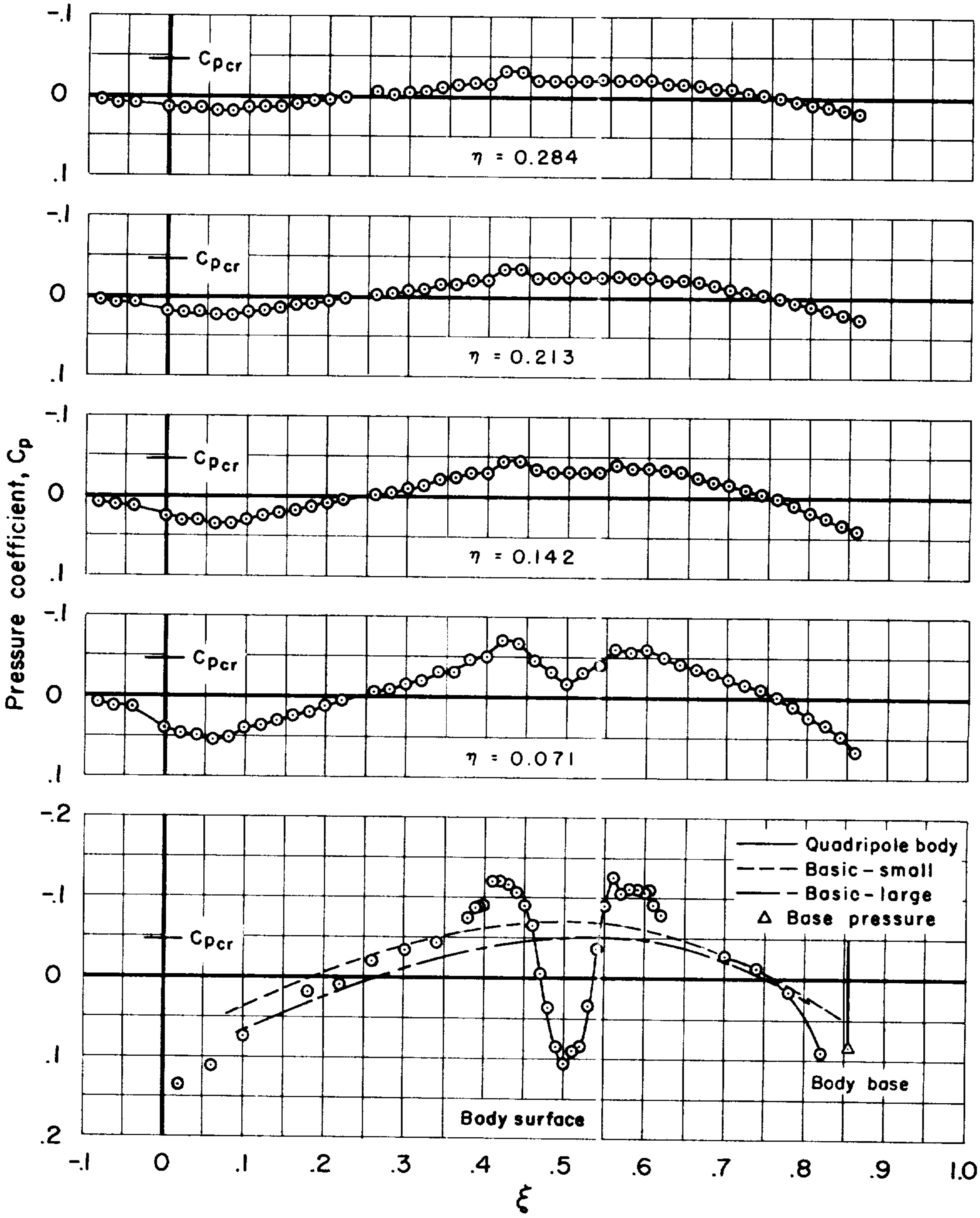

(d) $M_\infty = 0.975$, $\theta = 90^\circ$

Figure 11.- Continued.

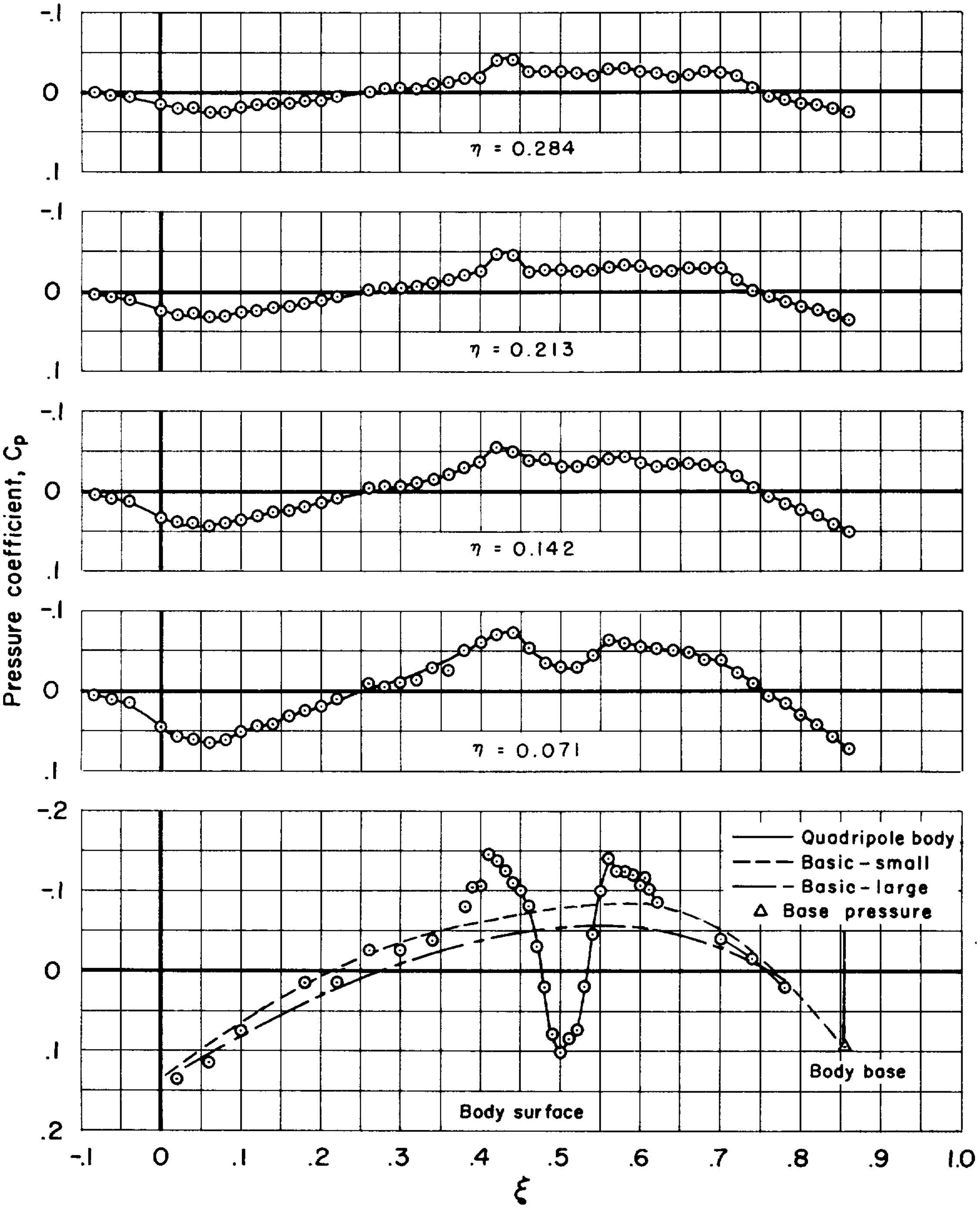

(e) $M_\infty = 1.0$, $\theta = 90^\circ$

Figure 11.- Continued.

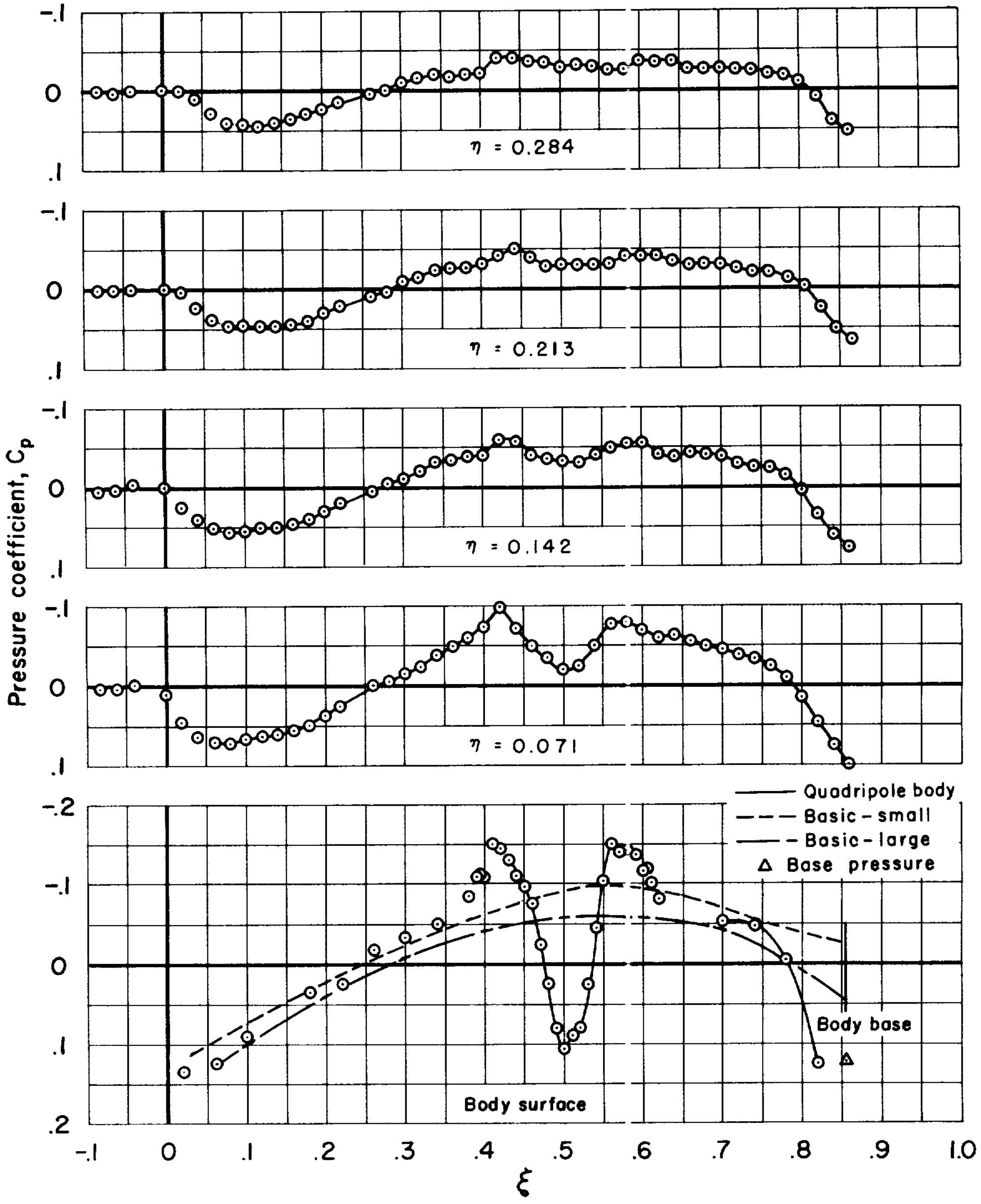

(f) $M_\infty = 1.025$, $\theta = 90^\circ$

Figure 11.- Continued.

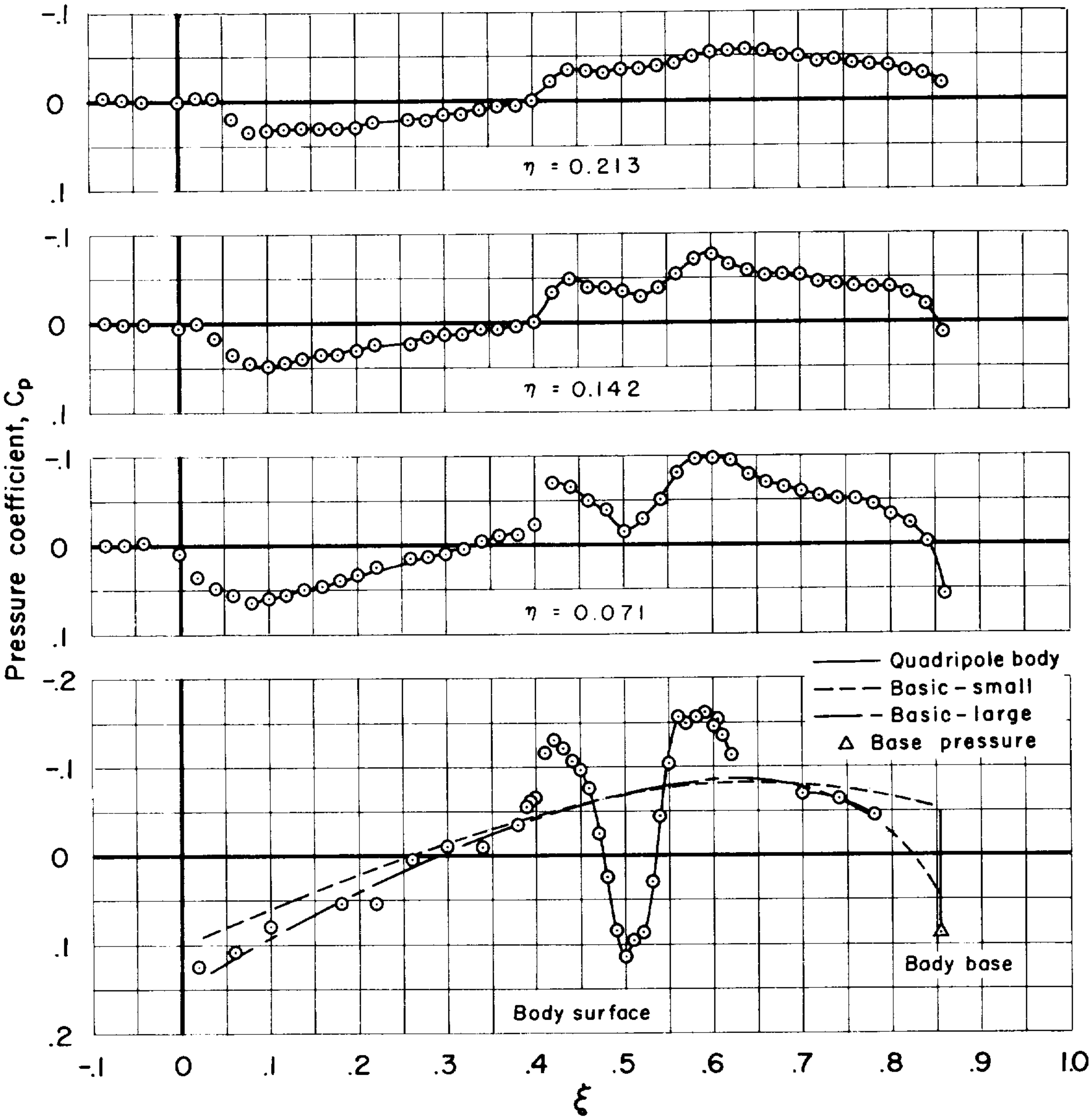

(g) $M_\infty = 1.05$, $\theta = 90^\circ$

Figure 11.- Continued.

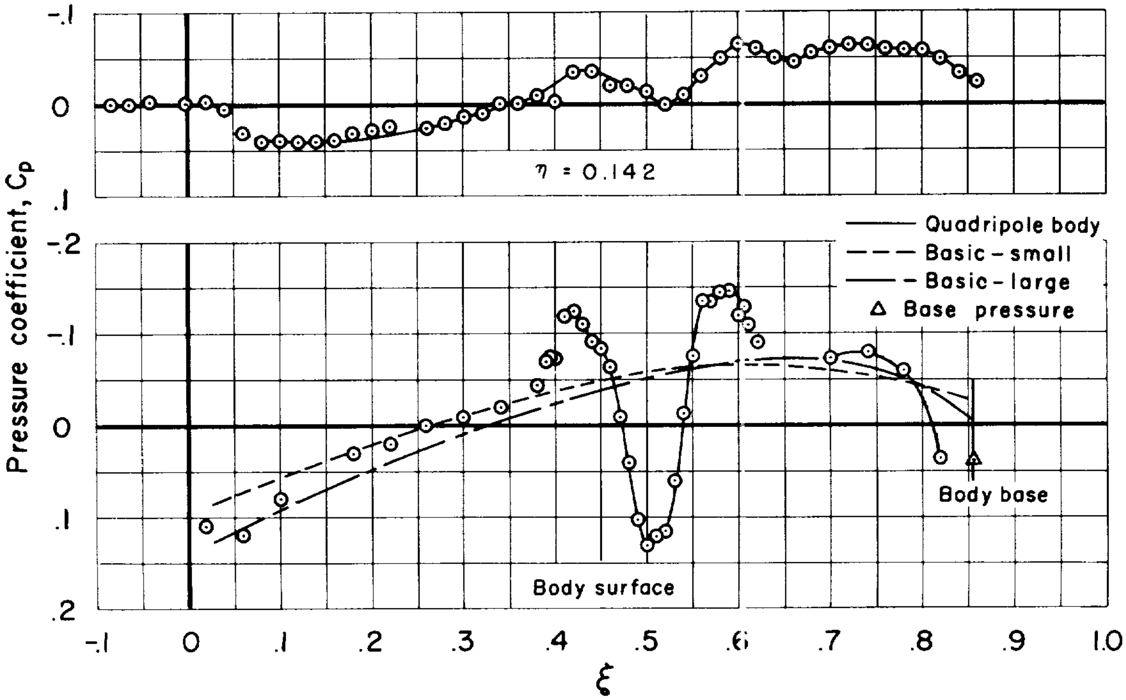

(h) $M_\infty = 1.075$, $\theta = 90°$

Figure 11.- Continued

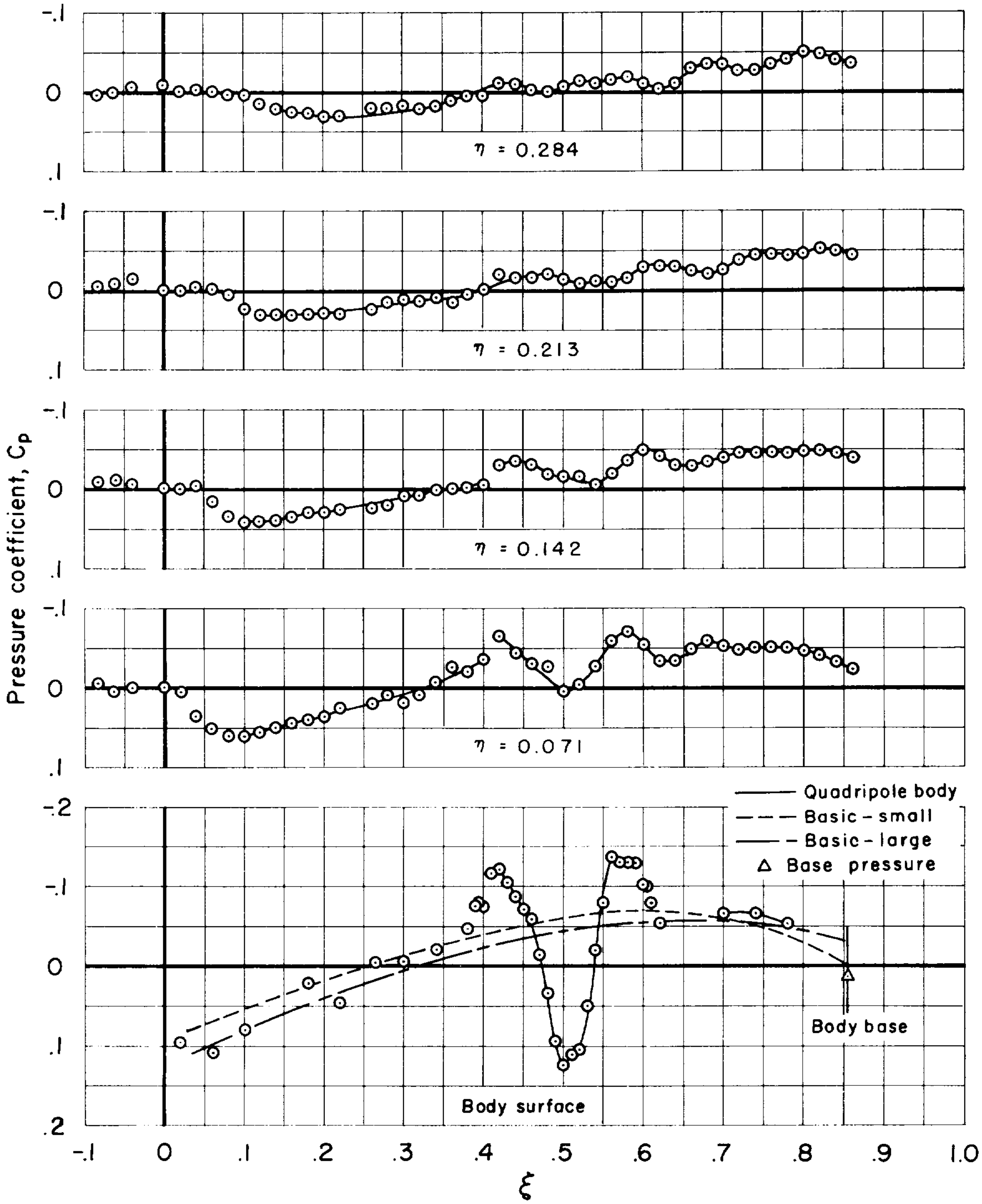

(i) $M_\infty = 1.10$, $\theta = 90^\circ$

Figure 11.- Continued.

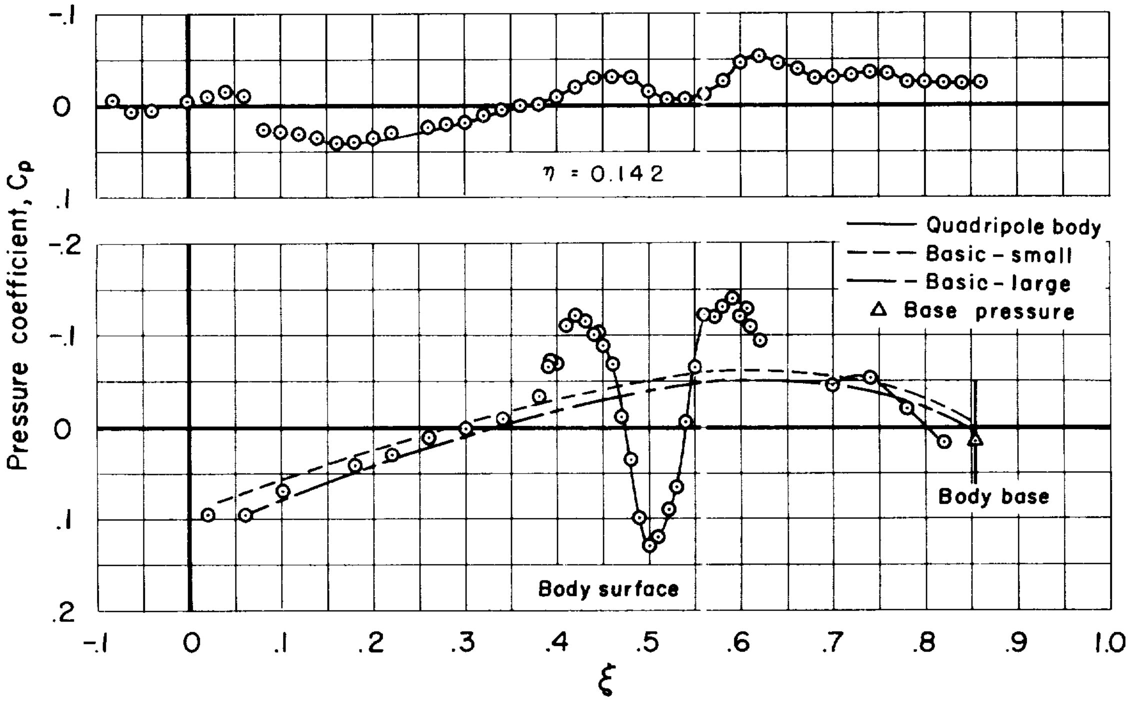

(j) $M_\infty = 1.15$, $\theta = 90^\circ$

Figure 11.- Continued.

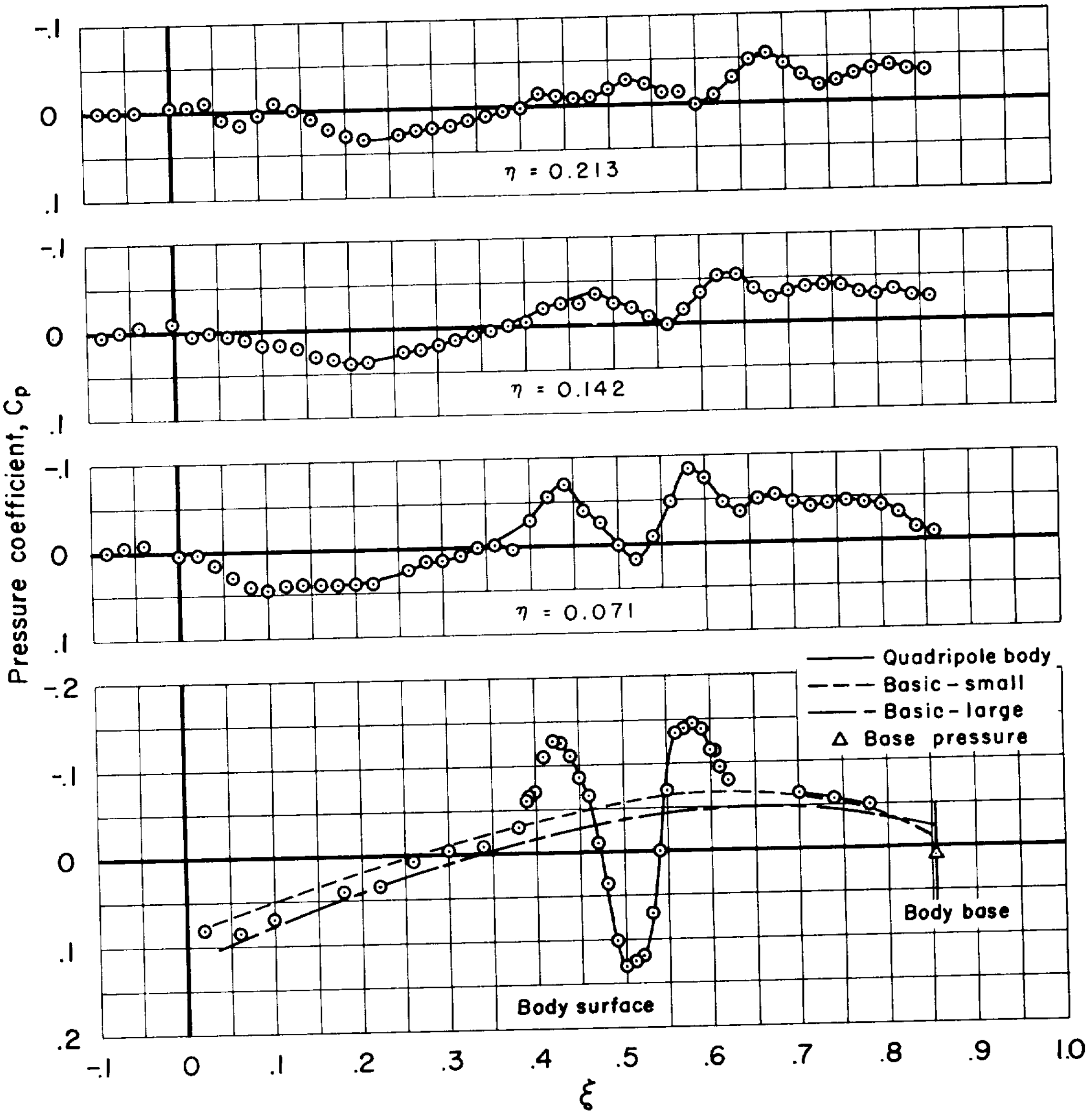

(k) $M_\infty = 1.20$, $\theta = 90^\circ$

Figure 11.- Concluded.

NASA - Langley Field, Va.

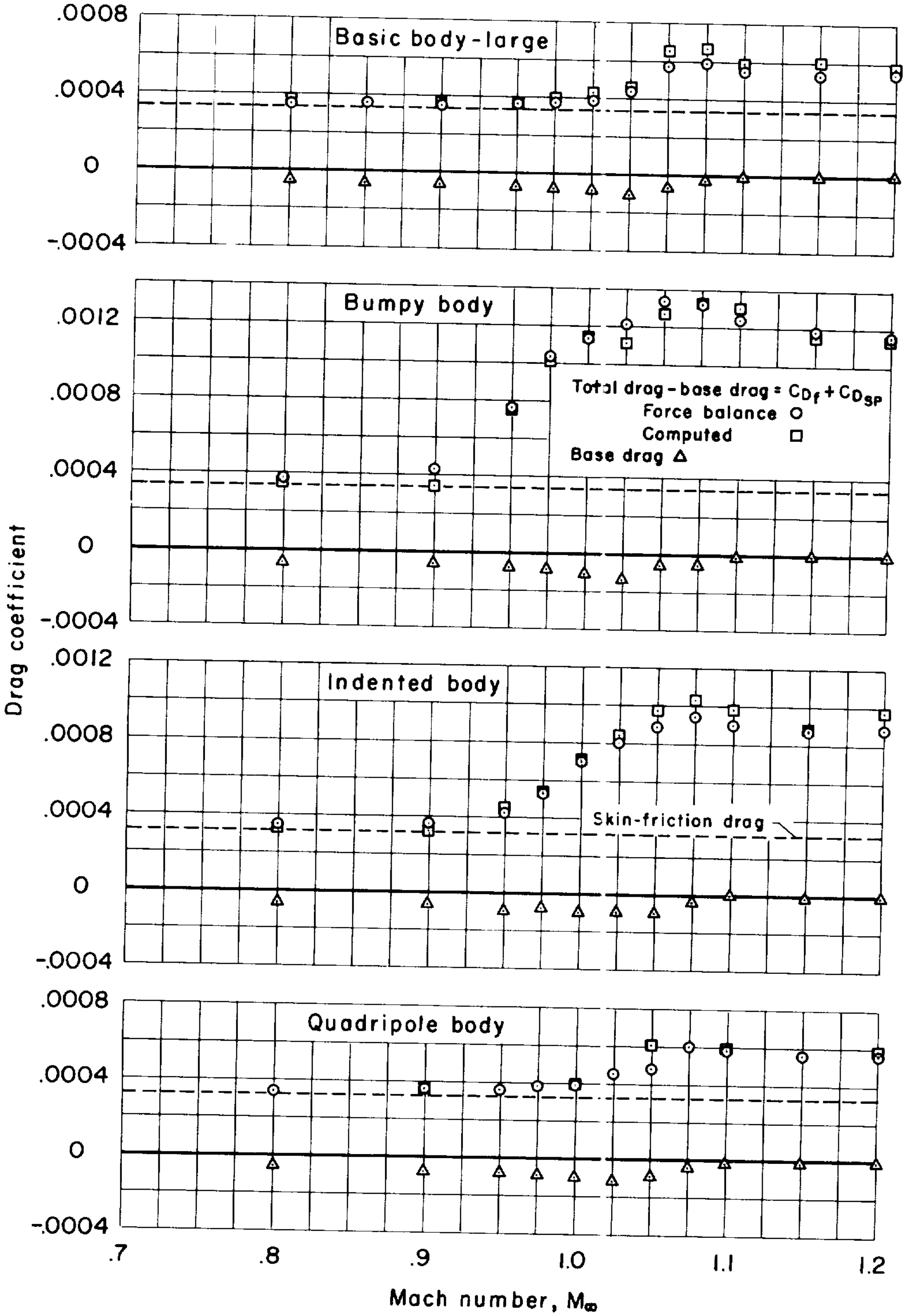

Figure 12.- Variation of drag coefficient with Mach number for the large basic, indented, bumpy, and quadripole bodies.